3. Modelling of Steady State Fibre Formation Process in Melt Spinning

3.1 Steady State Single Fibre Formation Process

3.1.1 Definition: What Does Fibre Formation Mean?

Melt spinning is the production of continuous solid filaments from polymeric melt. The fibre formation process includes change in shape, structure and properties of the thermoplastic polymer. The polymer pellets or granules are fed into an extruder where, through heating, their melting temperature is exceeded. The polymeric melt is then transported, under pressure, to the spinneret. Hygroscopic polymers require vacuum drying prior to processing in order to ensure a low water content. The extrusion temperature T_0 is roughly 30-50 K above the melting temperature T_m of the polymer, i. e. T_0=250-270°C for PA 6 or 280-295°C for PET, respectively. A constant mass flow rate of the melt is achieved by a metering pump (the spinning pump) which can be positioned inside the spinning head. Within the spinneret the melt flow is channelled into a number of individual capillary holes, each is responsible for the formation of a single filament. After the melt flow passes through these spinneret orifices into the air, the single filaments cool off, solidify, and are collected into a fibre bundle that is finally wound up. The take-up speed is much higher than the average extrusion velocity at the spinneret exit. The ratio between the spinning velocity v_L (take-up velocity at any distance L) and the (average) extrusion velocity v_0 at the spinneret exit defines the *draw down ratio ddr*:

$$ddr = \frac{v_\mathrm{L}}{v_0} \,. \tag{3.1}$$

Between take-up of the as-spun fibre and the final winding to bobbins an additional drawing procedure (with additional draw ratio DR) may be introduced. The drawing is typically achieved by means of godet pairs. Two or more drawing steps can be performed (Fig. 3.1). Fibre formation in the sense of *spinnability* requires three necessary conditions:

1. Attenuation and acceleration of the filaments, i. e. $ddr > 1$,
2. Stability in time that allows the production of continuous filaments, i. e. no filament breakage,

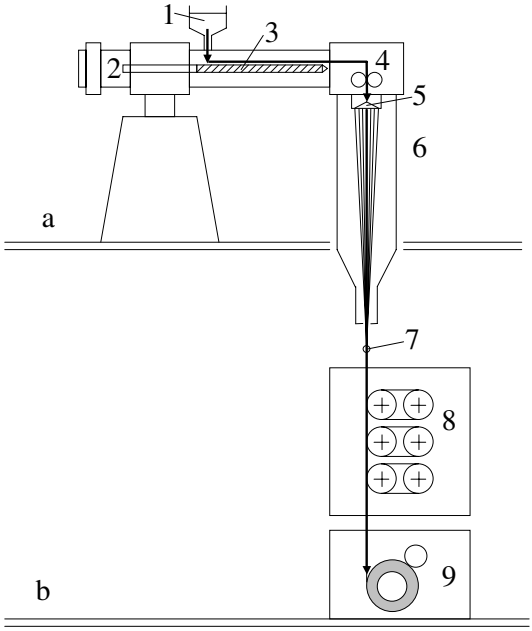

Fig. 3.1. Melt spinning equipment (schematic): a – spinning floor, b – winding floor; 1 – container with polymer pellets, 2 – electrical motor and drive train, 3 – extruder assembly with screw, 4 – spinning head with metering pump (gear pump), 5 – spinneret with capillary holes, 6 – spinning chamber with quenching air, 7 – spin finish applicator, 8 – pairs of godets for online drawing, 9 – (high speed) winder

3. Steady state conditions (stationarity), i. e. uniform filaments without any variation of properties throughout the production time and therefore along the filament length.

The maximum possible draw down ratio for a given polymer is an important characteristic value for the *spinnability* of the polymeric melt. For well-spinnable polymers draw down ratios of several hundred to up to $ddr > 1000$ can be reached in the high speed spinning process. Specifically the high speed fibre spinning shows extremely high deformation and cooling rates. Structural changes and phase transition from liquid to solid state are possibly taking place within *milliseconds*.

3.1.2 Fundamental Balance Equations

At the exit of the capillary holes (at distance $x = 0$) the polymeric melt is extruded with a given constant mass throughput Q and extrusion velocity v_0 at a constant extrusion temperature T_0 (Fig. 3.2). The diameter of the spinneret capillary holes is D_0. The take-up device (godets, winder or air suction device) positioned at any distance L from the spinneret, determines

the final take-up velocity v_L of the as-spun filaments. The velocity $v(x)$, the diameter $D(x)$, the temperature $T(x)$, and the filament force $F(x)$ depend upon the axial distance x from the spinneret. Their courses play an essential role in the development of the fibre structure and the resulting textile yarn properties. The theory of steady state fibre formation helps to describe the deformation, cooling, and stress developing processes. It is, in principle, an application of the fundamental physical balance equations [274] of *mass, energy,* and *momentum*, combined with the stress-deformation behaviour of the polymer and the description of its structural changes.

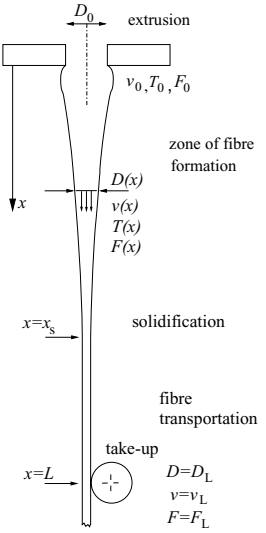

Fig. 3.2. Fibre formation in melt spinning

Mass Balance

The mass balance represents the continuity equation of the melt spinning process. It is largely simplified because no mass exchange takes place between the filament and its environment. The mass conservation formula connects the most important quantities, mass throughput Q, filament cross sectional area $A(x)$ (or filament diameter $D(x)$, respectively), and the (averaged over the cross section) axial filament velocity $v(x)$:

$$Q = \varrho_p(x) \cdot A(x) \cdot v(x) = \text{const.} \tag{3.2}$$

The quantity ϱ_p in Eq. 3.2 denotes the mass density of the polymer. The product $\varrho_p(x) \cdot A(x) = Tt(x)$ is known in textile engineering as fineness (titre). For a circular cross section with diameter $D(x)$ follows

$$Q = \varrho_p \cdot \frac{\pi}{4} D^2 \cdot v = Tt \cdot v \; . \tag{3.3}$$

The fineness Tt quantifies the linear mass density (mass per unit length of the fibre) and has its own special units. The most common are *tex* (resp. *decitex*) and *denier* (den), defined as

$$1\,\text{tex} = \frac{1\,\text{g}}{1000\,\text{m}}\,, \qquad 1\,\text{dtex} = \frac{1\,\text{g}}{10\,000\,\text{m}}\,, \qquad 1\,\text{den} = \frac{1\,\text{g}}{9000\,\text{m}}\,.$$

The fineness of a fibre is called 1 dtex if 10 000 meters of fibre material is equal to 1 gram (resp. the fineness 1 den equals 9 000 meters of 1 gram mass). The relation between *fineness* Tt (in dtex or denier), and *diameter* D (in µm) depends on the mass density ϱ_p (in g/cm^3) and is given by

$$Tt = 0.0078\,\varrho_\text{p}\,D^2, \quad D = 11.3\,\sqrt{Tt/\varrho_\text{p}} \qquad \text{for} \quad Tt \quad \text{in dtex,} \tag{3.4a}$$

$$Tt = 0.0112\,\varrho_\text{p}\,D^2, \quad D = 9.44\,\sqrt{Tt/\varrho_\text{p}} \qquad \text{for} \quad Tt \quad \text{in denier.} \tag{3.4b}$$

Two examples (with given mass densities) are listed in Table 3.1.

Table 3.1. Equivalence between fineness and diameter

	Fineness Tt	Diameter D
PP – poly(propylene)	1 dtex	12 µm
($\varrho_\text{p} = 0.9\,\text{g/cm}^3$)	10 dtex	37 µm
	100 dtex	119 µm
PET – poly(ethylene terephthalate)	1 dtex	10 µm
($\varrho_\text{p} = 1.35\,\text{g/cm}^3$)	10 dtex	31 µm
	100 dtex	97 µm

Due of the fundamental character and simplicity of the mass balance Zi-ABICKI [274] distinguishes the principal process variables by means of the continuity equation into *primary*, *secondary*, and *resulting* variables.

Primary variables

- describe the material, its chemical and molecular structure (molecular weight, molecular weight distribution), and the material's characteristics like viscosity, heat capacity, solidification behaviour etc.
- Primary variables are also the parameters which determine the technological conditions of the melt spinning process. These are the mass throughput Q delivered by the spinning pump, the extrusion temperature T_0, the dimensions of the capillary holes (diameter D_0), the length of the spinning line L from spinneret to the take-up device, the take-up velocity v_L, and the conditions of the cooling process, its velocity profile v_air of quenching air, the temperature profile T_air, and the air humidity.

Secondary spinning variables result from the primary variables by application of the continuity equation (3.2). Examples are:

- the (average) extrusion velocity v_0 with

$$v_0 = \frac{Q}{\varrho_\mathrm{p} \frac{\pi}{4} D_0^2} ,$$

- the as-spun fineness $Tt_\mathrm{L} = Q/v_\mathrm{L}$, and the corresponding diameter D_L,
- the draw down ratio ddr (3.1) with

$$ddr = \frac{v_\mathrm{L}}{v_0} = \frac{v_\mathrm{L}}{Q} \varrho_\mathrm{p} \frac{\pi}{4} D_0^2 .$$

The formulas show that the secondary variables are combinations of the primary variables, specifically the draw down ratio.

Resulting variables are determined by primary variables as well as the dynamics of the fibre formation process. Some examples are:

- the development of the fibre velocity $v(x)$ along the spinning path,
- the length of the fibre formation zone, i. e. the distance between the spinneret and the solidification point,
- the maximum deformation rate of the polymeric downstream,
- the filament tension force $F(x)$ and the filament stress $\sigma(x)$ at any distance x from spinneret, especially at the solidification point and at the take-up point,
- the filament temperature $T(x)$.

The development of stress and temperature and the structural changes determine the physical and textile properties such as orientation, crystallinity, elongation at break, tenacity and many others.

Modelling the dynamics of fibre formation should lead to a sufficient description of the resulting variables and their correlations to the fibre properties. The main goal is helping to understand the influence of primary variables (material properties and technological process parameters) on the resulting product properties.

Energy Balance

The energy equation describes the development of the filament temperature $T(x)$ from the point of exiting the capillary holes to the points of solidification and take-up.

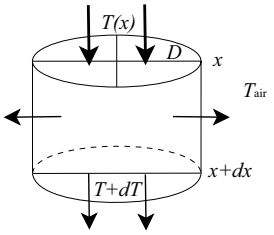

Fig. 3.3. Heat flow balance of a filament volume element (schematic)

Simplified analysis. If we at first assume only heat convection (i. e. no heat conduction and no heat sources within the filament, no heat radiation), then the heat balance of any volume element between x and $x + dx$ is given by the following equation: The difference of heat flow into the unit volume and out of it must be equal to the total heat loss of the unit volume, that is the heat transfer from the surface of the unit volume into the surrounding air (Fig. 3.3).
The heat balance equation can be written as

$$Q \cdot c_\mathrm{p} \cdot T - Q \cdot c_\mathrm{p} \cdot (T + \mathrm{d}T) = \alpha \cdot (T - T_\mathrm{air}) \cdot \pi \cdot D \cdot \mathrm{d}x \; . \tag{3.5}$$

Using the so-called (non-dimensional) NUSSELT number Nu with

$$Nu = \frac{\alpha \cdot D}{\lambda_\mathrm{air}} \tag{3.6}$$

leads to

$$\frac{\mathrm{d}T}{\mathrm{d}x} = -(T - T_\mathrm{air}) \cdot Nu \, \frac{\pi \, \lambda_\mathrm{air}}{Q \cdot c_\mathrm{p}} \; . \tag{3.7}$$

In Eqs. 3.5–3.7 T_air is the temperature of surrounding air, α is the heat transfer coefficient from the filament surface to the surrounding air, c_p represents the specific heat capacity of the polymer, and λ_air stands for the heat conductivity of air.

The NUSSELT number (or the heat transfer coefficient α) is an essential parameter for calculating the filament temperature profile $T(x)$. A more detailed discussion of heat transfer will follow in Sect. 3.1.3. Here it should be pointed out that the fraction on the right hand side of Eq. 3.7 has the dimension of a reciprocal length:

$$Nu \, \frac{\pi \, \lambda_\mathrm{air}}{Q \cdot c_\mathrm{p}} = \frac{1}{L_\mathrm{c}} \; . \tag{3.8}$$

Equation (3.7) then becomes

$$\frac{\mathrm{d}T(x)}{\mathrm{d}x} = -\frac{T(x) - T_\mathrm{air}(x)}{L_\mathrm{c}(x)} \quad \text{with} \quad T(0) = T_0 \; . \tag{3.9}$$

Example. To get an impression of the cooling of poly(ethylene terephthalate) (PET) filaments the following typical values should be used:

specific heat capacity (PET)	c_p	1500 kJ/kg K
temperature of the melt (PET)	T_0	290 °C
air temperature	T_air	20 °C
heat conductivity of air	λ_air	10^{-5} W/m
NUSSELT number	Nu	≈ 1

Using the parameters above (see also Eqs. 2.3 and 2.6) the cooling length for PET per mass throughput becomes $L_\mathrm{c}/Q \approx 0.2\,\mathrm{m/g \cdot min^{-1}}$. In order to cool off a filament from its initial temperature of 290 °C to a solidification temperature of 70 °C (glass transition temperature of PET) at a throughput of 1 g/min, a cooling length of approximately 0.5 m is needed. As the throughput increases, the required cooling length increases as well, for $Q = 2$ g/min follows $L_\mathrm{c} \approx 1.0$ m, and so on.

Further discussions about energy balance. Heat is transferred not only via convection but also by heat radiation and heat conduction.

Heat radiation strongly depends upon the temperature (power law with T^4 dependence – STEPHAN-BOLTZMANN law). Radiation plays an important role for glass or metal spinning processes where the temperature can reach 1200 °C or more. But in melt spinning of thermoplastics with spinning temperatures of up to 300 °C the contribution of radiation is, consequently, often neglected.

Heat conduction occurs as inner conduction inside the fibres and also as outer conduction in such cases where fibres are brought into contact with other materials of different temperature, like fibre guides, metal plates or godets. The inner conduction is negligible for thin filaments, but needs to be taken into consideration for thick and very thick filaments. The contact of filaments with other objects is sometimes used to force the cooling process. But it is also possible to heat up the fibres in the contact area to initiate phase transitions or to achieve certain drawing effects.

A sensitive contribution to the energy balance of the fibre can arise from the internal heat which is set free when the filament crystallises. Stress-induced crystallisation appears especially in high speed spinning of PET, PA, PP and other crystallising polymers. It is necessary to take the crystallisation heat [59, 194–198, 200] into consideration for the modelling of such processes. The energy equation (3.7) then has to be expanded with the crystallisation term to

$$\frac{\mathrm{d}T}{\mathrm{d}x} = -(T - T_\mathrm{air}) \cdot Nu \frac{\pi\,\lambda_\mathrm{air}}{Q \cdot c_\mathrm{p}} + \frac{\Delta H}{c_\mathrm{p}} \frac{\mathrm{d}X_\mathrm{c}}{\mathrm{d}x}\,, \tag{3.10}$$

where ΔH is the heat of fusion and X_c is the degree of crystallinity.

The deformation energy can also be an additional source of internal heat. However, in melt spinning the contribution of internal friction processes can usually be neglected.

Momentum Balance

The momentum balance equation can be integrated in order to determine the forces acting on the fibre. In this manner, the forces play an essential role in structure development: the resulting fibre stress σ (that is fibre force F divided by fibre cross-sectional area A) leads to the deformation of the polymer and at least determines the orientational status and the structural arrangement of the polymeric chains.

The analysis of the force contributions reveals the following components which add-up to the total fibre force [274]:

- the initial force at the capillary exit F_0,
- the inertial force F_{inert},
- the gravitational force F_{grav},
- the air drag force F_{drag},
- the surface tension force F_{surf},
- the take-up force F_{L}

Figure 3.4 shows how the forces act on the fibre and how they contribute to the total fibre force.

$$F(x) = F_0 + F_{\text{surf}}(x) + F_{\text{inert}}(x) + F_{\text{drag}}(x) - F_{\text{grav}}(x) \tag{3.11a}$$

$$= F_{\text{L}} - F_{\text{surf}}(x) - F_{\text{inert}}(x) - F_{\text{drag}}(x) + F_{\text{grav}}(x) \tag{3.11b}$$

$$= F_{\text{rheo}}(x)\ . \tag{3.11c}$$

Discussion. Some more details should be discussed with respect to each force contribution and its effect on the total force should be discussed by means of simple estimation.

The *surface tension force* F_{surf} should be regarded at first. It is caused by the enlargement of the filament surface per unit volume during stretching and thinning of the fibre:

$$\frac{\mathrm{d}F_{\text{surf}}}{\mathrm{d}x} = \pi \frac{\mathrm{d}}{\mathrm{d}x}\left(\sigma_{\text{surf}} R\right) \tag{3.12}$$

or, after integration with respect to x (assuming constant σ_{surf}) follows

$$F_{\text{surf}}(x) = \pi\, \sigma_{\text{surf}} \big(R_0 - R(x)\big), \tag{3.13}$$

where σ_{surf} is the surface tension (or specific surface energy) of the material. The contribution of the surface tension force to the total force is usually low, except for very low viscous materials. A typical value for poly(ethylene

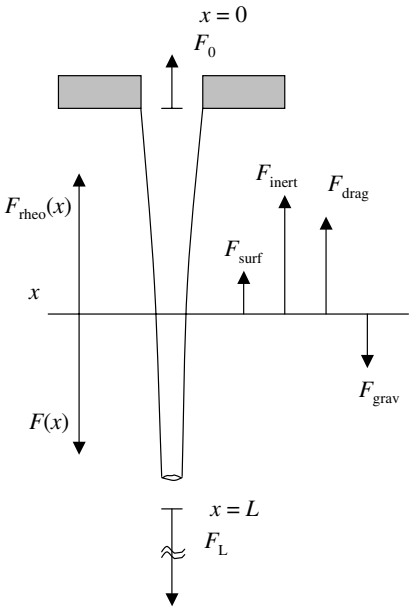

Fig. 3.4. Forces acting on a fibre

terephthalate) (PET) has a magnitude of about $\sigma_{\mathrm{surf}} \approx 0.05$ mN/mm, and with an assumed initial radius of $R_0 = 0.15$ mm one gets a surface tension F_{surf} lower then 0.02 mN.

The *gravitational force* F_{grav} at any distance x is the weight of the filament at this point and can be expressed as

$$F_{\mathrm{grav}}(x) = \int_0^x \varrho_{\mathrm{p}}\, g\, A(x')\, dx' \,, \tag{3.14}$$

where ϱ_{p} is the mass density of the polymer, g is the gravitational acceleration on earth ($g \approx 9.81$ m/s^2), and A denotes the filament cross-sectional area. Assuming a circular PET filament (mass density $\varrho_{\mathrm{p}} = 1.35$ g/cm^3) with an averaged radius of 10 µm and a length of about 1 m, then one can estimate a weight of about 0.01 mN, which is also the order of magnitude of the contribution of F_{grav}.

The *inertial force* F_{inert} is caused by acceleration of the polymeric material from the initial velocity v_0 at the exit point of the spinneret to the velocity $v(x)$ at any distance x, at least to the final take-up velocity v_{L}. The changes in speed directly affect the inertial force:

$$\frac{\mathrm{d}F_{\mathrm{inert}}}{\mathrm{d}x} = Q\,\frac{\mathrm{d}v}{\mathrm{d}x} \tag{3.15}$$

or, after integration with respect to distance x follows

$$F_{\text{inert}}(x) = Q \cdot \big(v(x) - v_0\big). \tag{3.16}$$

The assumption of a filament velocity of 3000 m/min for example and again a radius of 10 µm leads to an estimated value of $F_{\text{inert}} \approx 1$ mN.

The discussion of *air drag force* F_{drag} seems to be a little bit more difficult. The air drag force acting on a filament with circular cross section (radius R) can be written in the form

$$\frac{\mathrm{d}F_{\text{drag}}}{\mathrm{d}x} = 2\,\pi\,R(x)\,\tau_{\text{f}}(x)\,, \tag{3.17}$$

where τ_{f} is the shear stress at the filament surface to the surrounding air. The shear stress is often expressed in terms of the air friction coefficient c_{f}

$$\tau_{\text{f}} = \frac{1}{2}\,\varrho_{\text{air}}\,v^2(x) \cdot c_{\text{f}}\,, \tag{3.18}$$

where ϱ_{air} denotes the air mass density. Unfortunately, the air friction coefficient c_{f} depends on the current state of air flow within the fibre formation region. A short discussion about the interaction between the fibre and its environment, including both heat transfer (Nu-number) and momentum transfer (air friction coefficient c_{f}), is presented in Sect. 3.1.3. Here it is to be remarked that an often used formula to describe the air drag coefficient is that of Hamana [29]:

$$c_{\text{f}} = 0.37 \cdot Re^{-0.61} \tag{3.19}$$

or to be more general $c_{\text{f}} = a \cdot Re^b$, with the different parameters a and b. Re denotes the non-dimensional Reynolds number. The Reynolds number itself is given by

$$Re(x) = \frac{\varrho_{\text{air}} \cdot v(x) \cdot 2R(x)}{\eta_{\text{air}}} = \frac{v(x) \cdot 2\,R(x)}{\nu_{\text{air}}}, \tag{3.20}$$

where η_{air} is the dynamic viscosity of air, and the fraction $\nu_{\text{air}} = \eta_{\text{air}}/\varrho_{\text{air}}$ is called the kinematic viscosity of air.

Integrating Eq. 3.17 with 3.18 leads to

$$F_{\text{drag}}(x) = 2\,\pi \int_0^x R(x')\frac{\varrho_{\text{air}}}{2}\,v^2(x')\,c_{\text{f}}(x')\,dx' \tag{3.21}$$

and a rough estimation shows that the air drag contribution can reach similar magnitudes compared to the inertial force, especially at high filament velocity v.

3.1.3 Interaction Between Fibre and Environment

The following section deals with heat and momentum transfer from the fibre surface to the environment in more detail. Therefore, the equations for the Nusselt number Nu and the air friction coefficient c_{f} are presented.

Heat Transfer

The heat transfer from the fibre surface to the ambient medium (usually air) involves the mechanisms *radiation*, *free convection*, and *forced convection* (Ziabicki [274]). The contributions from radiation and free convection are often neglected or sometimes empirically incorporated into the model by the chosen relationships for the heat transfer coefficient resp. Nusselt number [25, 26, 38, 59, 62, 63, 68, 196]. However, some more recent investigations also show the influence of radiation [203, 204].

Radiation. Due to radiation, the heat transfer coefficient α_r is strongly dependent upon the temperature T

$$\alpha_\mathrm{r}(T) = \sigma_\mathrm{SB} \cdot \varepsilon_\mathrm{m} \cdot \frac{T^4 - T_\mathrm{air}^4}{T - T_\mathrm{air}} \,, \tag{3.22}$$

where σ_SB is the Stephan-Boltzmann constant and ε_m is the emissivity of the polymeric material. Replacing the heat transfer coefficient with the non-dimensional Nusselt number Nu_r (Eq. 3.6) for radiation then follows

$$Nu_\mathrm{r} = \mathrm{const} \cdot D \cdot \frac{T^4 - T_\mathrm{air}^4}{T - T_\mathrm{air}} \tag{3.23}$$

with const $\approx 1.7 \cdot 10^{-6}\,(\mathrm{m} \cdot \mathrm{K}^3)^{-1}$.

Figure 3.5 shows Nusselt numbers for the radiation heat transfer vs. temperature for different fibre thicknesses. It can be seen that radiation in the temperature range of $T = 50 \ldots 300\,^\circ\mathrm{C}$ for polymer melt spinning has very little effect, only directly below the spinneret ($T = 200 \ldots 300\,^\circ\mathrm{C}$, $D = 300\ \mu\mathrm{m}$) the Nusselt number can reach values between $0.1 \ldots 0.2$. This is equal $5 \ldots 20\%$ of the convective heat transfer (see below).

Convection. The *free (natural) convective heat transfer* is a typical heat transfer mechanism for stationary systems and is concerned with the movement of the ambient medium (air) caused by thermal expansion and density variation resulting from the related temperature field. The non-dimensional Nusselt number Nu_n for free (natural) convection can be written as a function of two other non-dimensional numbers, namely the Grashof number Gr, and the Prandtl number Pr [185]

$$Nu_\mathrm{n} = Nu_\mathrm{n}(Gr, Pr)\,, \tag{3.24}$$

where the Grashof number is given by $Gr = g\,\beta_\mathrm{air}\,(T - T_\mathrm{air})\,D^3$, with β_air as the thermal expansion coefficient of air, and the Prandtl number of air is $Pr = \eta_\mathrm{air}\,c_\mathrm{p,air}/\lambda_\mathrm{air}$. Fibre cooling by means of free convection depends on the temperature difference between fibre and ambient medium and becomes an essential factor at low fibre velocities, especially near the spinneret. Near the spinneret the high temperature of the spinning block brings forth additional

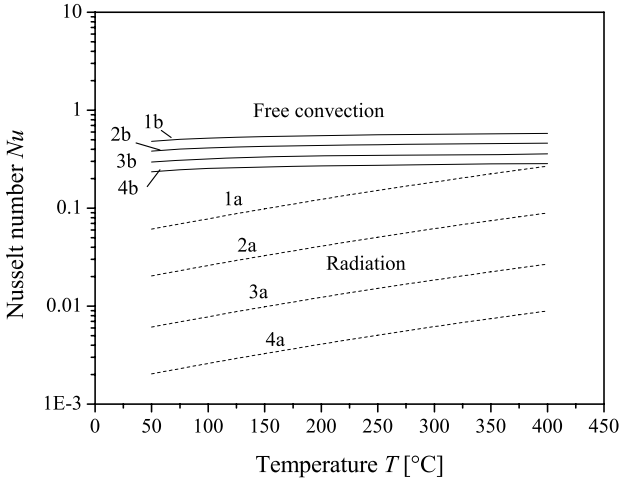

Fig. 3.5. NUSSELT number Nu vs. temperature T for different diameters D, resulting a) from heat radiation (Eq. 3.23), b) from free convection ($Nu = 0.65(Gr \cdot Pr)^{0.07}$, after [186]), diameters: 1 – 300 µm, 2 – 100 µm, 3 – 30 µm, 4 – 10 µm; temperature of ambient air: $T_{\mathrm{air}} = 25\,℃$

complications regarding the air flow. Careful design of the spinning block is required in order to reduce turbulences and improve the stability of the spinning process.

Resulting NUSSELT numbers for free convection, calculated from an empirical correlation which was determined from analyzing the free convection over thin wires [186] are shown in Fig. 3.5.

Fibre cooling in melt spinning is mainly related to the *forced convective heat transfer*. The filaments move with increasing velocity and can be additionally quenched by cross air flow. The NUSSELT number Nu_{f} for the forced convection can depend upon the exposed length x of the filaments (in parallel flow), but the main contributions are given by the parallel and/or transverse air flow described with the related REYNOLDS numbers:

$$Nu_{\mathrm{f}} = Nu_{\mathrm{f}}(Re_{\parallel}, Re_{\perp}, x, Pr) \; . \tag{3.25}$$

Many authors have developed relations to describe the heat transfer using both boundary layer theory or experimental investigations. Some earlier expressions are summarised by ZIABICKI [184, 274]. The formula developed by KASE and MATSUO is often used [25]:

$$Nu_{\mathrm{f}} = 0.42 Re_{\parallel}^{0.334} \left(1 + \left(\frac{8\, v_{\perp}}{v} \right)^2 \right)^{0.167} \; , \tag{3.26}$$

which can be rearranged to the more general relationship

$$Nu_{\mathrm{f}} = a \left(Re_{\parallel}^2 + b \cdot Re_{\perp}^2 \right)^c \; , \tag{3.27}$$

Table 3.2. Relationships for heat transfer (NUSSELT number) in melt spinning

Equation for Nu-number	References and conditions
only parallel flow	
$0.76 Re_{\parallel}^{0.38}$	Andrews (1959) [24]
$0.42 Re_{\parallel}^{0.334}$	Kase, Matsuo (1965) [25]
$0.10 + 0.15 Re_{\parallel}^{0.36}$	Sano (1966) [189]
$0.53 Re_{\parallel}^{0.33}$	Copley (1967) [190]
$0.325 Re_{\parallel}^{0.3}$	Glicksman (1968) [192]
$0.76 Re_{\parallel}^{0.41}$	Conti (1970) [193]
$0.25 + 0.15 Re_{\parallel}^{0.36}$	Zieminski (1985) [194]
$0.16 Re_{\parallel}^{0.50}$	slow melt spinning of PEEK, Ohkoshi (1993) [202]
$0.42 Re_{\parallel}^{0.344} Ra^{0.13}$	melt spinning of PEEK, Golzar (2004) [204]
$3.0 Re_{\parallel}^{-0.22}$	melt spinning of PEEK, Golzar (2004) [204]
only transverse flow	
$0.891 Re_{\perp}^{0.33}$	$1 < Re_{\perp} < 4$, Hilpert (1933) [205]
$0.821 Re_{\perp}^{0.385}$	$4 < Re_{\perp} < 40$, dito
$0.615 Re_{\perp}^{0.466}$	$40 < Re_{\perp} < 4000$, dito
$0.32 + 0.67 Re_{\perp}^{0.52}$	$0.1 < Re_{\perp} < 10^3$, McAdams (1954) [206]
$0.38 Re_{\perp}^{0.6}$	$10^3 < Re_{\perp} < 5 \cdot 10^4$, dito
parallel and transverse flow	
$0.42\left(Re_{\parallel}^2 + 64 Re_{\perp}^2\right)^{0.167}$	(*) Kase, Matsuo (1965) [25]
$0.28\left(Re_{\parallel}^2 + 1024 Re_{\perp}^2\right)^{0.17}$	(**) Brünig (1999) [207]

here with parameters $a = 0.42$, $b = 64$, $c = 0.167$. $Re_{\parallel}$ and $Re_{\perp}$ are the REYNOLDS numbers related to the parallel and cross air flow, defined as follows

$$Re_{\parallel}(x) = \frac{v_{\parallel}(x) \cdot D(x)}{\nu_{\text{air}}} \,, \tag{3.28}$$

$$Re_{\perp}(x) = \frac{v_{\perp}(x) \cdot D(x)}{\nu_{\text{air}}} \,, \tag{3.29}$$

where $v_{\parallel}$ is the axial (difference) velocity between fiber and ambient air, and $v_{\perp}$ is the cross air velocity, $\nu_{\text{air}} = \eta_{\text{air}}/\varrho_{\text{air}}$ is the kinematic viscosity of air, respectively. According to Eq. 3.10 it is possible to recalculate the total NUSSELT number for different spinning conditions, by carefully measuring the fibre temperature $T(x)$ simultaneously with fibre diameter $D(x)$ and/or velocity $v(x)$, if no crystallisation occurs:

$$Nu = -\frac{\mathrm{d}}{\mathrm{d}x} \ln\left(T(x) - T_{\text{air}}\right) \cdot \frac{Q\, c_{\text{p}}}{\pi\, \lambda_{\text{air}}} \,. \tag{3.30}$$

The experimental investigations can be carried out under different conditions: heated wires or filaments, running in stationary air, or stationary wires or filaments in steady air flow, and so on.

Table 3.2 and Fig. 3.6 show some examples for the relationship between the NUSSELT number and REYNOLDS number.

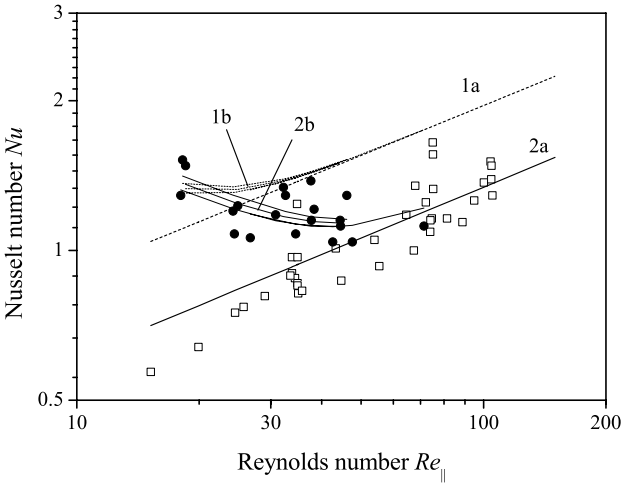

Fig. 3.6. NUSSELT number Nu vs. REYNOLDS number $Re_{\parallel}$, *symbols*: recalculated from experimental data, *open symbols:* without quenching air ($Re_{\perp} = 0$ (data source: recalculated from BRAGATO, GIANOTTO [187], *closed symbols:* with quenching air ($v_{\text{air}} = 0.4$ m/s, data source: recalculated from HABERKORN et al. [188], 1 – calc. after Eq. (*) in Table 3.2, 2 – calc. after Eq. (**) in Table 3.2, a) without quenching air ($Re_{\perp} = 0$), b) with quenching air ($v_{\text{air}} = 0.4$ m/s, $Re_{\perp} > 0$)

Air Friction

Equation (3.18) describes the friction-caused momentum transfer between the fibre surface and surrounding air. Similar to heat transfer, the air friction coefficient c_{f} was also investigated by several authors [53–55,82,208–211] both experimentally and by using laminar and turbulent boundary layer theory. Most results for the air drag coefficient have led to a relationship in the following manner

$$c_{\text{f}} = a\, Re^{b} \tag{3.31}$$

with non-dimensional REYNOLDS number Re related to the filament diameter and with different parameters a and b. Often used are the numbers given by HAMANA [29] with $a = 0.37$ and $b = -0.61$. A summary of different formulas

Table 3.3. Relationships for momentum transfer (air friction coefficient c_f) in melt spinning: $c_f = a \cdot Re^b$, after Shimizu et al. [59], Table 4

a	a^*	b	References and conditions
4.8	-	-1	Sakiadis (1961), laminar theory
1.8	-	-0.5	Sakiadis (1961), laminar theory [208–210]
5.0	-	-1	Higuchi, Katsu (1960), $0.04 < Re < 0.2$, (a) [72]
1.23	0.4	-0.81	Kase, Matsuo (1967), $3 < Re < 100$, (b) [26]
0.68	0.39 . . . 0.41	-0.8	Sano, Orii (1968), $10 < Re < 50$, (d) [73]
0.65	0.5	-0.7	Glicksman (1968), $4 < Re < 100$, (d) [192]
	0.37	-0.61	Hamana (1968) [29]
	1.78		Fukuda (1966), $5 < Re < 20$, (b) [74]
	1.3		Thompson (1953), $20 < Re < 150$, (b) [75]
	0.84		Anderson, Stubbs (1958), $10 < Re < 60$, (b) [76]
	0.77		Shimizu, Okui (1983), $50 < Re < 400$, (b,e) [53]
	0.41		Gould, Smith (1980), $20 < Re < 200$, (b) [211]
	0.56		Selwood (1962), $5 < Re < 54$, (c) [77]
	0.31 . . . 0.71		Kwon, Prevorsek (1979), $3 < Re < 30$, (c) [182]
	0.5		Shimizu, Okui (1983), $40 < Re < 250$, (d) [53]
	0.39 . . . 0.23		Shimizu, Okui (1983), $25 < Re < 70$, (d) [53]
	0.37		Matsui (1976), (d) [82]

a^* recalculated from measurements under the condition that $b = -0.61$, measurements made (a) on filaments falling in still air, (b) stationary filaments in airstream, (c) moving filaments in still air, (d) filaments spun into still air, (e) filaments spun into airstream

for Eq. 3.31 can be found in literary source [216] and some examples are shown in Table 3.3 [59].

It is surprising that the most published relations do not describe the influence of quenching cross air on the air friction coefficient. But a simple consideration leads to the assumption that with increasing quenching cross air velocity $v_\perp$ the air friction coefficient c_f must also increase. The air flow perpendicular to the fibre axis disturbs the originally axial symmetric boundary layer surrounding the fibre and leads to an additional momentum flux, analogous to the additional heat flux in the case of heat transfer (3.26). Because of the similarity of both transfer effects it was proposed to consider the influence of quenching air by means of both REYNOLDS numbers $Re_\parallel$ and $Re_\perp$ [207]:

$$c_f = c_f(Re_\parallel, Re_\perp) \; . \tag{3.32}$$

To estimate the parameters in Eq. 3.32 a boundary layer calculation and several fibre spinning experiments with different profiles of quenching air were conducted and evaluated. The investigations led to the following result

$$c_\mathrm{f} = \frac{a}{Re_\parallel}\left(Re_\parallel^2 + b\,Re_\perp^2\right)^c \quad \text{with} \quad a = 0.33,\ b = 4096,\ c = 0.2\,. \tag{3.33}$$

Figure 3.7 shows the influence of both effects: the air friction coefficient c_f is depicted there dependent upon the parallel REYNOLDS number $Re_\parallel$ and for different cross quenching REYNOLDS numbers $Re_\perp$. Usually in melt spinning the REYNOLDS numbers are in the following ranges: $5 < Re_\parallel < 150$ and $0 < Re_\perp < 5$.

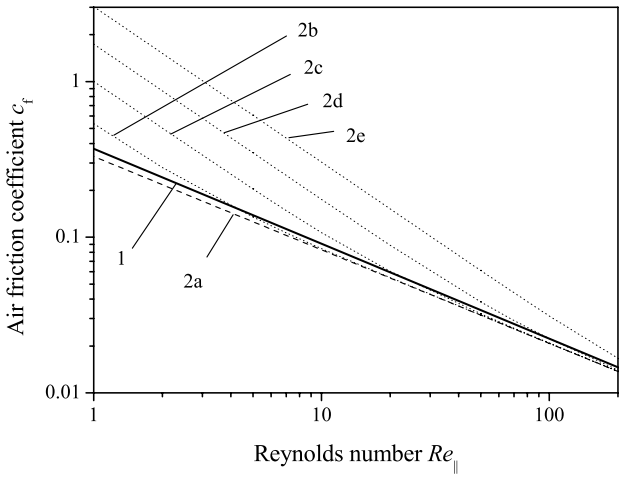

Fig. 3.7. Air friction coefficient c_f vs. REYNOLDS number $Re_\parallel$, 1 – $c_\mathrm{f} = 0.37 Re^{-0.61}$ (Hamana [29]), 2 – Eq. 3.33, a) $Re_\perp = 0$, b) $Re_\perp = 0.05$, c) $Re_\perp = 0.25$, d) $Re_\perp = 1.0$, e) $Re_\perp = 4.0$

The influence of the quenching cross air on the air friction coefficient leads to an interesting effect which is unfortunately often neglected in modelling: A strong quenching air profile causes a high cooling rate and therefore a short fibre formation zone with a short fibre length exposed to air friction force. But on the other hand, increasing quenching air flow leads to an increase of the air friction coefficient c_f. Both effects, the shorten fibre formation zone and the higher air friction coefficient are in competition. This means that the total air friction force and at least the resulting fibre stress at the solidification point can decrease with increasing quenching air flow, but it is also possible that they can increase with increasing quenching air flow. How the resulting fibre orientation (and also the resulting fibre properties like the elongation to break) changes with quenching air flow conditions depends on the current spinning conditions.

3.1.4 Response of the Polymer Melt

Shear flow of the polymeric melt takes place inside the capillary of the die. After leaving the die exit, elongational flow takes place within the fibre formation zone until at least the polymer melt stream solidifies to the final fibre. Only the elongational flow after leaving the capillary die exit and no flow behaviour inside the spinneret should be regarded: The elongation $\varepsilon(x)$, depending on distance x from the spinneret, is defined by the logarithmic HENCKY measure

$$\varepsilon(x) = \ln \frac{v(x)}{v_0} \,, \tag{3.34}$$

where v_0 is the (mean) extrusion velocity at the spinneret exit. Comparing the definition above with the normally used relation for extension (see Fig. 3.8) the equivalence for small elongations becomes obvious: $\varepsilon = \ln(l/l_0) = \ln(1 + \Delta l/l_0) \rightarrow \varepsilon = \Delta l/l_0$ for $\Delta l \ll l_0$.

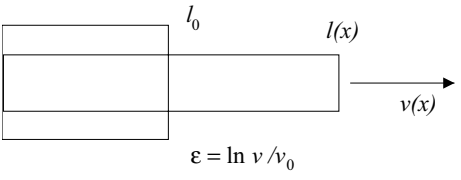

Fig. 3.8. Definition of elongation: HENCKY measure

For modelling the elongational flow, a suitable constitutive equation is necessary. It should describe the polymer response depending on the applied tensile force in a practicable manner, that is the relation between stress σ and strain ε of the fibre from the spinneret to the take-up device sufficient for any treatment in an engineering approach.

The stress-strain behaviour is controlled by the rheological properties of the polymeric material. Therefore, the spinline stress[1] σ is given by the (axial) tensile force $F = F_{\text{rheo}}$ divided by fibre cross section A

$$\sigma(x) = \frac{F_{\text{rheo}}(x)}{A(x)} \,. \tag{3.35}$$

Several constitutive equations have been developed either on the basis of continuum mechanics or under consideration of the molecular structure of the material by means of statistical methods. For modelling purposes of fibre formation mostly viscous and/or visco-elastic phenomenological relationships [25, 26, 99–102, 155–158, 196] are applied.

[1] In a more detailed theory of flow problems, the stress tensor $\underline{\sigma}$ is related to any kinematic tensor, and tension is described by the normal stress difference $\Delta\sigma = \sigma_{xx} - \sigma_{rr}$ of the components of the stress tensor $\underline{\sigma}$

Viscous and Visco-elastic Behaviour

The simplest engineering models for stress-strain behaviour are the basic rheological bodies NEWTON dashpot for purely viscous behaviour and HOOK's spring for purely elastic behaviour. In general, molten polymers are visco-elastic fluids. They show both viscous and elastic behaviour in their response to applied stress (see Fig. 3.9). The relation between viscous and elastic deformation can essentially influence the *spinnability* of a polymer (for further discussion see Sect. 3.3, visco-elasticity also gives reason for the concept of the so-called *apparent elongational viscosity*). The viscous behaviour dominates the elongational flow at comparatively low fibre velocity near the spinneret, but the influence of the elastic part becomes more and more important with increasing velocity (especially near the solidification region). Under certain conditions the *necking effect* can occur, that is the sudden reduction of the filament cross-sectional area within a short range because of a dramatic increase in the filament velocity. The necking region is very sensitive to the relationship of viscous and elastic materials behaviour. After solidication there is only the transportation of the fibre and a (more or less) purely elastic deformation up to the take-up device. Nevertheless it is often possible to get reasonable results for describing and simulating the course of melt spinning of common polymers without taking into account the elastic effects. But on the other hand, including the elastic deformation behaviour, some possibilities for calculating the textile properties are given (e. g. the elongation to break, see Sect. 3.1.6). In the following paragraphs some often used constitutive equations will be presented.

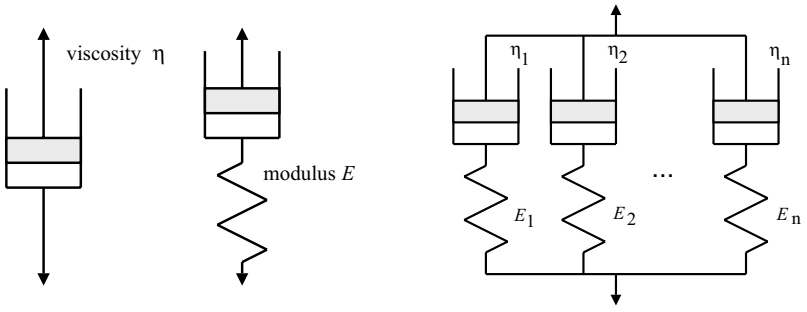

Fig. 3.9. Model of purely viscous (NEWTON) and visco-elastic (MAXWELL) rheological behaviour (*left*); spectral model, series of MAXWELL-bodies (*right*)

Newton model: Purely viscous flow. The mechanical model of the purely viscous elongation is based on the dashpot approach Fig. 3.9 (left side) and the stress-strain-relation is given by the simple constitutive equation

$$\sigma = \eta \cdot \dot{\varepsilon}_{\mathrm{v}} \,, \tag{3.36}$$

where $\dot{\varepsilon}_\mathrm{v} = \mathrm{d}\varepsilon_\mathrm{v}/\mathrm{d}t$ is the viscous deformation rate (strain rate) and η is the *elongational viscosity*. For constant applied stress the piston inside the dashpot moves at a constant strain rate. Under the steady state conditions ($\varepsilon = \varepsilon(x(t))$) and with the definition of Eq. 3.34 then Eq. 3.36 becomes

$$\sigma = \eta \cdot \frac{\mathrm{d}v}{\mathrm{d}x} \tag{3.37}$$

because of the equivalence

$$\frac{\mathrm{d}\varepsilon}{\mathrm{d}t} = \frac{\mathrm{d}\varepsilon}{\mathrm{d}x} \cdot \frac{\mathrm{d}x}{\mathrm{d}t} = \frac{1}{v} \cdot \frac{\mathrm{d}v}{\mathrm{d}x} \cdot v = \frac{\mathrm{d}v}{\mathrm{d}x} \; . \tag{3.38}$$

Example: Constant tensile force. The course of fibre formation can be discussed (after Ziabicki [184]) for the viscous deformation in a simple manner assuming a constant tensile force $F(x) = F_\mathrm{c}$. Neglecting all the contributions of inertia, gravitation, air friction, and surface tension to the force balance equation (3.11a) we get

$$\sigma(x) = \frac{F_\mathrm{c}}{A(x)} = F_\mathrm{c} \cdot \frac{\varrho_\mathrm{p} \cdot v(x)}{Q} \tag{3.39a}$$

$$= \eta \cdot \frac{\mathrm{d}v}{\mathrm{d}x} \; . \tag{3.39b}$$

This leads to the differential equation for the velocity v

$$\eta \cdot \frac{\mathrm{d}v}{\mathrm{d}x} = C \cdot v(x), \qquad C = \varrho_\mathrm{p} \cdot \frac{F_\mathrm{c}}{Q} \tag{3.40}$$

which can be integrated to

$$v(x) = v_0 \cdot \exp\left(C \cdot x \cdot \Phi(x)\right) \; , \tag{3.41}$$

where the function $\Phi(x)$ is given by

$$\Phi(x) = \frac{1}{x} \int_0^x \frac{1}{\eta(x')} dx' \; . \tag{3.42}$$

The constant force F_c is related to the boundary conditions

$$v(x = 0) = v_0$$
$$v(x = L) = v_\mathrm{L}$$

through

$$F_\mathrm{c} = \frac{Q}{\varrho_\mathrm{p}} \cdot \frac{L}{\Phi(L)} \cdot \ln\left(\frac{v_\mathrm{L}}{v_0}\right) \; . \tag{3.43}$$

The function $\Phi(x)$ describes the so-called *fluidity* of the polymeric material – the mean value of the reciprocal viscosity over certain length. An

exponentially increasing elongational flow (Eq. 3.41) results from constant viscosity η (and constant fluidity Φ). But in melt spinning the temperature along the spinning line decreases, thus the viscosity increases with increasing distance, and the slope $\mathrm{d}v/\mathrm{d}x$ also more and more decreases. Assuming that at the solidification point the viscosity becomes infinitely large, the velocity then reaches its final value v_L. The resulting behaviour is the characteristically "S-shaped" course of velocity vs. distance for purely viscous behaviour. Figure 3.10 shows an example for two different cases of fibre cooling with following conditions:

Fibre temperature T (in °C):	$T_1(x) = 20 + 280\exp(-x/0.60)$
	$T_2(x) = 20 + 280\exp(-x/0.30)$
Viscosity η (in Pa·s) :	$\eta(T) = 0.015\exp(\frac{5200}{T+273})$ for $T \geq 70$°C
	$\eta(T) = \infty$ for $T < 70$°C
Final draw down ratio :	$v_\mathrm{L}/v_0 = 300$.

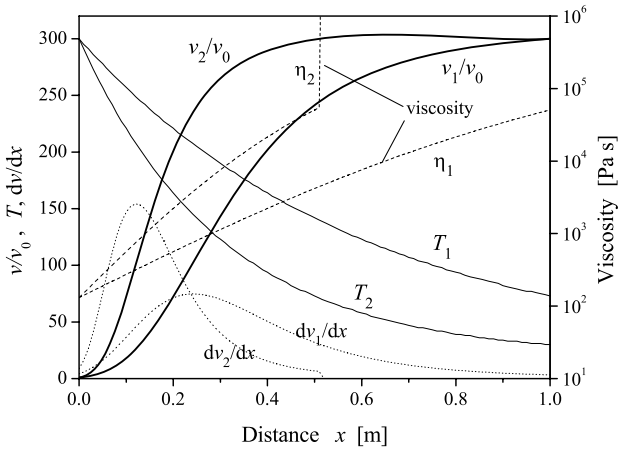

Fig. 3.10. Example of fibre formation with constant tensile force F_0 and two different cooling lengths: 1 – slow cooling, cooling length $L_\mathrm{c} = 0.60$ m; 2 – fast cooling, $L_\mathrm{c} = 0.30$ m; NEWTONian flow behaviour, draw down ratio $ddr = 300$

Maxwell model: Visco-elastic behaviour. The mechanical model consists of the combination of dashpot and spring in series (Fig. 3.9). The applied force causes the (ideal) spring to an immediate elongational elastic deformation (orientational deformation) ε_o proportional to the applied stress σ. The same stress acts on the dashpot and causes the viscous elongational deformation ε_v. The total deformation ε of the MAXWELL body is now the sum of both parts [280, 281]:

$$\varepsilon = \varepsilon_\mathrm{v} + \varepsilon_\mathrm{o} \tag{3.44}$$

with

$$\sigma = \eta \cdot \dot{\varepsilon}_{\mathrm{v}} = E \cdot \varepsilon_{\mathrm{o}} \ , \tag{3.45}$$

where E is the elongational modulus of the spring. Modulus E and viscosity η are the two material properties describing the deformation behaviour of the MAXWELL body. Often the modulus E is used together with the *relaxation time* λ with

$$\lambda = \frac{\eta}{E} \ . \tag{3.46}$$

The constitutive equation (considering the stationarity behaviour) of the MAXWELL model is given by

$$\sigma + \frac{\eta}{E} \cdot v \cdot \frac{\mathrm{d}\sigma}{\mathrm{d}x} = \eta \cdot \frac{\mathrm{d}v}{\mathrm{d}x} \tag{3.47}$$

or, expressed in terms of the relaxation time λ as

$$\sigma + \lambda \cdot v \cdot \frac{\mathrm{d}\sigma}{\mathrm{d}x} = E \cdot \lambda \cdot \frac{\mathrm{d}v}{\mathrm{d}x} \ . \tag{3.48}$$

Approaching a spectral series of $i = 1...N$ MAXWELL bodies (Fig. 3.9, right) the corresponding relation is given by

$$\sigma + \sum_i \lambda_i \cdot v \cdot \frac{\mathrm{d}\sigma}{\mathrm{d}x} = \sum_i E_i \cdot \lambda_i \cdot \frac{\mathrm{d}v}{\mathrm{d}x} \ . \tag{3.49}$$

Generalisations. The constitutive equations above describe a simple one-dimensional model for the extension in spinning-direction. All effects related to the radial stress and deformation components of the uniaxial deformation are neglected. Considering the three-dimensionality of the real deformation process, a more detailed analysis needs to be carried out. This can be done by means of precise formulation with the help of tensor-calculus. Nevertheless, the *thin-filament approximation* in which the radial dependence of axial velocity (and temperature) $\partial v/\partial r = 0$ (and $\partial T/\partial r = 0$) is neglected should further be used. For the incompressible axis symmetrical and uniaxial elongational deformation, the deformation rate tensor $\underline{\dot{\varepsilon}}$ and the stress tensor $\underline{\sigma}$ are given as follows:

$$\underline{\dot{\varepsilon}} = \frac{\mathrm{d}v}{\mathrm{d}x} \begin{pmatrix} 1 & 0 & 0 \\ 0 & -\frac{1}{2} & 0 \\ 0 & 0 & -\frac{1}{2} \end{pmatrix} \qquad \text{and} \qquad \underline{\sigma} = \begin{pmatrix} \sigma_{\mathrm{xx}} & 0 & 0 \\ 0 & \sigma_{\mathrm{rr}} & 0 \\ 0 & 0 & \sigma_{\mathrm{rr}} \end{pmatrix} \ . \tag{3.50}$$

A possible generalisation for visco-elastic behaviour using the stress and deformation rate tensors is the *upper-convected* MAXWELL model with relaxation time λ and modulus G:

$$\sigma_{xx} + \lambda \left(v \frac{d\sigma_{xx}}{dx} - 2 \frac{dv}{dx} \sigma_{xx} \right) = 2 G \lambda \frac{dv}{dx} , \tag{3.51}$$

$$\sigma_{rr} + \lambda \left(v \frac{d\sigma_{rr}}{dx} + \frac{dv}{dx} \sigma_{rr} \right) = - G \lambda \frac{dv}{dx} . \tag{3.52}$$

The spinning line tension (3.35) is now related to the normal stress difference $\Delta\sigma = \sigma_{xx} - \sigma_{rr}$ with

$$\Delta\sigma = \sigma_{xx} - \sigma_{rr} = \frac{F}{A} . \tag{3.53}$$

The PHAN-TIEN-TANNER model [212, 213] is another generalised constitutive equation based on a special type of network theory to describe a nonlinear strain-softening behaviour. It helps to describe the necking effect at higher spinning speeds. The constitutive equations are:

$$K \cdot \sigma_{xx} + \lambda \left(v \frac{d\sigma_{xx}}{dx} - 2 \frac{dv}{dx} \sigma_{xx} \right) = 2 G \lambda \frac{dv}{dx} , \tag{3.54}$$

$$K \cdot \sigma_{rr} + \lambda \left(v \frac{d\sigma_{rr}}{dx} + \frac{dv}{dx} \sigma_{rr} \right) = - G \lambda \frac{dv}{dx} , \tag{3.55}$$

$$K = \exp \left(\frac{\alpha}{G} \cdot \operatorname{tr} \underline{\sigma} \right) . \tag{3.56}$$

The parameter α describes the additional strain softening effect. For $\alpha \to 0$ in Eq. 3.56 the upper-convected MAXWELL equation above follows. $\operatorname{tr} \underline{\sigma} = \sigma_{xx} + 2\,\sigma_{rr}$ denotes the trace of the stress-tensor.

Of course it is also possible to use combinations of different MAXWELL or generalised MAXWELL elements. This leads to a discrete or continuous spectrum with more than one relaxation time and modulus, respectively (Fig. 3.9). Some investigators also describe the viscosity by means of a power law such as

$$\eta(T, \dot{\varepsilon}) = \eta_0(T) \cdot \left(\frac{dv}{dx} \right)^{n-1} , \quad n < 1 , \tag{3.57}$$

or a generalised power law equation similar to the CROSS-CARREAU type e. g.

$$\eta(T, \dot{\varepsilon}) = \frac{\eta_0(T)}{1 + a \left(\eta_0(T) \frac{dv}{dx} \right)^b} , \tag{3.58}$$

respectively, to describe the additional influence of the strain rate $\dot{\varepsilon} = dv/dx$ and the deviation of the resulting viscosity from the NEWTONian behaviour with corresponding parameter n, a, b.

Solidification

The glass transition point marks the temperature T_g at which the mobility of the polymer chains prevent any further deformation flow. Some of the typical values are listed in Table 3.4.

Table 3.4. Glass transition temperature T_g of melt spinning polymers

polymer	T_g in ℃
PET – poly(ethylene terephthalate)	70
PA 6 – poly(amide) 6	50 . . . 55
PP – poly(propylene)	≈ -20

In reality, the flow deformation often comes to an end *before* the glass transition temperature is reached. The reason for this is that crystallisation can take place within the spinline at certain high levels of orientation and stress. The developing crystalline regions act as additional strain hardening segments. Some researchers (e. g. George [39]) investigated the solidification temperature T_s where the deformation comes to an end. They found that the solidification temperature depends upon the spinning speed and spinline stress. The solidification temperature T_s showed a step-like behaviour as function of stress σ. The solidification cannot be separated from the appearance of stress-induced crystallisation, especially in the cases of highly crystallisable polymers in melt spinning. Therefore, an empirical relation $T_s = T_s(\sigma)$ between solidification temperature and spinline stress is often used for modelling the fibre formation process .

3.1.5 Structure Development

Structure development is one of the most interesting aspects [175] in the modelling of the melt spinning process because the resulting as-spun fibre structure determines the textile fibre properties like tenacity, residual draw ratio or elongation to break. This is why a practicable and useful simulation should not stop with the calculation of fibre temperature, velocity, or stress, but should also allow for the prediction of the structural parameters and the correlated textile properties. To *quantitatively* describe the fibre formation and resulting fibre structure it is necessary to possess information on how

- the elongational flow influences molecular orientation,
- the orientation influences the crystallisation of the material,
- crystallisation occurs (nucleation and kinetics),
- orientation and crystallisation change the rheological flow properties.

Of course the effect of the heat of crystallisation should also be included. The main parameters for structure development are temperature, stress, and time. Although many researchers have investigated the melt spinning process for a long time (and with investigations still ongoing) the current models do not sufficiently consider these effects. A satisfactory description is still missing specifically for the crystallisation.

Orientation and Birefringence

The polymer deformation, in melt spinning mainly the elongational flow, causes an alignment of the polymer chain molecules. HERRMANN's orientation factor f describes the orientation of the molecular chains with respect to the fibre axis. It can be defined through different methods (e. g. X-ray scattering) as follows [173]:

$$f = \frac{3\left\langle \cos^2\theta \right\rangle - 1}{2}\,, \tag{3.59}$$

where θ is the angle between the molecular chains and the fibre axis, the brackets denote the mean value. The orientation factor f is equivalent to the second momentum $\langle P_2 \rangle$ of the development of *orientation distribution function* $N(\theta)$ to LEGENDRE polynomials P_n:

$$N(\theta) = a_0 P_0(\cos(\theta)) + a_2 P_2(cos(\theta)) + a_4 P_4(cos(\theta)) + \ldots \tag{3.60}$$

due to reasons of symmetry the odd-numbered coefficients vanish, the first three even LEGENDRE polynomials are given as follows:

$$P_0(\cos(\theta)) = 1\,, \tag{3.61a}$$

$$P_2(\cos(\theta)) = \frac{1}{2}\big(3\cos(\theta) - 1\big)\,, \tag{3.61b}$$

$$P_4(\cos(\theta)) = \frac{1}{8}\big(35\cos^4(\theta) - 30\cos^2(\theta) + 3\big)\,. \tag{3.61c}$$

The orientation distribution function $N(\theta)$ is defined at the sphere (see Fig. 3.11) and of course normalised ($\langle P_0 \rangle = 1$), therefore the second momentum $\langle P_2 \rangle$ gives us the first information about the orientation of the molecular chains:

$$\langle P_0 \rangle = 2\,\pi \int_0^\pi P_0\, N(\theta) \sin(\theta)\, d\theta = 1\,, \tag{3.62}$$

$$\langle P_2 \rangle = 2\,\pi \int_0^\pi P_2(\theta)\, N(\theta) \sin(\theta)\, d\theta \equiv f\,. \tag{3.63}$$

The orientation factor vanishes ($f = 0$) if all axes of the polymer chains are randomly distributed. It's maximum is $f = 1$ if all polymer chains align parallel to the fibre axis. The orientation of the molecular chains affects the polarisability and leads to the difference of the refractive index for linear

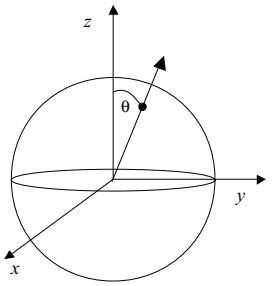

Fig. 3.11. Definition of the orientation distribution function, θ is the angle between fibre axis z and the end-to-end-vector of molecular chains, the distribution of the orientation vectors about the sphere defines $N(\theta)$

polarised light parallel and perpendicular to the fibre axis, called birefringence $\Delta n = n_{\parallel} - n_{\perp}$ (Fig. 3.12). The birefringence is related to the orientation factor as follows

$$\Delta n = f \cdot \Delta n^0 \ , \tag{3.64}$$

where Δn^0 is the maximum possible birefringence of the material (all molecular chains are aligned parallel to the fibre axis), the so-called *intrinsic birefringence*.

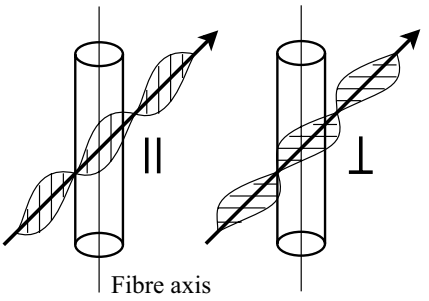

Fig. 3.12. Linear polarised light, parallel and perpendicular to fibre axis

It was found that for noncrystalline amorphous polymers and for moderate stress levels the (amorphous) birefringence Δn_{am} satisfies a simple relation to the applied stress σ, the *stress-optical law* [30]:

$$\Delta n_{\mathrm{am}} = C_{\mathrm{opt}} \cdot \sigma \ , \tag{3.65}$$

where C_{opt} is the stress-optical coefficient.

The properties of partly crystalline polymers are usually described by a two-phase model consisting of crystalline regions (fractional part X_{c}) and amorphous regions (fractional part $1 - X_{\mathrm{c}}$). Following this two-phase concept, the birefringence of a semicrystalline material can be written as [174]

$$\Delta n = (1 - X_{\mathrm{c}}) \cdot \Delta n_{\mathrm{am}} + X_{\mathrm{c}} \cdot \Delta n_{\mathrm{cr}} \tag{3.66a}$$

$$= (1 - X_{\mathrm{c}}) \cdot f_{\mathrm{am}} \, \Delta n^0_{\mathrm{am}} + X_{\mathrm{c}} \cdot f_{\mathrm{cr}} \, \Delta n^0_{\mathrm{cr}} \ . \tag{3.66b}$$

The amorphous and crystalline phases are depicted by the subscripts 'am' and 'cr'. An additional component of birefringence, the so-called 'form' birefringence, is caused by the interaction of the two phases. In most cases this form birefringence has only little effect and can be neglected. (However, if rod-like voids are generated in the fibre, sometimes the form birefringence is not negligible).

Crystallisation and Crystallinity

As mentioned above, a satisfactory and easy to handle theory of non-isothermal crystallisation within the spinline is still missing. Nevertheless, the basics of a phenomenological model will be shortly presented in the following section. For more details the interested reader is referred to separate literature [163, 214–240].

The crystallisation can be divided into *nucleation* and *crystal growth*. For higher temperatures (near the melting point) the nucleation is low and the material crystallises slowly, at lower temperatures (near the glass transition) the molecular mobility is low and the crystal growth is slow. The result is a maximum overall crystallisation rate at any intermediate temperature $T_{\max}$. The high cooling rate in melt spinning allows for only a short time interval for the temperature range where crystallisation is possible. Therefore the temperature-dependent crystallisation rate for an isotropic material $K(T, 0)$ is given by the approximation

$$K(T,0) = K_{\max} \cdot \exp\left(\frac{-4\ln(2)\,(T - T_{\max})^2}{\Delta T_{1/2}^2}\right) , \tag{3.67}$$

where $K_{\max}$ is the crystallisation rate constant at the temperature $T_{\max}$ of maximum crystallisation rate, $\Delta T_{1/2}$ is the half-width of the GAUSSian function. For a non-isotropic material with stress-related orientation $f \propto \sigma$ ZIABICKI [214, 216, 220] proposed a series expansion of the crystallisation rate $K(T, \sigma)$ to include the stress and orientation effects in the form

$$K(T,\sigma) = K(T,0) \exp\left(C_2\,\sigma^2 + C_3\,\sigma^3 + \ldots\right) , \tag{3.68}$$

where C_i are constants. The linear term in (3.68) vanishes because of thermodynamic symmetry reasons. For moderate stress the crystallisation rate is given as

$$K(T,\sigma) = K_{\max} \cdot \exp\left(\frac{-4\ln(2)\,(T - T_{\max})^2}{\Delta T_{1/2}^2} + C_2\,\sigma^2\right) . \tag{3.69}$$

It can be seen that crystallisation is extremely sensitive to orientation or stress, especially for the high-speed spinning process *stress-induced crystallisation* can be observed. Other approaches [197–200] use the quiescent crystallisation theory from HOFFMAN and LAURITZEN, expanded by the stress-orientation effect. This leads to

$$K(T,\sigma) = K_0 \cdot \exp\left(-\frac{U*}{R(T-T_\infty)} - \frac{C_1}{T\cdot\Delta T + C_2 T^2\cdot\sigma^2}\right) , \tag{3.70}$$

where U^* is the activation energy for segment motion, R is the gas constant, $\Delta T = T_\mathrm{m} - T$ is the supercooling where T_m is the melting temperature, $T_\infty = T_\mathrm{g} - 30\,\mathrm{K}$ where T_g is the glass transition temperature, and K_0, C_1, C_2 are material constants.

The development of the crystallinity X_c now is in agreement to the AVRAMI approximation given by the relation

$$\frac{\mathrm{d}X_\mathrm{c}}{\mathrm{d}t} = nK(1-X_\mathrm{c})\left[\ln\left(\frac{1}{1-X_\mathrm{c}}\right)\right]^{\frac{n-1}{n}} , \tag{3.71}$$

where n is the AVRAMI exponent, usually an integer value in the range of 1–4. With $n = 1$ at steady state conditions the simpler (and often used) equation follows:

$$\frac{\mathrm{d}X_\mathrm{c}}{\mathrm{d}x} = \frac{K(T,\sigma)}{v}\cdot(1-X_\mathrm{c}) . \tag{3.72}$$

Mostly, melt spun fibres are partially crystalline. Assuming the two-phase model of amorphous (density ϱ_am) and crystalline (density ϱ_cr) regions, the mass density ϱ_p of a partially (X_c) crystalline fibre is given by the rule of mixture:

$$\varrho_\mathrm{p}(X_\mathrm{c}) = (1-X_\mathrm{c})\,\varrho_\mathrm{am} + X_\mathrm{c}\,\varrho_\mathrm{cr} . \tag{3.73}$$

Some typical values for fibre densities and also for the densities of the amorphous and crystalline regions are presented in Table 3.5, at a temperature of 20 °C.

Table 3.5. Amorphous, crystalline and typical fibre mass densities at 20 °C

	ϱ_am in g/cm^3	ϱ_cr in g/cm^3	ϱ-fibre in g/cm^3
PET	1.335	1.455	1.34−1.38
PA 6	1.09	α-modification: 1.23	1.12−1.14
		γ-modification: 1.17	
PP	0.854	0.963	0.90−0.905

Therefore, the precise measurement of the density can be used to determine the crystallinity in the solid state of the as-spun fibre:

$$X_\mathrm{c} = \frac{\varrho_\mathrm{p} - \varrho_\mathrm{am}}{\varrho_\mathrm{cr} - \varrho_\mathrm{am}} . \tag{3.74}$$

For example, Fig. 3.13 shows the mass density of some spun PET fibres vs. spinning velocity. For a higher take-up velocity, the density increases because stress-induced crystallisation occurs and the crystallinity X_c increases.

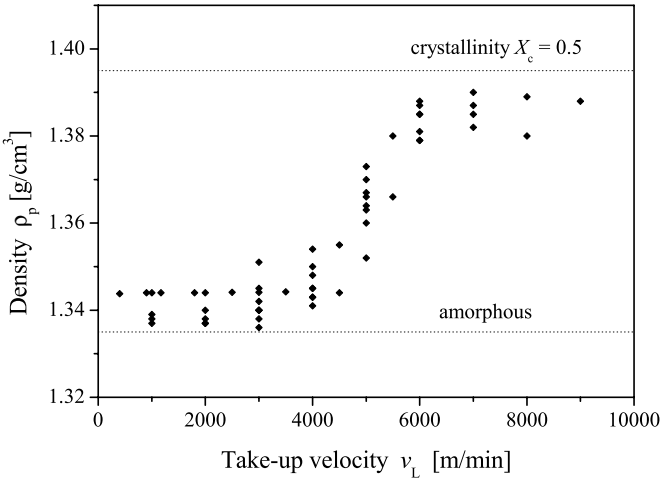

Fig. 3.13. Mass density ρ_{p} for PET vs. take-up velocity v_{L}, data points taken/recalculated from [58, 187, 241–246]

3.1.6 Material Properties of Spinnable Polymers

Mass density and specific heat capacity of melt spinnable polymers are not constant but depend on temperature and crystallinity. Elongational viscosity, relaxation time and/or modulus also depend on temperature and structural parameters. Finally the resulting fibre properties like elongation to break or tenacity are correlated with the fibre structure.

Properties of the Melt

Mass density. The mass density ϱ_{p} of molten polymers can be assumed as linear relation to the temperature T:

$$\varrho_{\mathrm{p}}(T) = \varrho_0 - \varrho_1 \cdot T\,, \quad T \text{ in } ^\circ\mathrm{C}\,. \tag{3.75}$$

Some often used values for the parameter ϱ_0 and ϱ_1 for modelling the fibre formation are shown in Table 3.6.

Table 3.6. Temperature dependence of mass density (3.75) in melt spinning

	ϱ_0 in g/cm^3	ϱ_1 in $(^\circ\mathrm{C})^{-1}$	temp. range in °C
PET	1.356	0.0005	70–300
PA 6	1.124	0.00056	55–300
PP	0.90	0.0006	25–260

Heat capacity. The specific heat capacity of polymers can be determined by analyzing their (equilibrium) melting behaviour using the established methods of differential scanning calorimetry (DSC). Regarding the thermal scans; the glass transition, the crystallisation, and the melting peaks can be observed. Therefore, the thermal analysis can also be used to calculate the degree of crystallinity of the as-spun fibres. Otherwise the melt spinning process appears in a non-equilibrium state. The process speed and cooling rate are much higher, making it impossible to apply DSC methods for observation of phase transition. The locations and amounts of latent heat which one can attain from the calorimetric scans normally cannot be used for describing the rapid fibre formation process. Regarding the tractability of the fibre formation model, the specific heat capacity c_p is often described by linear relationship to temperature T:

$$c_\mathrm{p}(T) = c_{\mathrm{p}0} + c_{\mathrm{p}1} \cdot T\,, \quad T \text{ in } ^\circ\mathrm{C}\,. \tag{3.76}$$

Table 3.7 contains some possible values for the parameter $c_{\mathrm{p}0}$ and $c_{\mathrm{p}1}$ for describing the heat capacity in the modelling of fibre formation.

Table 3.7. Temperature dependence of the specific heat capacity

	$c_{\mathrm{p}0}$ in J/(kg·K)	$c_{\mathrm{p}1}$ in $(^\circ\mathrm{C})^{-1}$	temp. range in °C
PET	1256	2.51	70–300
PA 6	2180	2.2	> 100
PP	1536	10.1	25–260

Elongational viscosity. The change of elongational viscosity with increasing distance from the spinneret, *essential*, influences the characteristic course of the spinning line (see the example of applying the constant force in Sect. 3.1.4 on page 61). The elongational viscosity η (or the relaxation time λ for the visco-elastic behaviour, respectively) generally depends upon the molecular weight M and the molecular weight distribution of the polymer. The dependence on the molecular weight often can be expressed by the intrinsic viscosity IV, or the relative solution viscosity. Sometimes it is convenient to use the melt flow rate MFR (melt flow index MFI) instead of the relative solution viscosity (e. g. for poly(propylene)). The local elongational NEWTONian viscosity $\eta(x)$ depends on the local temperature $T(x)$, and for the non-NEWTONian case the viscosity additionally depends on the local elongational deformation rate $\dot{\varepsilon}(x)$. Finally, if crystallisation occurs, the effect of the local degree of crystallinity $X_\mathrm{c}(x)$ has also to be taken into account.

The NEWTONian viscosity is usually assumed to be approximated by the ARRHENIUS equation with constant activation energy E_a:

Table 3.8. Typical melt viscosities (zero shear viscosities) of spinnable polymers

	PET	PA 6	PP
Molecular weight	19 000	17 000	200 000
Processing temperatures (°C)	285–295	260–270	230–250
Melt viscosity (Pa·s)	120–90	140–120	120–80

$$\eta(T) = \eta_0 \exp(E_\mathrm{a}/k\,T)\ , \tag{3.77}$$

where η_0 is a material constant depending on molecular weight or intrinsic viscosity and k is the BOLTZMANN constant. Equation (3.77) works well in the high temperature range above the melting point. The better alternative to the ARRHENIUS formulation within the lower temperature range, as the temperature approaches the glass transition temperature T_g, is the WILLIAMS-LANDEL-FERRY (WLF) equation with T_g and melting temperature T_m as parameters:

$$\eta(T) = \eta_1 \exp\left(\frac{-(T - T_\mathrm{m})}{(51.6 + T - T_\mathrm{g})(51.6 + T_\mathrm{m} - T_\mathrm{g})}\right)\ . \tag{3.78}$$

On the one hand, the WLF equation gives a steep rise in the vicinity of glass transition. However, on the other when solidification is reached the rise of viscosity can be assumed to reach infinity for modelling purposes.

The influence of molecular weight M (expressed by intrinsic viscosity IV or relative solution viscosity) on the elongational viscosity is usually given by the power functions

$$\eta_0 \propto M^b\,, \qquad \eta_0 \propto (IV)^c\,, \tag{3.79}$$

with exponents $b = 3.2 \ldots 3.4$, and $c = 1.8 \ldots 2.2$, respectively.

Table 3.8 shows selected parameters for typical melt viscosities of polymers (measured in oscillatory shearing). For modelling purposes, the elongational viscosity is often assumed to be approximately three times the zero shear viscosity. Some examples for the dependency of the elongational viscosity on temperature for PET are shown in Fig. 3.14 .

The dependency of the viscosity on deformation and deformation rate cannot be separated from the general visco-elastic and/or nonlinear rheological behaviour. These problems are also strongly connected with the failure behaviour of the polymer material. A short but only qualitative discussion is given in Sect. 3.3.

Another unsolved problem is the correct description of the effect of crystallinity on viscosity. There is a rapid increase of viscosity if crystallisation occurs. Usually the viscosity $\eta(T, X_\mathrm{c}) = \eta(T) f(X_\mathrm{c})$ is expressed as a product of temperature-dependent viscosity and a crystallinity-dependent function $f(X_\mathrm{c})$. There are several proposals [59, 200, 201] how to quantify the influence of crystallinity X_c on viscosity:

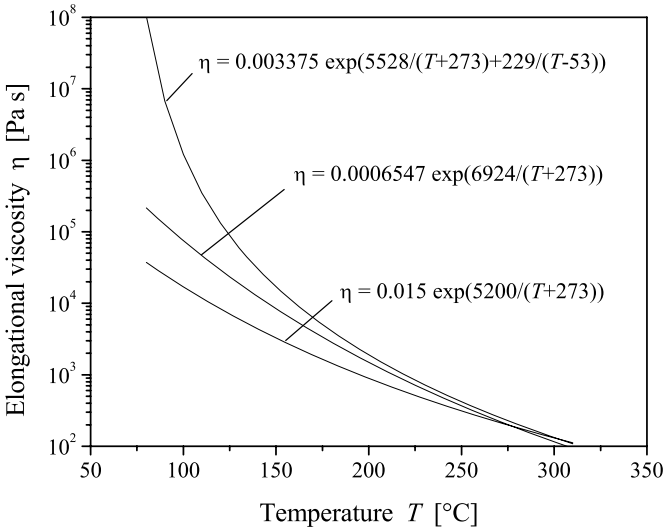

Fig. 3.14. Elongational viscosity η vs. temperature T for PET, ARRHENIUS type equations

$$\eta(T, X_\mathrm{c}) = \eta(T) \exp(a\, X_\mathrm{c}^b) \;, \tag{3.80}$$

or

$$\eta(T, X_\mathrm{c}) = \eta(T) \cdot (1 + 99\, X_\mathrm{c}) \;, \tag{3.81}$$

or

$$\eta(T, X_\mathrm{c}) = \frac{\eta(T)}{(1 - X_\mathrm{c}/X_\mathrm{crit})^\alpha} \;, \tag{3.82}$$

with parameters a, b, α; X_crit is a critical value derived from a crosslinking model where $\eta \to \infty$ when $X_\mathrm{c} \to X_\mathrm{crit}$.

Elastic modulus *E*. Little is known about the elastic modulus (or relaxation time) of the melt during elongational deformation. A possible assumption follows the network deformation concept. For example the modulus $E = \mathrm{d}\sigma/\mathrm{d}\varepsilon_\mathrm{o}$ of the GAUSSian entropic network is given by

$$E(\varepsilon_\mathrm{o}) = E_0\big(2\, \exp(2\,\varepsilon_\mathrm{o}) + \exp(-\varepsilon_\mathrm{o})\big) \;, \tag{3.83}$$

where ε_o is the elongational (orientational) deformation of the network (see also the discussion in the next paragraph), and where the parameter E_0 fits to the properties of the melt. Equation 3.83 implies that the relaxation time $\lambda = \eta/E$ has the same dependence on temperature as viscosity.

Properties of the Solid Fibre - The Network Deformation Concept

Textile properties like elongation to break and/or the tenacity of as-spun fibres are mainly determined by the orientational state reached during melt spinning [280, 281]. The orientation itself depends on the realised spinning stress.

Elongation to break. Regarding the correlation between (amorphous) orientation (birefringence Δn) and elongation to break ε_b leads to the generally accepted assumption that a maximum possible elongation ε_max may exist depending on the type of polymer. Extrapolating this relation to a hypothetic value of vanishing orientation with $\Delta n \to 0$ then allows to estimate the maximum possible elongation to break ε_max. The same procedure can be applied in principle for the behaviour of elongation to break vs. take-up velocity. Extrapolating $v_\mathrm{L} \to 0$ also leads to similar values for the maximum possible elongation to break. Figure 3.15 shows as an example the elongation to break vs. take-up velocity for as-spun PA 6 fibres at various spinning conditions. The elongation ϵ measured in percentages relates to the corresponding draw ratio DR and the logarithmic HENCKY measure ε by[2]

$$DR = 1 + \frac{\epsilon\ (\mathrm{in}\ \%)}{100\%} \quad , \qquad \varepsilon = \ln DR\ . \tag{3.84}$$

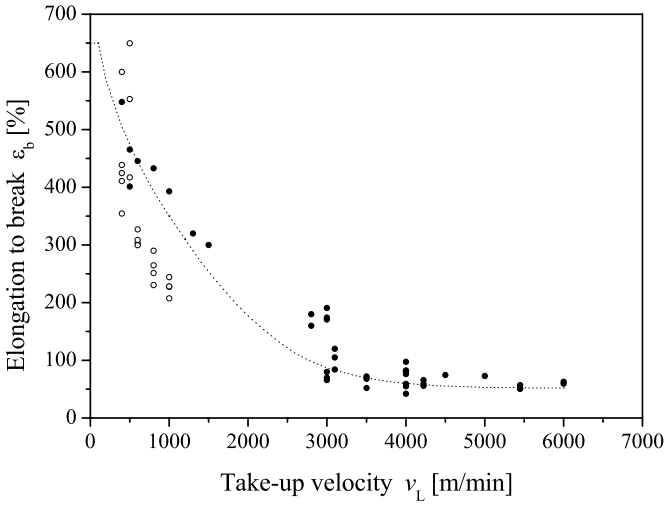

Fig. 3.15. Elongation to break ε_b vs. take-up velocity v_L; PA 6, different spinning conditions, filled symbols (•): molecular weight 16 000 – 18 000, open symbols (○): molecular weight 28 000; data source: Institute of Polymer Research Dresden

[2] The elongation measured in percentage (%) is labeled with ϵ and the corresponding logarithmic HENCKY measure is labeled with ε.

Table 3.9 contains the results for the maximum possible elongation to break $\epsilon_{\max}$ also expressed as maximum corresponding draw ratio $DR_{\max}$ and as logarithmic measure $\varepsilon_{\max}$.

Table 3.9. Maximum possible elongation of spinnable polymers

	PA 6	PET
$\epsilon_{\max}$ (in %)	650–700	800–900
$DR_{\max}$ corresponding draw ratio	7.5–8.0	9.0–10.0
$\varepsilon_{\max}$ (logarithmic HENCKY measure)	2.0–2.1	2.2–2.3

Under the assumptions

- that a maximum possible elongation $\varepsilon_{\max}$ exists and
- that each deformation (or drawing) step i is independent of the step before,

follows for the deformation steps the simple relation (in logarithmic HENCKY measure)

$$\sum_i \varepsilon_i = \varepsilon_{\max} \tag{3.85}$$

or, expressed with the corresponding draw ratios DR_i

$$\prod_i DR_i = DR_{\max} \; . \tag{3.86}$$

Applying this concept of independent deformation steps to a typical melt spinning process, one can easily calculate the residual elongation to break ϵ_{b} of the fibre after spinning and drawing:

$$\epsilon_{\mathrm{b}} \; (\mathrm{in}\%) = \left(\frac{DR_{\max}}{DR_{\mathrm{m}} \cdot DR_{\mathrm{spun}}} - 1 \right) \cdot 100 \; \% \tag{3.87a}$$

$$= \left(\frac{\exp(\varepsilon_{\max})}{DR_{\mathrm{m}} \cdot \exp(\varepsilon_{\mathrm{spun}})} - 1 \right) \cdot 100 \; \% \tag{3.87b}$$

or, vice versa the necessary machine draw ratio DR_{m} to any residual elongation to break ϵ_{b} of the final fibre after drawing if the logarithmic elongation measure $\varepsilon_{\mathrm{spun}}$ of the as-spun fibre is known:

$$DR_{\mathrm{m}} = \frac{DR_{\max}/DR_{\mathrm{spun}})}{\epsilon_{\mathrm{b}}/100\% + 1} \tag{3.88a}$$

$$= \exp(\varepsilon_{\max} - \varepsilon_{\mathrm{spun}} - \varepsilon_{\mathrm{b}}) \; . \tag{3.88b}$$

In the equations above $DR_{\mathrm{m}} = DR_1 \cdot DR_2 \cdot \ldots \cdot DR_{\mathrm{N}}$ denotes the *total draw ratio* of the (machine) drawing procedure with N drawing steps; $\varepsilon_{\max}$

is the polymer specific constant describing the maximum possible elongation. The (logarithmic) as-spun elongation $\varepsilon_{\text{spun}}$ reached in the fibre formation process correlates with the elastic elongation and orientational deformation of the visco-elastic rheological model (MAXWELL or PHAN-TIEN-TANNER) as described before: $\varepsilon_{\text{spun}} \approx \varepsilon_{\text{o}}$. Figure 3.16 depicts this concept.

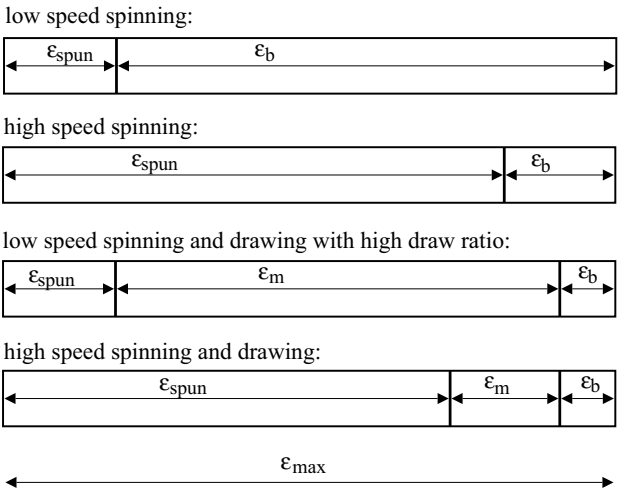

Fig. 3.16. Principle of network deformation concept: independent drawing steps

Tenacity. The tenacity TN (sometimes called strength) is defined as the breaking force F_{b} divided by the initial fineness Tt_0 of the filament at the beginning of the force-elongation experiment $TN = F_{\text{b}}/Tt_0$. Melt spun fibres often show a strain hardening behaviour with increasing elongation. On the other hand, the higher the *pre-orientation* of the fibre (resulting from take-up velocity and spinning stress) the higher the tenacity and the lower the residual elongation to break. For typical melt spinning polymers like PA and PET the product of tenacity and residual elongation to break, the *(true) stress at break*,

$$\sigma_{\text{b}} = TN \cdot \left(\frac{\epsilon_{\text{b}}\ (\text{in}\,\%)}{100\%} + 1 \right) \tag{3.89}$$

is nearly independent of pre-orientation and the resulting elongation and can be taken as a property of the polymer and its molecular weight alone. This assumption in combination with the concept of the independent deformation steps (Eq. 3.87b) allows us to predict the tenacity TN depending upon the machine draw ratio DR_{m} of the spun and drawn fibre if the elongation to break of the fibre is known:

$$TN = \frac{\sigma_\mathrm{b}}{\epsilon_\mathrm{b}(\text{in }\%)/100\% + 1} \tag{3.90}$$

$$= \sigma_\mathrm{b} \cdot \frac{\exp(\varepsilon_\mathrm{spun})}{\exp(\varepsilon_\mathrm{max})} \cdot DR_\mathrm{m} \; . \tag{3.91}$$

As a consequence, a (true) stress–(true) strain 'master'-curve of the polymer exists to which the stress-strain curves can be shifted [137,280]. The shift of each curve from the origin represents the realised pre-orientation in the spinning process, resp. the spin draw ratio DR_spun. Figure 3.17 shows the stress-strain behaviour and Fig. 3.18 shows the resulting master curve after the shifting procedure for low and high speed spinning of PA 6.

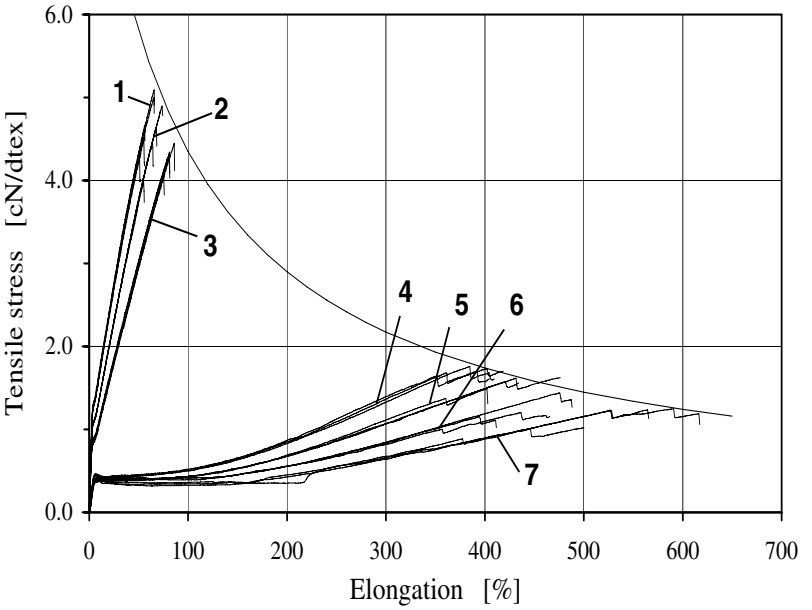

Fig. 3.17. Stress-strain behaviour of as-spun PA 6 fibres; Take-up velocities: 1 – 6000 m/min, 2 – 5000 m/min, 3 – 4000 m/min, 4 – 1000 m/min, 5 – 800 m/min, 6 – 600 m/min, 7 – 400 m/min, data source: Institute of Polymer Research Dresden; hyperbolic envelope: $\dfrac{8.6\,\mathrm{cN/dtex}}{\epsilon/100\% + 1}$

Remark. The concept of independent deformation steps is quite simple but works well in the manner of an initial approximation. A more exact analysis of properties of spun and drawn fibres shows that ε_max is not independent of the drawing procedure. There is a slight increase with increasing draw ratio $\varepsilon_\mathrm{max} = f(DR_\mathrm{m})$ to a new higher level specifically for higher drawn yarns (FDY). An analogue observation can be made for the maximum possible tenacity TN_max.

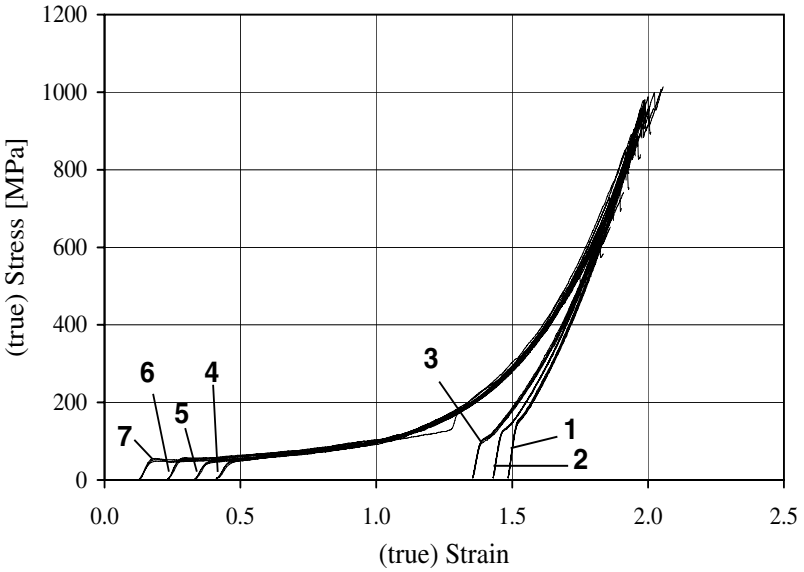

Fig. 3.18. Master curve of PA 6 fibres (true stress - true strain behaviour), shifted curves of Fig. 3.17; Take-up velocities: 1 – 6000 m/min, 2 – 5000 m/min, 3 – 4000 m/min, 4 – 1000 m/min, 5 – 800 m/min, 6 – 600 m/min, 7 – 400 m/min; data source: Institute of Polymer Research Dresden

3.1.7 Practical Modelling: Simulation of Fibre Formation

The complete set of equations which allows the simulation of the fibre formation process differs from case to case, especially with respect to the question of how the authors or investigators describe the deformation behaviour and structure development of the polymer. The available mathematical models show the progress made in the theory of fibre spinning [38,40,59,152–155,157–172,194–197,213,258] but of course they do not satisfy all experimental observations and many of them give no conclusions to the resulting *textile* fibre properties. Generally more agreement exists among the basic balance equations. The following two sections summarise the relations for the fibre formation model and give some examples for the simulation of polyamide 6 melt spinning. The equations used for the model here (specifically the correlations to textile fibre properties) have been developed over many years at the Institute of Polymer Research Dresden as a result of the collaboration with industrial and scientific partners.

Complete Set of Equations

Geometry

$$A(x) = \frac{\pi}{4} D^2(x) \; . \tag{3.92}$$

Balance equations

$$Q = \varrho_{\mathrm{p}} \cdot v \cdot A \tag{3.93}$$

$$\frac{\mathrm{d}T}{\mathrm{d}x} = -\left(T - T_{\mathrm{air}}\right) \cdot Nu \cdot \frac{\pi\,\lambda_{\mathrm{air}}}{Q\,c_{\mathrm{p}}} + \frac{\Delta H}{c_{\mathrm{p}}} \frac{\mathrm{d}X_{\mathrm{c}}}{\mathrm{d}x}\,, \tag{3.94}$$

$$\frac{\mathrm{d}F}{\mathrm{d}x} = Q\,\frac{\mathrm{d}v}{\mathrm{d}x} + c_{\mathrm{f}}\,\frac{\rho_{\mathrm{air}}}{2}\,v^2\,\pi\,D - \varrho_{\mathrm{p}}\,g\,A\,. \tag{3.95}$$

Remark: The surface tension contribution is neglected.

Rheology: Constitutive equations

Case 1: Newton model, purely viscous behaviour

$$\sigma = \eta\,\frac{\mathrm{d}v}{\mathrm{d}x}\,. \tag{3.96}$$

Case 2: Maxwell model, visco-elastic behaviour

$$\sigma + \lambda\,v\,\frac{\mathrm{d}\sigma}{\mathrm{d}x} = \eta\,\frac{\mathrm{d}v}{\mathrm{d}x}\,. \tag{3.97}$$

Case 3: upper convected Maxwell model, visco-elastic behaviour

$$\sigma_{\mathrm{xx}} + \lambda\,v\,\frac{\mathrm{d}\sigma_{\mathrm{xx}}}{\mathrm{d}x} = 2\,\lambda\,(G + \sigma_{\mathrm{xx}})\,\frac{\mathrm{d}v}{\mathrm{d}x}\,, \tag{3.98}$$

$$\sigma_{\mathrm{rr}} + \lambda\,v\,\frac{\mathrm{d}\sigma_{\mathrm{rr}}}{\mathrm{d}x} = -\lambda\,(G + \sigma_{\mathrm{rr}})\,\frac{\mathrm{d}v}{\mathrm{d}x}\,. \tag{3.99}$$

Case 4: Phan-Tien-Tanner model, visco-elastic behaviour with strain softening

$$\kappa \cdot \sigma_{\mathrm{xx}} + \lambda\left(v\,\frac{\mathrm{d}\sigma_{\mathrm{xx}}}{\mathrm{d}x} - 2\frac{\mathrm{d}v}{\mathrm{d}x}\,\sigma_{\mathrm{xx}}\right) = 2\,G\,\lambda\frac{\mathrm{d}v}{\mathrm{d}x}\,, \tag{3.100}$$

$$\kappa \cdot \sigma_{\mathrm{rr}} + \lambda\left(v\,\frac{\mathrm{d}\sigma_{\mathrm{rr}}}{\mathrm{d}x} + \frac{\mathrm{d}v}{\mathrm{d}x}\,\sigma_{\mathrm{rr}}\right) = -G\,\lambda\,\frac{\mathrm{d}v}{\mathrm{d}x}\,, \tag{3.101}$$

$$\kappa = \exp\left(\frac{\alpha}{G}\,(\sigma_{\mathrm{xx}} + 2\,\sigma_{\mathrm{rr}})\right)\,. \tag{3.102}$$

Stress for constitutive equations cases 1 and 2:

$$\sigma = \frac{F}{A}\,, \tag{3.103}$$

for constitutive equations cases 3 and 4:

$$\Delta\sigma = \sigma_{\mathrm{xx}} - \sigma_{\mathrm{rr}} = \frac{F}{A}\,. \tag{3.104}$$

Crystallisation

$$\frac{\mathrm{d}X_{\mathrm{c}}}{\mathrm{d}x} = \frac{K}{v}\,(1 - X_{\mathrm{c}})\,, \tag{3.105}$$

$$K = K_{\max}\,\exp\left(\frac{-4\,(\ln 2)(T - T_{\mathrm{c}})^2}{\Delta T_{1/2}^2} + C \cdot f_{\mathrm{am}}^2\right)\,. \tag{3.106}$$

Birefringence and orientation

$$\Delta n = \Delta n_{\mathrm{am}}(1 - X_{\mathrm{c}}) + \Delta n_{\mathrm{cr}}\, X_{\mathrm{c}} \,, \tag{3.107}$$

$$\Delta n_{\mathrm{am}} = C_{\mathrm{opt}} \cdot \sigma \,, \tag{3.108}$$

$$f_{\mathrm{am}} = \Delta n_{\mathrm{am}} / \Delta n^{0}_{\mathrm{am}} \,. \tag{3.109}$$

Polymer material properties

- mass density $\varrho_{\mathrm{p}} = \varrho_{\mathrm{p}}(T, X_{\mathrm{c}}, ...)$,
- specific heat $c_{\mathrm{p}} = c_{\mathrm{p}}(T, X_{\mathrm{c}}, ...)$,
- elongational viscosity $\eta_{\mathrm{e}} = \eta_{\mathrm{e}}(T, M, \dot{\varepsilon}, X_{\mathrm{c}}, ...)$,
- modulus $E = E(\varepsilon_{\mathrm{o}}, T, X_{\mathrm{c}}, ...)$,
- relaxation time $\lambda(T, \ldots)$,
- solidification temperature $T_{\mathrm{s}} = T_{\mathrm{s}}(\sigma, ...)$.

Transfer equations: heat and momentum

- heat transfer: NUSSELT number $Nu = Nu(Re_{\parallel}, Re_{\perp})$,
- air friction coefficient $c_{\mathrm{f}} = c_{\mathrm{f}}(Re_{\parallel}, Re_{\perp})$.

Environment material properties, e. g. for surrounding air

- density of air ϱ_{air} ,
- heat conductivity of air λ_{air} ,
- kinematic viscosity of air ν_{air} .

Structure development and textile fibre properties

- elongation to break ε_{b} ,
- tenacity TN ,
- orientation or birefringence Δn ,
- crystallinity X_{c} ,
- possible draw ratio (to get full drawn yarn, FDY) DR .

Initial and boundary conditions. To solve the coupled system of ordinary differential equations of fibre formation above, the related initial and/or boundary conditions are necessary. Known conditions at the spinneret are

- $T(0) = T_0$, the filament (spinning or extrusion) temperature, and
- $D(0) = D_0$, the filament diameter, resp. the filament velocity (= extrusion velocity) $v(0) = v_0$.

The initial rheological force $F(0) = F_0$ is unknown, therefore the boundary condition for the take-up point L has to be used:

- $v(L) = v_{\mathrm{L}}$, the take-up velocity.

In practice, a shooting method needs to be applied in order to solve the differential equations. The unknown initial rheological force F_0 is estimated first and then varied in an iterative procedure until the velocity v reaches the take-up velocity v_L after solidification within a given tolerance range. The other initial conditions (e. g. the initial crystallisation rate for computing the crystallisation) are usually set to zero at the starting point.

At higher take-up velocities stress-induced crystallisation may occur. The differential equations describing the crystallisation kinetics and the fibre formation procedure become stiffer and for solving them numerically a step width control is necessary. The maximum step width Δx_max can be fitted to a given maximum velocity step: $\Delta x_\mathrm{max} < \Delta v_\mathrm{max} \cdot \left(\frac{dv}{dx}\right)^{-1}$.

Examples of Calculation

The primary interest in simulating the melt spinning process is the possibility to get results on how the large number of process parameters influence the spinning behaviour and consequently the fibre properties. But the simulation results have to be verified by means of experiments in order to assess the quality of the model. These tests must be carried out in a twofold manner. At first, by measuring the physical variables within the fibre formation zone itself, for example by measuring the velocity v vs. distance x from the spinneret. Secondly, by determining the resulting fibre properties after spinning, for example the elongation to break, the birefringence, or the tenacity of the fibres. Many researchers have investigated several aspects to model the fibre formation process. However, their results differ more or less with respect to a satisfactory description of the material behaviour and correlation to the fibre properties. Sometimes the experimental verification seems rather difficult.

The following simulations were carried out exemplary for PA 6 (but would also be possible for other materials) and show some effects of changing the process variables to fibre formation. The computer simulation program and the equations used here for describing the material behaviour and the correlations to fibre properties (mainly for PA 6 and PET) were elaborated and tested over a long time during the scientific cooperation of the authors and their coworkers at the Institute of Polymer Research Dresden, together with several partners from the industry. The strong interaction between experimental and theoretical work is an unalterable requirement for developing and improving any model.

Figure 3.19 shows the fibre velocity v versus distance x from the spinneret exit for a typical melt spinning experiment of PA 6. The points in the figure are determined experimentally by means of laser doppler anemometry (LaserSpeed LSM50, TSI Inc.), the solid lines are calculated using computer simulation for two different rheological models discussed in Sect. 3.1.4. Numerous experiments with different spinning conditions have been conducted in order to improve and verify the model equations. Now the simulation can

be used for quick estimation of fibre formation, the simulation needs less than 1 second on a modern personal computer.

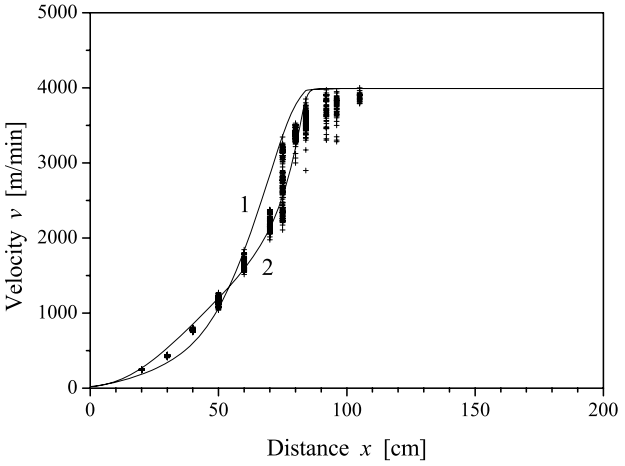

Fig. 3.19. Fibre velocity v vs. distance x from spinneret, *points:* velocity measured by means of laser doppler anemometry, each distance with 100...200 measurements, *solid lines:* calculated, 1 – MAXWELL model, 2 – PHAN-TIEN-TANNER model for rheological behaviour, *Spinning parameter:* PA 6, molecular weight: 17 000, throughput (per hole): 1.5 g/min, diameter of capillary: 0.25 mm, melt temperature: 250 °C, velocity of quenching air: 0.35 m/s, temperature of quenching air: 15 °C, take-up velocity: 4000 m/min; data source: Institute of Polymer Research Dresden

Figure 3.20 shows another comparison between experimentally determined and calculated fibre velocities, respectively. Each point in the diagram represents the mean value of 500...1000 measurements of velocity. The simulation results are in accordance with the experimental data, only for the high take-up speed of 5000 m/min the calculation seems to become a little inaccurate which shows a small gap of about 5 cm for the step (like a jump) to the final velocity. It becomes clear that melt spinning is a highly dynamic process, specifically the course of fibre formation at higher take-up velocities is very sensitive to little changes because of the occurrence of the stress induced crystallisation. *In principle* it seems that the accuracy of simulation which can be reached with current models is in the magnitude of about 10 percent of deviation.

The next simulations carried out for PA 6 and shown in the following diagrams are based on the MAXWELL model in order to describe the rheological behaviour. The molecular (number) weight (Mn) of the polymer is about 17 000. The molecular weight is related to the relative solution viscosity (in H_2SO_4, 96%, 20 °C) of about 2.45.

Figure 3.21 shows the effect of different take-up velocities on the *cooling behaviour* (up to 6000 m/min). It can be observed that there is only weak

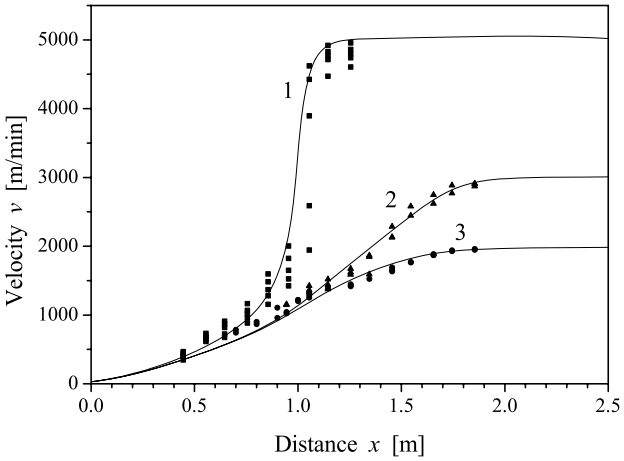

Fig. 3.20. Fibre velocity v vs. distance x from spinneret exit, *symbols:* velocity measured by means of laser doppler anemometry, each point represents the mean value of 500...1000 individual velocity measurements, *solid lines:* calculated with PHAN-TIEN-TANNER model for rheological behaviour, *Spinning parameter:* PA 6, molecular weight: 17 000, throughput (per hole): 2.0 g/min, diameter of capillary holes: 0.30 mm, melt temperature: 265 °C, no quenching air, temperature of environment: 25...28 °C, 1 – take-up velocity: 5000 m/min, 2 – 3000 m/min, 3 – 2000 m/min; data source: Institute of Polymer Research Dresden

coupling between velocity and cooling. On the other hand, the take-up velocity is the most important process parameter to affect the fibre properties. The higher the velocity, the higher the tensile stress and the higher the resulting orientation of the as-spun filaments. The higher the orientation, the lower the elongation to break. In reality, the spinning experiment with 1 g/min throughput and 6000 m/min take-up is not practicable because of the very high increase of spinning stress (see Fig. 3.22).

The two figures (Figs. 3.23 and 3.24) show the graphs of fibre formation for different mass throughputs Q. The mass throughput strongly influences the fibre cooling behaviour and therefore the filament temperature $T(x)$, and also the fineness of the as-spun filaments.

As shown in Fig. 3.24 the variation of the mass throughput Q has only a little effect on the stress at the solidification point. The higher throughput causes an increased length of the fibre formation zone and leads to an increase of the acting fibre force F (inertia and the air friction force increase with increasing mass throughput and distance). However, the larger diameter D, respectively the larger cross-sectional area A, compensate this effect with respect to the stress $\sigma = F/A$. Finally, the variation of troughput leads to nearly similar stress at the solidification point. There is only little changing of the fibre orientation and elongation to break with the variation of mass throughput.

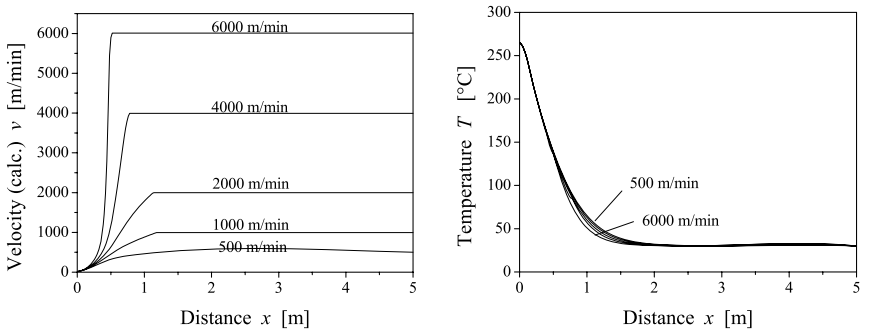

Fig. 3.21. (Calculated) fibre velocity v (*left*) and temperature T (*right*) vs. distance x from spinneret exit, MAXWELL model, *Spinning parameter:* PA 6, molecular weight: 17 000, mass throughput (per hole): 1.0 g/min, diameter of capillary hole: 0.30 mm, melt temperature: 265 °C, no quenching air, take-up velocity indicated: 500, 1000, 2000, 4000 and 6000 m/min

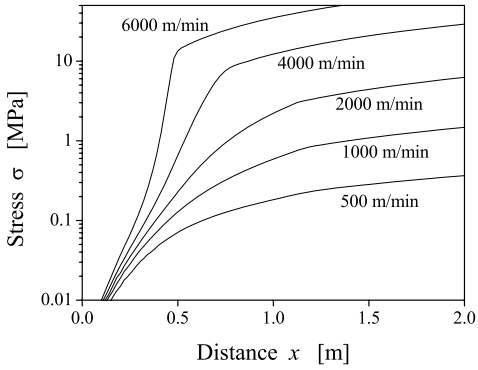

v_L	x_s	σ_s	ϵ_{spun}
m/min	m	MPa	%
500	1.20	0.23	416
1000	1.16	0.80	257
2000	1.12	2.99	138
4000	0.76	7.94	79
6000	0.50	13.41	54

Fig. 3.22. *Left:* (calculated) tensile stress $\sigma(x)$ vs. distance x from spinneret, MAXWELL model, *right:* stress σ_s at solidification point x_s and resulting elongation to break ϵ_{spun} of as-spun fibres, *Spinning parameter:* see Fig. 3.21

Combining the changes of both process variables, mass throughput Q and take-up velocity v_L, leads to the diagrams shown in Fig. 3.25. In this figure the graphs for the proportional increase of both $Q \propto v_L$ are depicted, this means *constant* as-spun fineness Tt.

Obviously, the stress at the solidification point increases if the mass throughput and take-up velocity increase in a proportional manner. The resulting fibre orientation also increases and the elongation to break for the as-spun fibres decreases.

Finally, the effect of the cooling conditions will be investigated. Figure 3.26 shows the influence of the environmental air temperature T_{air} and Fig. 3.27 depicts the effect of different velocity profiles v_{air} of quenching air on fibre temperature $T(x)$ and fibre velocity $v(x)$.

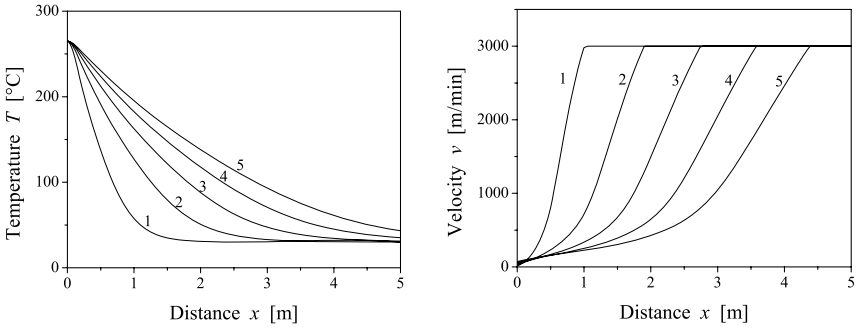

Fig. 3.23. (Calculated) fibre temperature T (*left*) and velocity v (*right*) vs. distance x from spinneret exit, MAXWELL model, *Spinning parameter:* PA 6, molecular weight: 17 000, mass throughput (per hole) indicated: 1...5 g/min (#1...#5), diameter of capillary hole: 0.30 mm, melt temperature: 265 °C, no quenching air, take-up velocity: 3000 m/min

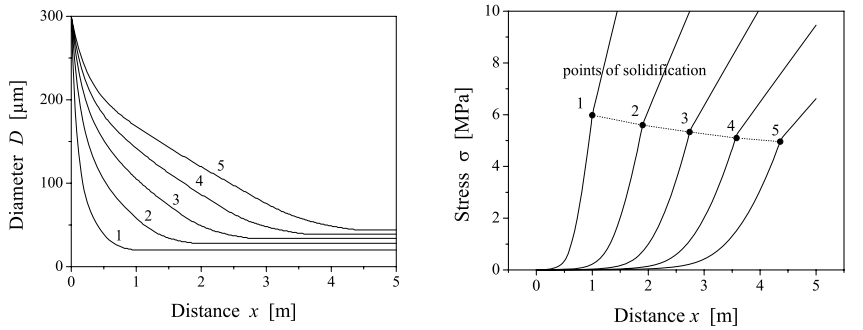

Fig. 3.24. (Calculated) fibre diameter D (*left*) and tensile stress σ (*right*) vs. distance x from spinneret exit, MAXWELL model, *Spinning parameter:* PA 6, molecular weight: 17 000, mass throughput (per hole) indicated: 1...5 g/min (#1...#5), diameter of capillary: 0.30 mm, melt temperature: 265 °C, no quenching air, take-up velocity: 3000 m/min

Table 3.10 summarises the effects of changing certain parameters with respect to fibre orientation, expressed by the elongation to break.

It is interesting to see the model predictions for the practical task of changing the spinning parameter under the conditions of constant fineness *and* constant elongation to break *after* drawing. The following is a typical question that occurs in fibre production: How to change mass throughput, take-up velocity and draw ratio to increase productivity (expressed by the mass throughput) under the condition of unchanging final fibre properties after drawing? An answer can be given with the help of the fibre formation model. The next figures show the main results for the task of spinning a full oriented PA 6 yarn (FDY) with final filament fineness of 4 dtex and final elongation to break of 25% after drawing.

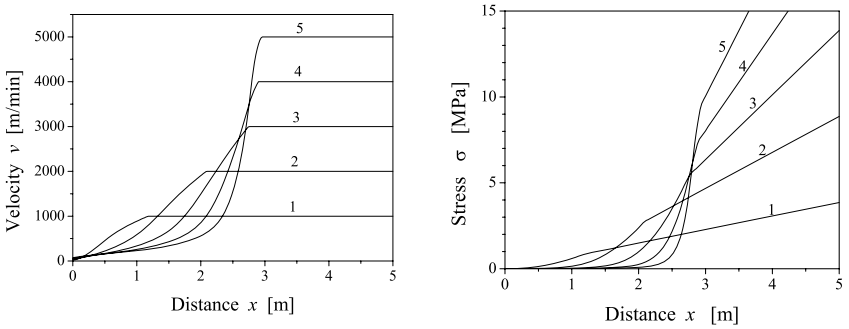

Fig. 3.25. (Calculated) fibre velocity v (*left*) and tensile stress σ (*right*) vs. distance x from spinneret exit, MAXWELL model, *Spinning parameter:* PA 6, molecular weight: 17 000, diameter of capillary holes: 0.30 mm, melt temperature: 265 °C, no quenching air, constant as-spun fineness of $Tt = 10$ dtex: 1 — 1 g/min, 1000 m/min, 2 – 2 g/min, 2000 m/min, 3 – 3 g/min, 3000 m/min, 4 – 4 g/min, 4000 m/min, 5 – 5 g/min, 5000 m/min

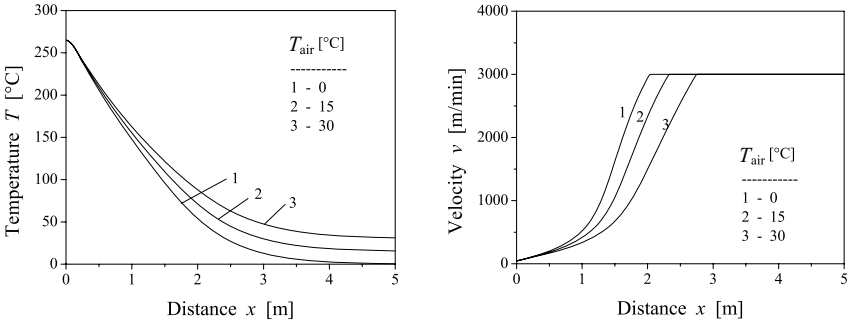

Fig. 3.26. (Calculated) fibre Temperature T (*left*) and velocity v (*right*) vs. distance x from spinneret exit, MAXWELL model, *Spinning parameter:* PA 6, molecular weight: 17 000, diameter of capillary hole: 0.30 mm, melt temperature: 265 °C, mass throughput: 3 g/min, take-up velocity: 3000 m/min, different temperatures of environmental air: 1 – 0 °C, 2 – 15 °C, 3 – 30 °C

Figure 3.28 depicts the simple relations between as-spun fineness Tt and needed draw ratio DR for different mass throughputs Q vs. take-up velocity v_L under the condition that the final filament fineness of (here) $Tt_\mathrm{f} = 4$ dtex should be reached after drawing:

$$Tt = \frac{Q}{v_\mathrm{L}} \quad , \qquad DR = \frac{Tt}{Tt_\mathrm{f}} = \frac{Q}{v_\mathrm{L} \cdot Tt_\mathrm{f}} \, .$$

Each point of these graphs represents the necessary draw ratio DR to reach the final filament fineness of 4 dtex for each combination (Q, v_L). But each combination of the spinning parameters (Q, v_L) is also connected with destinated orientation of the as-spun fibres and therefore the necessary draw ratio to reach the final fineness of 4 dtex leads to very different final elongations

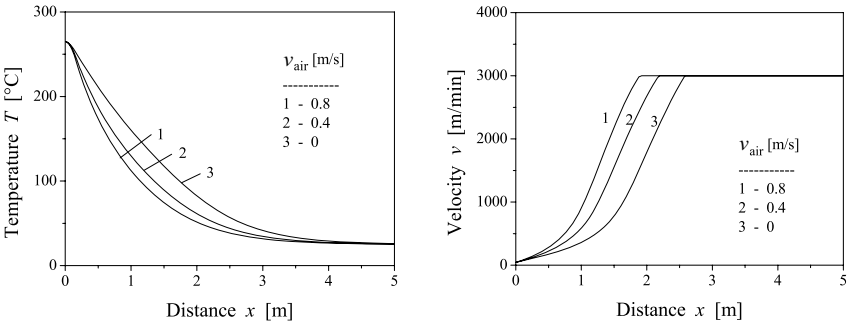

Fig. 3.27. (Calculated) fibre temperature T (*left*) and velocity v (*right*) vs. distance x from spinneret, MAXWELL model, *Spinning parameter:* see Fig. 3.26, different velocity profiles of quenching air: 1 – no quenching air, 2 – $v_{\text{air}} = 0.4$ m/s, 3 – $v_{\text{air}} = 0.8$ m/s, temperature of air: $T_{\text{air}} = 25\,℃$

to break. Only at certain combinations (in Fig. 3.28 they are marked by the symbol (•)) the elongation to break of 25% can be obtained.

Table 3.10. Variation of technological parameters: effects on orientation resp. elongation to break for as-spun filaments.

Changing	see Fig.	Example	ϵ_{b} in %
Take-up velocity v_{L}	3.21	500 m/min	416
($Q = 1$ g/min)		1000 m/min	257
		2000 m/min	138
		4000 m/min	79
Throughput (per hole) Q	3.24	1 g/min	95
($v_{\text{L}} = 3000$ m/min)		2 g/min	98
		3 g/min	101
		4 g/min	102
$Q \propto v_{\text{L}}$	3.25	1 g/min, 1000 m/min	257
($Tt = 10$ dtex)		2 g/min, 2000 m/min	146
		3 g/min, 3000 m/min	101
		4 g/min, 4000 m/min	84
Air temperature T_{air}	3.26	0 ℃	109
($v_{\text{air}} = 0$ m/s)		15 ℃	105
		30 ℃	101
Air velocity v_{air}	3.27	0.0 m/s	102
($T_{\text{air}} = 25\,℃$)		0.4 m/s	100
		0.8 m/s	97

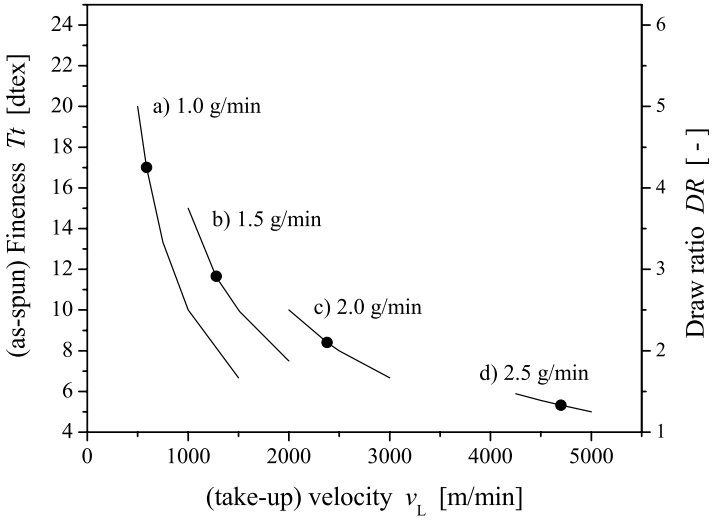

Fig. 3.28. Relation between (as-spun) fineness Tt and needed draw ratio DR vs. take-up velocity v_L to reach final filament fineness of $Tt_\mathrm{f} = 4$ dtex after drawing; different mass throughputs Q: a) 1.0 g/min, b) 1.5 g/min, c) 2.0 g/min, d) 2.5 g/min, the symbols (•) mark the combinations where additionally the (calculated) final elongation of 25% after drawing is reached, see also Fig. 3.29, *Spinning parameter:* PA 6, moleculare weight: 17 000, diameter of capillary hole: 0.30 mm, melt temperature: 265 °C, no quenching air

The calculated results for the dependency of elongation to break of the as-spun fibres on take-up velocity v_L for different mass throughputs Q are shown in the upper part of Fig. 3.29. In the lower part the resulting final elongations to break ϵ_b after drawing to the final filament fineness of 4 dtex are depicted. It can be seen that only for certain combinations (Q, v_L) it is possible to reach the required final properties of $Tt_\mathrm{f} = 4$ dtex fineness *and* $\epsilon_\mathrm{b} = 25\%$ elongation.

In Fig. 3.30 the results of the calculations are summarised and the answer to the question for how to increase productivity, posed at the beginning of this section, is given. The relation between mass throughput and take-up velocity is a nonlinear one: To increase the mass throughput, a super proportional increase of the take-up velocity is necessary if the final fibre properties all remain unchanged.

It is easy now to get the direction of how to adjust the general parameters throughput and take-up velocity for a given task in fibre spinning and also to appreciate the effects of changing spinning parameters on fibre properties.

Therefore the model of fibre formation can be a powerful tool not only in fibre research but also in the production process.

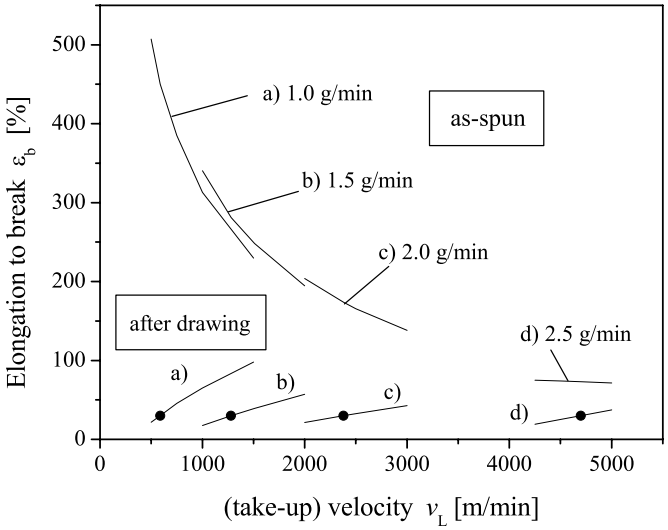

Fig. 3.29. (Calculated) elongation to break vs. take-up velocity v_L *before* drawing (as-spun) and *after* drawing to the final fineness of $Tt_f = 4$ dtex, different mass throughputs Q: a) 1.0 g/min, b) 1.5 g/min, c) 2.0 g/min, d) 2.5 g/min, the points (•) mark the required 25% elongation to break after drawing; *Spinning parameter:* see Fig. 3.28

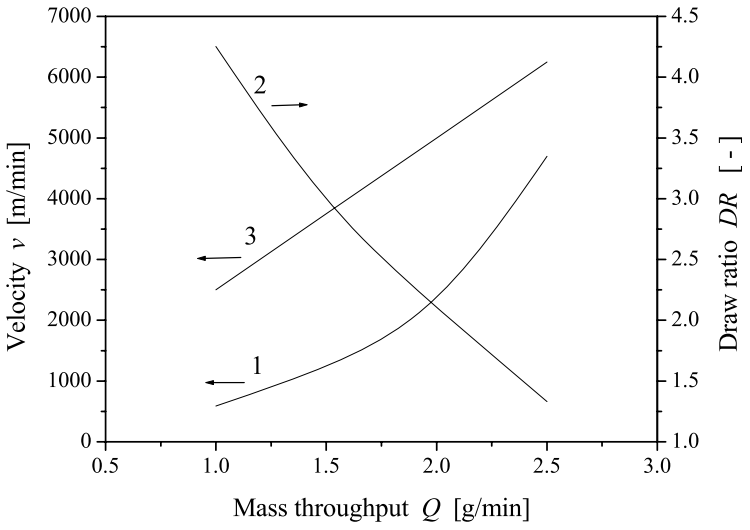

Fig. 3.30. Relationships between (1) take-up velocity v_L, (2) draw ratio DR and (3) wind-up velocity $v_w = DR \cdot v_L$ vs. mass throughput Q (per hole) for FDY spinning process with final filament fineness of $Tt_f = 4$ dtex and (calculated) elongation to break of $\epsilon_b = 25\%$ after drawing, *Spinning parameter:* see Fig. 3.28

3.2 Modelling of Fibre Formation in the Multifilament Melt Spinning Process

3.2.1 Peculiarities in Multifilament Spinning

In the prior discussion about modelling the stationary single filament process, the environment of the fibre was initially assumed to be the boundary condition with a given temperature $T_{\text{air}}(x)$, resp. velocity profile $v_{\text{air}}(x)$ of the surrounding air. It is important to recognise that in multifilament spinning these boundary conditions can vary from filament to filament location within the filament bundle because of the interaction between the filaments and air. At first, the hot filaments dissipate heat to the quenching air while it flows through the bundle. The air temperature increases. Secondly, the air flow is deflected in filament direction because the running filaments will impart the axial component and reduce the transversal component of air velocity. These effects are illustrated in Fig. 3.31. On the other hand, the cross flow of air will also disturb the axially sucked air flow in the boundary layer of the filaments. For a sufficient number of filaments per square unit the boundary layers for the individual filaments also may overlap. Near the converging point where the filaments are bundled the air flow inside the bundle will be pressed out. As a result, the friction forces for the individual filaments then vanish.

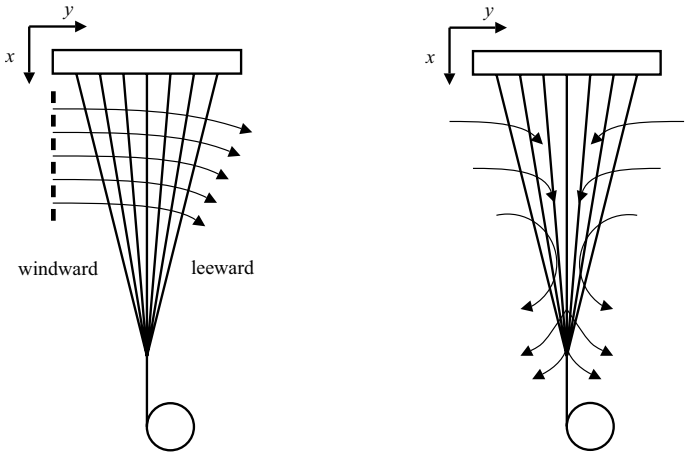

Fig. 3.31. Multifilament melt spinning process (schematic), *left:* active quenching from left hand side, *right:* no active quenching but air is sucked from the bundle itself

All these effects influence the heat and momentum transfer from each filament surface to the environment. Different geometries of the bundle and air flow are possible, too (Fig. 3.32). Therefore, the spinning conditions of

the individual filaments within the bundle vary and the spun filaments show differences in structure and properties as a function of their position. These differences lead to non-uniform or scattered properties, respectively, which may influence the further processing in a negative manner.

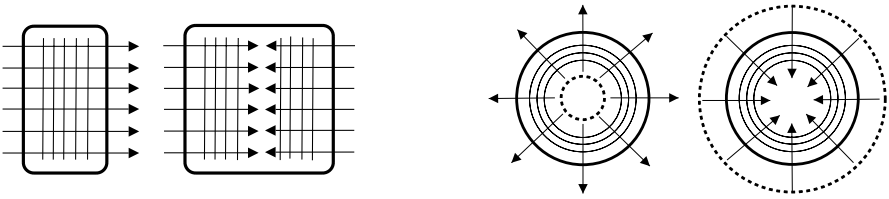

Fig. 3.32. Possible geometries of multifilament spinning. *Left:* one-sided and double-sided cross quenching; *right:* radial blowing from inside to outside and vice versa

Examples. The following two examples give a simple estimation in which a rise in temperature for the quenching cross air flow in a filament bundle can be expected:

1. POY - yarn, PA 6

polymer:	poly(amide) 6
spinneret:	24 holes arranged on two concentric circles,
	diameter of outer circle: $D_1 = 50\,\mathrm{mm}$,
	diameter of inner circle: $D_2 = 40\,\mathrm{mm}$,
	diameter of capillary holes: $D_0 = 0.25$ mm,
melt temperature:	$T_0 = 255\,^{\circ}\mathrm{C}$,
throughput:	$Q_{\mathrm{PA}} = 24 \times 1.5$ g/min $= 36$ g/min,
take-up velocity:	$v_{\mathrm{L}} = 3000$ m/min $\ldots$ 4000 m/min,
quenching:	cross quenching from one side,
	air temperature $T_{\mathrm{air}} = 20\,^{\circ}\mathrm{C}$,
	air velocity of air $v_{\mathrm{air}} = 0.35$ m/s,
	length of quenching zone $L_{\mathrm{air}} = 1.20$ m .

Assuming that the fibre formation zone ends at the end of the quenching zone (no further deformation occurs) the transported heat $Q_{\mathrm{air}} \cdot c_{\mathrm{air}}$ and the temperature rise ΔT_{air} of air can be estimated as follows

$$Q_{\mathrm{air}} \cdot c_{\mathrm{air}} \cdot \Delta T_{\mathrm{air}} = Q_{\mathrm{PA}} \cdot c_{\mathrm{PA}} \cdot \Delta T_{\mathrm{PA}} \ , \tag{3.110}$$

where c_{air} is the specific heat capacity of air, and the air volume affecting the fibre bundle is approximately given by $Q_{\mathrm{air}} \approx \varrho_{\mathrm{air}} \cdot v_{\mathrm{air}} \cdot L_{\mathrm{air}} \cdot D_1$, while using the diameter D_1 of the outer circle as effective width of quenching air. Using the following parameters

temperature change of polymer:	$\Delta T_{\mathrm{PA}} = 200$ K,
specific heat capacity of PA 6:	$c_{\mathrm{PA}} = 2.4$ kJ/(kg · K),
specific heat capacity of air:	$c_{\mathrm{air}} = 1.0$ kJ/(kg · K),
mass density of air:	$\varrho_{\mathrm{air}} = 1.2$ kg/m^3,

leads to the temperature rise of quenching air of $\Delta T_{\mathrm{air},1} \approx 10$ K. The higher temperature at the exit side of air causes a delayed cooling of the filaments and thus increases the length of the fibre formation zone. The distance from the spinneret exit to the solidification point for the filaments at the leeward side is larger as at windward side. Figure 3.33 shows the effect of the different curves of fibre velocity vs. distance for filaments at the windward and leeward side.

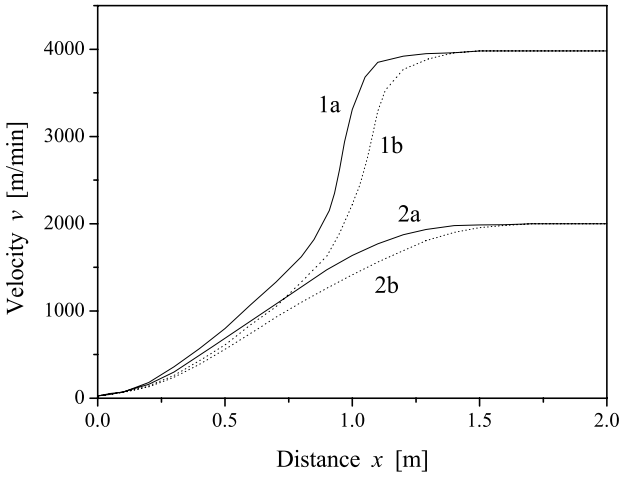

Fig. 3.33. Filament velocity v (measured by means of laser doppler anemometry) vs. distance x from spinneret exit, differences between windward (a) and leeward (b) sides; quenching air velocity: 0.35 m/s, PA 6 melt spinning, throughput: 1.5 g/min, take-up velocity: 1 – 4000 m/min, 2 – 2000 m/min; data source: Institute of Polymer Research Dresden

2. Staple fibre process, PET
The example concerns staple fibre spinning with the following parameters:

polymer:	poly(ethylene terephthalate), PET
spinneret:	1300 holes, 13 rows with 100 holes in each row, dimension W x B: 26 cm x 6.5 cm, rectangular, diameter of capillary holes: 0.30 mm,
melt temperature:	$T_0 = 290$°C,
throughput:	$Q_{\mathrm{PET}} = 1300 \times 0.6$ g/min $= 780$ g/min,

take-up velocity: $v_L = 1200$ m/min,
quenching: cross quenching from one side,
air temperature $T_{\text{air}} = 20\,^{\circ}\text{C}$,
air velocity $v_{\text{air}} = 1.5$ m/s,
length of quenching zone $L_{\text{air}} = 0.5$ m .

The fibre formation should be finished after a distance of 0.5 m. In analogy to the first example and using the parameters applicable to PET

temperature change of polymer: $\Delta T_{\text{PET}} = 220$ K,
specific heat capacity PET: $c_{\text{PET}} = 1.5$ kJ/(kg · K),
effective width of quenching air: $W = 26$ cm,

then follows the mean temperature rise of quenching air at the exit side of approximately $\Delta T_{\text{air},2} \approx 20$ K

The estimated temperature change of air can be confirmed for the PA 6–POY process experimentally. But, in the case of the second example of the PET–staple fibre process, the experimental observations differ strongly from the estimation: The temperature rise of quenching air at the leeward side varies with distance from the spinneret and reaches *more than* 100 K near the spinneret (see Fig. 3.44 following on page 115). Based on the rather simple heat balance, the approximation carried out is no longer valid because the local effects of air deflection and heat transfer are neglected. A more detailed analysis becomes mandatory.

3.2.2 Models of Interaction Between the Fibre Bundle and the Environment

The temperature and velocity field of air within the fibre bundle and the fibre strands interact and thus influence each other [247, 248]. Therefore, the multifilament process should be treated as a two-phase system [249] where the filaments are embedded in an environmental 'matrix'. At the boundary layers between the two phases the general conditions for heat and momentum transfer have to be satisfied. This method was employed specifically for the wet spinning process by Szaniawski and Zachara [250–254]. But, in case of a common melt spinning process where the 'matrix' is given by air, the properties and the behaviour of the two phases are extremely different. This is why it is possible to regard both phases in a separate manner, and finally to combine a model of multifilament melt spinning from three parts

- the single fibre formation model,
- the model of air velocity and air temperature fields,
- and the model of interaction between both.

Due to the heat and momentum exchange between fibres and air an iterative calculation procedure is necessary. The iteration can be carried out in the following manner (Fig. 3.34):

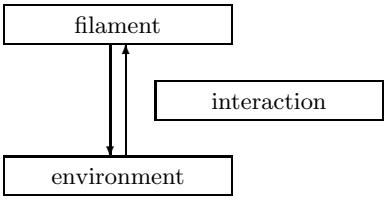

Fig. 3.34. Schematic model for multifilament spinning

1. Calculation of velocity and temperature fields of air on the basis of simple assumptions about fibre formation.
2. Calculation of the fibre formation process for some (not all) single fibres in various positions across the bundle on the basis of the calculated velocity and temperature fields of air.
3. Like step 1, calculation of velocity and temperature fields of air, but now on the basis of the new calculated fibre formation results.

Steps 2 and 3 need to be repeated until sufficient convergence is reached, i. e. no further changes occur. Finally, the calculation of fibre formation for *all fibre positions* should be conducted with the final temperature and velocity fields of air.

Cells method. Matsuo et al. [255], Yasuda et al. [65, 66] and Ishihara et al. [256, 257] developed a method to treat the multifilament effects. They divided the fibre bundle into individual cells for each filament row to apply the balance equations of energy and momentum (Fig. 3.35). This method was also used by Dutta [258, 259] and later similar treatments were developed by means of *FEM* (finite elements method) calculations.

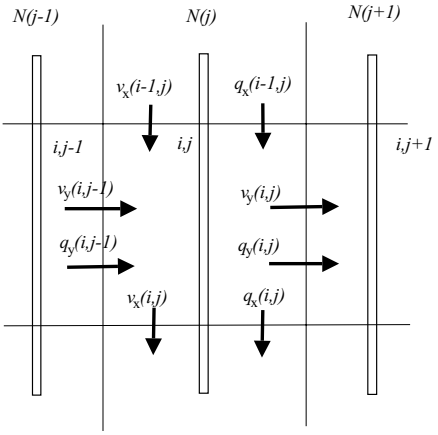

Fig. 3.35. Multifilament bundle divided into individual cells

In Fig. 3.35, $N(j)$ is the spinline of row number j, $v_{\mathrm{x}}(i,j)$ and $v_{\mathrm{y}}(i,j)$ are the components of air velocity in the cell (i,j), and $q_{\mathrm{x}}, q_{\mathrm{y}}$ are the components of heat flow in x and y direction, respectively. The dimensions of each cell are given by $\Delta x \cdot \Delta y \cdot \Delta z$ (dimensions in fibre direction, in blowing air direction, and perpendicular to both). The balance of air flow is composed by four flow elements

$$\big(v_{\mathrm{y}}(i,j-1) - v_{\mathrm{y}}(i,j)\big)\Delta z\,\Delta x + \big(v_{\mathrm{x}}(i-1,j) - v_{\mathrm{x}}(i,j)\big)\Delta y\,\Delta z = 0 \quad (3.111)$$

and the heat flow balance is given by five elements

$$q_{\mathrm{y}}(i,j-1) - q_{\mathrm{y}}(i,j) + q_{\mathrm{x}}(i-1,j) - q_{\mathrm{x}}(i,j) = \big(T(i,j) - T_{\mathrm{air}}\big)\; Nu\,\pi\,\lambda_{\mathrm{air}}\;. \quad (3.112)$$

The components of heat flow are defined as

$$q_{\mathrm{y}}(i,j) = \varrho_{\mathrm{air}}\, c_{\mathrm{air}}\, v_{\mathrm{y}}(i,j)\, T_{\mathrm{air}}(i,j)\,\Delta z\,\Delta x \quad (3.113)$$

$$q_{\mathrm{x}}(i,j) = \varrho_{\mathrm{air}}\, c_{\mathrm{air}}\, v_{\mathrm{x}}(i,j)\, T_{\mathrm{air}}(i,j)\,\Delta z\,\Delta y\,, \quad (3.114)$$

where $T(i,j)$ and $T_{\mathrm{air}}(i,j)$ denote the filament and air temperature in cell number (i,j), respectively, ϱ_{air} and c_{air} are the density and heat capacity of air. The main problem connected with this method is the determination of the exact amount of *air pumping rate* of fibre – this is the difference of the entrained air flows $v_{\mathrm{x}}(i,j) - v_{\mathrm{x}}(i-1,j)$. Some researchers used the estimation of Sakiadis [208–210] based on the boundary layer theory for continuous cylindrical surfaces. But the cross air flow disturbs the cylindrical symmetry of the boundary layer and a detailed analysis may show that the assumptions made by Sakiadis are no longer valid in this case. There is no sufficient theory for the flow behavior around a fibre in motion with additional cross air flow. Nevertheless, some calculations using *FEM*-methods more recently have been reported.

3.2.3 Continuum Theory

In order to avoid the difficulties related to the pumping effect of filaments (which are quenched by an additional cross air flow) another model can be used [260, 261]. The basic idea of this model was originally developed by Schöne. The following section describes the method of calculating the velocity and temperature fields of air for symmetric fibre bundles based on the continuum theory of hydrodynamics. The application of this model to the multifilament staple fibre spinning will be demonstrated later.
The main ideas of the continuum method are:

- Momentum balance: the equivalence of both air friction force acting on fibres and acceleration impart of axial velocity component of air.
- Heat balance: the equivalence of both cooling of fibres and heating of quenching air.

- Continuously smoothed sources: the fibres are the sources of momentum and heat imposed to the quenching air. These sources are assumed as continuously distributed density fields in the bundle region.
- Rectangular or axially symmetric geometry is assumed in order to simplify the mathematical treatment and to allow for the use of analytical expressions for the quenching air flow.

Air Velocity

Rectangular geometry. The expressions for components v_x and v_y of the air velocity field $\boldsymbol{v}_\mathrm{air}$ are given by the NAVIER-STOKES equations and the continuity equation. In cartesian coordinates they are written as follows

$$\varrho_\mathrm{air}(v_\mathrm{x}v_{\mathrm{x,x}} + v_\mathrm{y}v_{\mathrm{x,y}}) = \eta_\mathrm{air}(v_{\mathrm{x,xx}} + v_{\mathrm{x,yy}}) + f_\mathrm{x} - p_{,\mathrm{x}} \,, \tag{3.115}$$

$$\varrho_\mathrm{air}(v_\mathrm{x}v_{\mathrm{y,x}} + v_\mathrm{y}v_{\mathrm{y,y}}) = \eta_\mathrm{air}(v_{\mathrm{y,xx}} + v_{\mathrm{x,yy}}) + f_\mathrm{y} - p_{,\mathrm{y}} \,, \tag{3.116}$$

$$v_{\mathrm{x,x}} + v_{\mathrm{y,y}} = 0 \,. \tag{3.117}$$

The partial derivatives with respect to the coordinates are symbolised by the subscripts $()_{,\mathrm{x}} \equiv \partial()/\partial x$ and $()_{,\mathrm{y}} \equiv \partial()/\partial y$, v_x and v_y are the components of air velocity in fibre direction x and in cross flow direction y, see Fig. 3.36, left side. The terms ϱ_air and η_air represent the density and (dynamic) viscosity of air, p is the pressure, and f_x and f_y are the components of the external force density (see later). The continuity equation (3.117) can be satisfied by introducing the potential flow function $\Psi(x, y)$ with

$$v_\mathrm{x} = \Psi_{,\mathrm{y}} \,, \qquad v_\mathrm{y} = -\Psi_{,\mathrm{x}} \,. \tag{3.118}$$

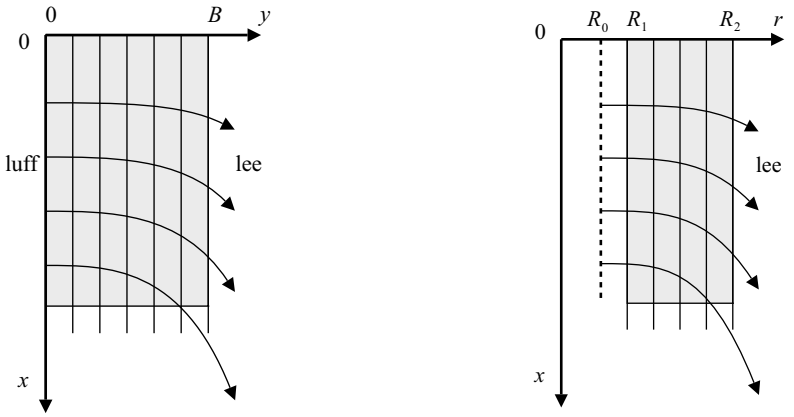

Fig. 3.36. Geometry of multifilament spinning. *Left:* rectangular (cartesian) coordinates, blowing air from the left side, *right:* radial symmetry, blowing air from inner candle (with radius R_0) outside

Discussion I. Some simplifications, which are not so far from real spinning conditions, should be discussed as follows. These assumptions will allow us to use an analytical description of the air flow inside the fibre bundle.

1) At first, we should assume a constant air blowing profile $v_{\mathrm{y}}(x,0) = v_{\mathrm{y0}}$, independent of distance x at the windward-side. The interesting region for fibre formation is the one between the spinneret exit at $x = 0$ and the solidification point x_{s}. In this region the course of fibre velocity v with respect to distance x increases from the (very) low extrusion velocity v_0 to the final take-up velocity v_{L} in an S-shaped manner. This development of the fibre velocity $v(x)$ should be simply approximated as a linearly with distance x increasing function: $v(x) = x \cdot v_{\mathrm{L}}/x_{\mathrm{s}}$. Furthermore, the relation between the air friction force and the difference of fibre velocity and air velocity $(v - v_{\mathrm{x}})$ should be assumed as a nearly linearly increasing function $F_{\mathrm{air}} \propto x \cdot (v - v_{\mathrm{x}})$. It is also convenient to approximate the air velocity v_{x} itself as a function linearly increasing with x. On the other hand, if there are free boundary conditions on the leeward-side, the pressure p also becomes independent of distance x and can be neglected in Eq. 3.115 (This argumentation is only valid in case of the free leeward side, see Fig. 3.32). The advantage of the linearisation is the possibility to uncouple the partial differential equations (3.115) and (3.116), in order to get ordinary differential equations with respect to x and y coordinates. The errors which are made by these linearisations with respect to the real course of fibre formation can be corrected later by means of an iteration procedure in a second step. Using the product

$$\Psi(x,y) = x \cdot g(y) \tag{3.119}$$

now leads to the simplified relations

$$\varrho_{\mathrm{air}}\, x \left(g'^2 - g\, g''\right) = \eta_{\mathrm{air}}\, x\, g''' + f_{\mathrm{x}} \;, \tag{3.120}$$

$$\varrho_{\mathrm{air}}\, g\, g' = -\eta_{\mathrm{air}}\, g'' - p' + f_{\mathrm{y}} \;, \tag{3.121}$$

for the reduced potential flow function g, where g is only a function of the cross direction y. The prime $(')$ denotes the derivative with respect to y, $g' \equiv \mathrm{d}g/\mathrm{d}y$.

2) Secondly, we should concentrate on Eq. 3.120. At the moment we are only interested in the velocity field of air and its deflection and acceleration within the filament bundle in the fibre direction. This is why we do not consider the bending of filaments caused by the air stream in cross direction and its backward deceleration effect on the air. Together with the linear increasing force density (that is air friction force per unit volume) in the form

$$f_{\mathrm{x}}(x,y) = x \cdot \varrho_{\mathrm{air}}\, k(y) \tag{3.122}$$

we get for Eq. 3.120 the relation

$$g'^2 - g\, g'' = \nu_{\mathrm{air}}\, g''' + k \;, \tag{3.123}$$

where $\nu_{\mathrm{air}} = \eta_{\mathrm{air}}/\varrho_{\mathrm{air}} \approx 1.5 \cdot 10^{-5}$ s/m^2 is the kinematic air viscosity. Outside the bundle (region I in Fig. 3.36) the force density term k vanishes and there is a simple analytical solution which satisfies the relation (3.123): $g(y) = c_1 \exp(c_2\, y) + c_3\, \nu_{\mathrm{air}}$, with constants c_{i}. Inside the bundle (region II) the differential equation can be solved numerically. But because of the low air viscosity, the viscous term $\nu_{\mathrm{air}}\, g'''$ becomes insignificant in comparison to the other parts and can thus be neglected. The numerical solutions with and without the viscous part show that it is indeed possible to neglect the viscous part within the bundle, and we then get the most simplified differential equation

$$g'^2 - g\, g'' = k\ , \tag{3.124}$$

which allows us to calculate the air velocity field inside the filament bundle.

Because we are only interested in the air velocity inside the bundle (region II) the coordinate y can now be shifted in such a manner that the left edge of the bundle fits into the origin at $y = 0$, and the right edge of the bundle (its width) is given by $y = B$.

Analytical expressions for the air velocity field. An analytical solution for $g(y)$ in (3.124), resp. for the potential flow function $\Psi(x, y) = x \cdot g(y)$ (3.119) and for the components v_{x} and v_{y} of the air velocity field inside the filament bundle, exists for the special case that the variation of the force density term k (3.122) *across* the fibre bundle in y-direction can be expressed in the manner

$$k(y) = \kappa^2 \exp(2\,\alpha\, y)\ . \tag{3.125}$$

Equation 3.125 includes different possible courses of the force density across the fibre bundle: $\alpha = 0$ describes the constant force density, $\alpha > 0$ the increasing force density, and $\alpha < 0$ is related to a decreasing force density with respect to y.

The analytical solution for the potential flow field in the simplified manner (3.124) is given by an exponential function with complex argument. To achieve physically realistic behaviour, a careful distinction between various cases is required. With the abbreviation

$$\beta = \frac{\alpha \cdot v_{\mathrm{y0}}}{\kappa} \tag{3.126}$$

the results for different cases can be expressed as follows:

Case 1: $1 - \beta^2 > 0$
The solutions for the potential flow function and the velocity components of air in this case are

$$\Psi(x, y) = -x \cdot \frac{v_{\mathrm{y0}}}{\sqrt{1-\beta^2}} \exp(\alpha\, y) \cos\Big(\frac{\kappa\sqrt{1-\beta^2}}{v_{\mathrm{y0}}}\, y + c\Big)\ , \tag{3.127}$$

$$v_{\mathrm{x}}(x,y) = x \cdot \kappa \cdot \exp(\alpha\, y)\left[\sin\Big(\frac{\kappa\,\sqrt{1-\beta^2}}{v_{\mathrm{y0}}}\, y + c\Big) - \frac{\beta}{\sqrt{1-\beta^2}}\cos\Big(\frac{\kappa\,\sqrt{1-\beta^2}}{v_{\mathrm{y0}}}\, y + c\Big)\right], \quad (3.128)$$

$$v_{\mathrm{y}}(x,y) = \frac{v_{\mathrm{y0}}}{\sqrt{1-\beta^2}} \cdot \exp(\alpha\, y)\cos\Big(\frac{\kappa\,\sqrt{1-\beta^2}}{v_{\mathrm{y0}}}\, y + c\Big), \quad (3.129)$$

with

$$c = \arctan\Big(\frac{\beta}{\sqrt{1-\beta^2}}\Big). \quad (3.130)$$

Case 2: $1-\beta^2 = 0$
The solutions for this (very special) case can be obtained by expanding the functions above to

$$\Psi(x,y) = -x \cdot v_{\mathrm{y0}} \cdot (1-\alpha\, y)\exp(\alpha\, y), \quad (3.131)$$

$$v_{\mathrm{x}}(x,y) = v_{\mathrm{y0}} \cdot \alpha \cdot x \cdot y \cdot \exp(\alpha\, y), \quad (3.132)$$

$$v_{\mathrm{y}}(x,y) = v_{\mathrm{y0}} \cdot (1-\alpha\, y)\exp(\alpha\, y). \quad (3.133)$$

Case 3: $1-\beta^2 < 0$
For this case the square root $\sqrt{1-\beta^2} = \mathrm{i}\sqrt{\beta^2-1}$ becomes imaginary. But using the identities $\cos(\mathrm{i}\,x) = \cosh(x)$, $\sin(\mathrm{i}\,x) = \mathrm{i}\,\sinh(x)$ and $\arctan(\mathrm{i}\,x) = \mathrm{i}\,\mathrm{artanh}(x)$, the solutions can be given again by means of real expressions

$$\Psi(x,y) = -x\,\frac{\alpha}{|\alpha|}\,\frac{v_{\mathrm{y0}}}{\sqrt{\beta^2-1}}\exp(\alpha\, y)\sinh\Big(d - \frac{\kappa\,\sqrt{\beta^2-1}}{v_{\mathrm{y0}}}\, y\Big), \quad (3.134)$$

$$v_{\mathrm{x}}(x,y) = x \cdot \kappa \cdot \frac{\alpha}{|\alpha|}\exp(\alpha\, y)\left[\cosh\Big(d - \frac{\kappa\,\sqrt{\beta^2-1}}{v_{\mathrm{y0}}}\, y\Big) - \frac{\beta}{\sqrt{\beta^2-1}}\sinh\Big(d - \frac{\kappa\,\sqrt{\beta^2-1}}{v_{\mathrm{y0}}}\Big)\right], \quad (3.135)$$

$$v_{\mathrm{y}}(x,y) = \frac{\alpha}{|\alpha|}\,\frac{v_{\mathrm{y0}}}{\sqrt{\beta^2-1}}\exp(\alpha\, y)\,\sinh\Big(d - \frac{\kappa\,\sqrt{\beta^2-1}}{v_{\mathrm{y0}}}\, y\Big), \quad (3.136)$$

with

$$d = \mathrm{artanh}\Big(\frac{\sqrt{\beta^2-1}}{\beta}\Big). \quad (3.137)$$

Figure 3.37 depicts the graphs of the velocity component v_{y} across the bundle in non-dimensional manner (reduced by v_{y0}) for the different cases above.

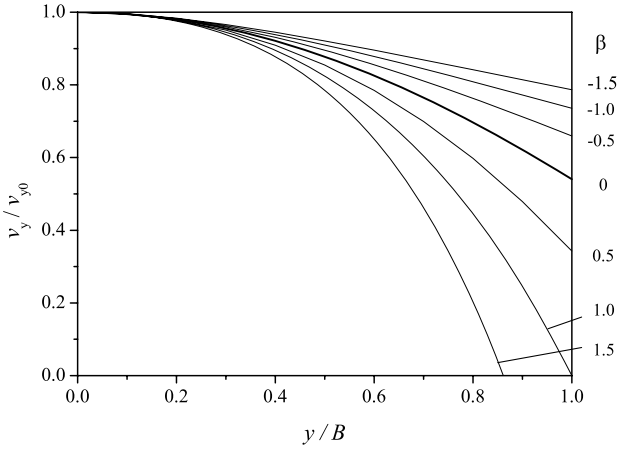

Fig. 3.37. Graphs of (reduced) velocity component $v_\mathrm{y}/v_{\mathrm{y}0}$ inside the bundle for different cases β, $\kappa\, B/v_{\mathrm{y}0} = 1$, values of β are indicated

Discussion II. Now we will discuss the important case of constant force density $k \neq k(y)$ across the bundle ($\alpha = \beta = 0$, case 1). The expressions for the velocity components v_x and v_y (see Eqs. 3.128 and 3.129) then are reduced to

$$v_\mathrm{x}(x,y) = x\,\kappa \sin\!\left(\frac{\kappa\, y}{v_{\mathrm{y}0}}\right) , \tag{3.138}$$

$$v_\mathrm{y}(x,y) = v_{\mathrm{y}0} \cos\!\left(\frac{\kappa\, y}{v_{\mathrm{y}0}}\right) . \tag{3.139}$$

Comparing the analytical expressions above with the numerical solution of Eq. 3.123 (with consideration of the air viscosity) shows that the approximated analytical solution and the numerical one are in accordance with each other. The air flow velocity inside the bundle is determined mainly by inertness and force density, therefore the viscous term can be neglected without changing the overall flow behaviour.

If there is no active quenching the filament bundle will suck the needed air by itself. This leads to a symmetrical air profile where air enters into the bundle from both sides. The minimum value of air velocity $v_{\mathrm{y}0,\mathrm{min}}$ which enters into the bundle can be determined with Eq. 3.138 and the condition

$$v_\mathrm{x}(x,0) = v_\mathrm{x}(x,B) = 0 , \tag{3.140}$$

or in equivalence with Eq. 3.139 and the condition for symmetry

$$v_\mathrm{y}(x,0) = -v_\mathrm{y}(x,B) = v_{\mathrm{y}0,\mathrm{min}} . \tag{3.141}$$

The minimum value of air velocity which results from self-priming and which describes the symmetric flow within the bundle is given by

$$v_{\mathrm{y0,min}} = \frac{\kappa\, B}{\pi}\ . \tag{3.142}$$

The value of quenching air which is necessary to penetrate the bundle $v_{\mathrm{y0,pen}}$ can be determined by the condition

$$v_{\mathrm{y}}(x, B) > 0 \tag{3.143}$$

and leads to the relation

$$v_{\mathrm{y0,pen}} > \frac{2\,\kappa\, B}{\pi} = 2 \cdot v_{\mathrm{y0,min}}\ . \tag{3.144}$$

Figure 3.38 qualitatively shows the air flow for the different cases.

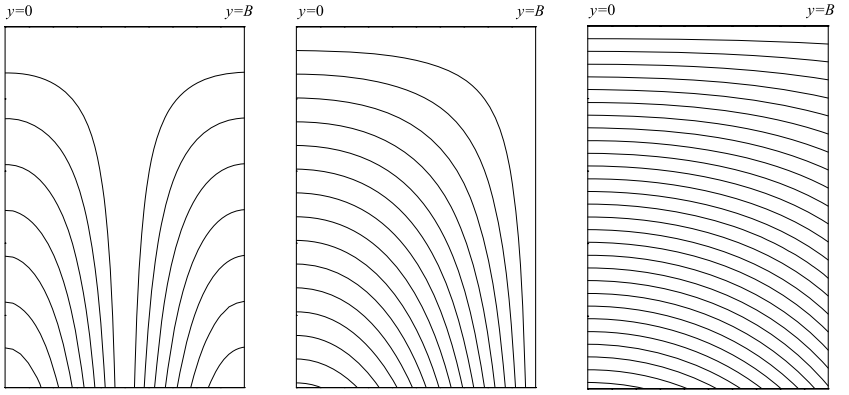

Fig. 3.38. Air flow within the filament bundle. *Left:* symmetric case, no active quenching, the filament bundle is self-priming air, $v_{\mathrm{y0}} = v_{\mathrm{y0,min}}$; *center:* limiting case of small quenching from left side, no penetration, $v_{\mathrm{y0}} = 2\, v_{\mathrm{y0,min}}$; *right:* active quenching from left side, air penetrates the bundle, $v_{\mathrm{y0}} = 4\, v_{\mathrm{y0,min}}$

The assumption of constant force density ($\alpha = \beta = 0$, case 1) across the bundle is applicable for many purposes. An example of this is the staple fibre spinning process with uniform distribution of capillary holes in the spinneret. It will later be investigated in more detail in Sect. 3.2.4. On the other hand, it is also possible to study the effect of air deflection by means of increasing or decreasing the number of capillary holes in the spinneret at each line by assuming a non-constant force density ($\alpha \neq 0$, $k \propto \exp(2\,\alpha\, y)$). The distribution variation of the spinneret capillary holes changes the force density $k(y)$ across the bundle and influences the flow behaviour inside. Figure 3.39 shows the effect of increasing (left graphs) and decreasing (right graphs) force density in comparison to the case of constant force density with respect to distance y.

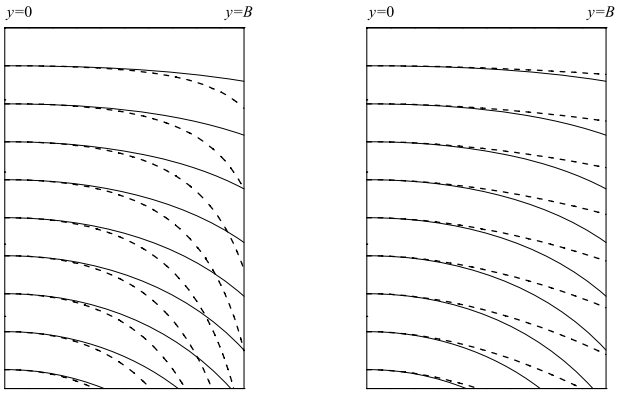

Fig. 3.39. Air flow within the filament bundle. *Left:* Comparison between constant force density (——, $\alpha = 0$) and increasing force density (– – –, $\alpha > 0$); *right:* Comparison between constant force density (——, $\alpha = 0$) and decreasing force density (– – –, $\alpha < 0$)

The minimum necessary air velocity for the self-priming filament bundle is given by Eq. 3.140. In the cases of variable force density $\alpha \neq 0$, it leads to the expression

$$v_{\mathrm{y0,min}} = \frac{\kappa\, B}{\pi} \sqrt{1 + \frac{\alpha}{|\alpha|} \Big(\frac{\alpha\, B}{2\,\pi} \Big)^2} \; . \tag{3.145}$$

Contrary to the symmetric flow in the case of constant force density (Fig. 3.38, left hand side) the streamlines now become asymmetric.

Iterative improvement of the analytical solution. The Eqs. (3.128) to (3.139) allow fast calculation of the air velocity inside the fibre bundle. However, they are based on the assumptions of constant air blowing velocity v_{y0} and linearly increasing filament velocity $v(x)$. Normally, in real spinning processes both the blowing air velocity and the filament velocity do notexactly follow these conditions. But the effects of the afore mentioned assumptions are mostly insignificant and therefore it is possible to use the developed relations in a modified manner. The external force density $f_{\mathrm{x}}(x, y) = x\, \varrho_{\mathrm{air}}\, k(y)$ and the velocity of blowing air v_{y0} are replaced by their *globally* varying *mean* values (with respect to distance x)

$$k(y) \rightarrow k_{\mathrm{m}}(x, y) = \frac{1}{x} \int_0^x k(x', y)\, dx' \; , \tag{3.146}$$

$$v_{\mathrm{y0}} \rightarrow v_{\mathrm{ym}}(x) = \frac{1}{x} \int_0^x v_{\mathrm{y0}}(x')\, dx' \; . \tag{3.147}$$

The dependence of the flow function on distance x can now be expressed indirectly through its dependence of k_{m} (or κ_{m}) and v_{ym}, respectively, on

distance x. Then, for the case $\alpha = 0$, the Eqs. 3.138 and 3.139 become

$$v_{\mathrm{x}}(x,y) = x\,\sqrt{k_{\mathrm{m}}(x)}\,\sin\Big(\frac{\sqrt{k_{\mathrm{m}}(x)}}{v_{\mathrm{ym}}(x)}\,y\Big)\;, \tag{3.148}$$

$$v_{\mathrm{y}}(x,y) = v_{\mathrm{ym}}(x)\,\cos\Big(\frac{\sqrt{k_{\mathrm{m}}(x)}}{v_{\mathrm{ym}}(x)}\,y\Big)\;. \tag{3.149}$$

The mean value of the force density $k_{\mathrm{m}}(x,y)$ needs to be calculated by means of iteration of the global momentum balance of air flow inside the fibre bundle with respect to distance x:

$$\begin{aligned}\sum_{j=1}^{N_{\mathrm{r}}} N(j) \int_0^x c_{\mathrm{f}}(x',y_{\mathrm{j}})\frac{\varrho_{\mathrm{air}}}{2}\big(v(x',y_{\mathrm{j}}) - v_{\mathrm{x}}(x',y_{\mathrm{j}})\big)^2\,\pi\,D(x',y_{\mathrm{j}})^2\,dx' \\ = W\int_0^B \varrho_{\mathrm{air}}\,v_{\mathrm{x}}^2(x,y)\,dy + W\int_0^x \varrho_{\mathrm{air}}\,v_{\mathrm{x}}(x',B)\,v_{\mathrm{y}}(x',B)\,dx'\;.\end{aligned} \tag{3.150}$$

Here, N_{r} is the number of filament rows, $N(j)$ is the number of filaments in each row j, y_j is the inter-filament distance at row number j, and B and W are the widths of the fibre bundle in y direction (quenching air direction) and perpendicular direction, respectively. The left-hand side of Eq. 3.150 represents the sum of all air friction forces within the bundle at any distance x. On the right-hand side, the first term describes the momentum in x direction within the bundle, the second term is the expression for the momentum of the air velocity component which has passed the bundle at distance $y = B$. Equation (3.150) is the expression for the global balance between air friction and momentum of the accelerated and deflected air in fibre direction x which is to be satisfied. As an initial value (subscript 0) for the iteration of k_{m} the result of the linear approximation ($v_{\mathrm{y0}} = \mathrm{const}$, $v(x) \propto x$) can be used:

$$k_{\mathrm{m,0}}(x) = \frac{2}{B\,W\,\varrho_{\mathrm{air}}\,x^2}\sum_{j}^{N_{\mathrm{r}}} N(j)\,F_{\mathrm{air}}(x,y_j)\;. \tag{3.151}$$

Radial symmetry. It is also possible to find similar analytical expressions for the air velocity in the case of radial symmetry and air flow from inside (e. g. from a blowing candle) to the outside (see Fig. 3.36, right-hand side, page 96). Concerning the rectangular cartesian case the procedures and the discussions are analogue to the treatment above. The following paragraph will only summarise the results. The Navier-Stokes and the continuity equations for the radial case are

$$\varrho_{\mathrm{air}}(v_{\mathrm{x}}\,v_{\mathrm{x,x}} + v_{\mathrm{r}}\,v_{\mathrm{x,r}}) = \eta_{\mathrm{air}}(v_{\mathrm{x,xx}} + v_{\mathrm{x,rr}}) + f_{\mathrm{x}} - p_{,\mathrm{x}}\;, \tag{3.152}$$

$$\varrho_{\mathrm{air}}(v_{\mathrm{x}}\,v_{\mathrm{r,x}} + v_{\mathrm{r}}\,v_{\mathrm{r,r}}) = \eta_{\mathrm{air}}(v_{\mathrm{r,xx}} + v_{\mathrm{x,rr}}) + f_{\mathrm{r}} - p_{,\mathrm{r}}\;, \tag{3.153}$$

$$v_{\mathrm{x,x}} + \frac{1}{r}\,v_{\mathrm{r,r}} + v_{\mathrm{r,r}} = 0\;. \tag{3.154}$$

Satisfying the continuity equation and decoupling the NAVIER-STOKES equation is possible by using the radial flow function $\Phi(x, r)$ with

$$\Phi(x, r) = x \cdot h(r) \ , \tag{3.155}$$

where $h(r)$ now is the solution of

$$\varrho_{\text{air}} \cdot x \cdot (h\, h' - r\, h\, h'' + r\, h'^2) = r^3\, f_{\text{x}} \ . \tag{3.156}$$

The prime ($'$) in Eq. 3.156 denotes the derivative with respect to the radial coordinate r. The velocity components are expressed by

$$v_{\text{x}}(x, r) = \frac{1}{r}\, \Phi_{,\text{r}} \ , \tag{3.157}$$

$$v_{\text{r}}(x, r) = -\frac{1}{r}\, \Phi_{,\text{x}} \ . \tag{3.158}$$

With the following approach for the force density

$$f_{\text{x}}(x, r) = x \cdot \kappa^2 \varrho_{\text{air}} \exp\left[2\, \alpha\, (r^2 - R_1^2)\right] \ , \tag{3.159}$$

an analytical solution for Eq. 3.156 can be found. Again, three different cases with respect to

$$\gamma = \frac{2\ \alpha \cdot v_1\, R_1}{\kappa} \tag{3.160}$$

are to be distinguished.

Case 1: $1 - \gamma^2 > 0$
The solutions are

$$\Phi(x, r) = -x \cdot \frac{v_1\, R_1}{\sqrt{1 - \gamma^2}} \exp\left[\alpha\, (r^2 - R_1^2)\right] \cos\Big(\frac{\kappa\, \sqrt{1 - \gamma^2}}{2\, v_1\, R_1}(r^2 - R_1^2) + c_1\Big) \ , \tag{3.161}$$

$$v_{\text{x}}(x, r) = x \cdot \kappa \cdot \exp\left[\alpha\, (r^2 - R_1^2)\right] \left[\sin\Big(\frac{\kappa\, \sqrt{1 - \gamma^2}}{2 v_1\, R_1}(r^2 - R_1^2) + c_1\Big) - \frac{\gamma}{\sqrt{1 - \gamma^2}} \cos\Big(\frac{\kappa\, \sqrt{1 - \gamma^2}}{2 v_1\, R_1}(r^2 - R_1^2) + c_1\Big)\right] \ , \tag{3.162}$$

$$v_{\text{r}}(x, r) = \frac{v_1\, R_1}{r\, \sqrt{1 - \gamma^2}} \cdot \exp\left[\alpha\, (r^2 - R_1^2)\right] \cos\Big(\frac{\kappa\, \sqrt{1 - \gamma^2}}{2 v_1\, R_1}(r^2 - R_1^2) + c_1\Big) \ , \tag{3.163}$$

with

$$c_1 = \arctan\Big(\frac{\gamma}{\sqrt{1 - \gamma^2}}\Big) \ . \tag{3.164}$$

Case 2: $1-\gamma^2=0$

$$\Phi(x,r) = -x\cdot v_1\,R_1\cdot\left[1-\alpha\,(r^2-R_1^2)\right]\exp\left[\alpha\,(r^2-R_1^2)\right]\,, \tag{3.165}$$

$$v_{\mathrm{x}}(x,r) = x\cdot 2\,\alpha^2 v_1\,R_1\left[1-\alpha\,(r^2-R_1^2)\right]\exp\left[\alpha\,(r^2-R_1^2)\right]\,, \tag{3.166}$$

$$v_{\mathrm{r}}(x,r) = \frac{v_1\,R_1}{r}\cdot\left[1-\alpha\,(r^2-R_1^2)\right]\exp\left[\alpha\,(r^2-R_1^2)\right]\,. \tag{3.167}$$

Case 3: $1-\gamma^2<0$

$$\Phi(x,r) = -x\,\frac{\alpha}{|\alpha|}\,\frac{v_1\,R_1}{\sqrt{\gamma^2-1}}\exp\left[\alpha\,(r^2-R_1^2)\right]\sinh\Big(d_1-\frac{\kappa\,\sqrt{\gamma^2-1}}{2\,v_1\,R_1}(r^2-R_1^2)\Big)\,, \tag{3.168}$$

$$v_{\mathrm{x}}(x,r) = x\cdot\kappa\cdot\frac{\alpha}{|\alpha|}\exp\left[\alpha\,(r^2-R_1^2)\right]\left[\cosh\Big(d_1-\frac{\kappa\,\sqrt{\gamma^2-1}}{2\,v_1\,R_1}(r^2-R_1^2)\Big)\right.$$
$$\left.-\,\frac{\gamma}{\sqrt{\gamma^2-1}}\sinh\Big(d_1-\frac{\kappa\,\sqrt{\gamma^2-1}}{2\,v_1\,R_1}(r^2-R_1^2)\Big)\right]\,, \tag{3.169}$$

$$v_{\mathrm{r}}(x,r) = \frac{\alpha}{|\alpha|}\,\frac{v_1\,R_1}{r\,\sqrt{\gamma^2-1}}\exp\left[\alpha\,(r^2-R_1^2)\right]\sinh\Big(d_1-\frac{\kappa\,\sqrt{\gamma^2-1}}{2\,v_1\,R_1}(r^2-R_1^2)\Big)\,, \tag{3.170}$$

with

$$d_1 = \operatorname{artanh}\Big(\frac{\sqrt{\gamma^2-1}}{\gamma}\Big)\,. \tag{3.171}$$

The discussion and application closely follow the analogue cases for the rectangular filament bundle.

Air Temperature

The basis for determination of the air temperature field $T_{\mathrm{air}}(x,y)$ is the energy equation of heat conduction and heat convection inside the fibre bundle. In analogy to the calculation of the air velocity field a two-dimensional steady state flow without free heat convection is assumed. The energy equation in cartesian coordinates is then given by

$$\lambda_{\mathrm{air}}(T_{\mathrm{air,xx}}+T_{\mathrm{air,yy}}) = c_{\mathrm{air}}\,\varrho_{\mathrm{air}}\,(v_{\mathrm{x}}\,T_{\mathrm{air,x}}+v_{\mathrm{y}}\,T_{\mathrm{air,y}})-q_{\mathrm{fib}}\,, \tag{3.172}$$

where $\lambda_{\mathrm{air}},\ c_{\mathrm{air}},\ \varrho_{\mathrm{air}}$ are the heat conductivity, the specific heat capacity, and the density of air, respectively.

The heat source density q_{fib} is equivalent to the heat transfer from fibre surfaces into air. Its mean value (for each fibre row at position y_{j}) is determined similarly to the calculation of force density. The heat quantity per length unit is given by the fibre cooling balance as follows

$$q_{\mathrm{fib}}(x,y) = \frac{1}{B\,W} \sum_{j=1}^{N_{\mathrm{r}}} N(j) \cdot Q \cdot c_{\mathrm{p}} \cdot \frac{\mathrm{d}T(x,y_j)}{\mathrm{d}x} \;, \tag{3.173a}$$

$$\approx \frac{N}{B\,W}\, \pi\, \lambda_{\mathrm{air}}\, Nu(x,y) \cdot \big(T(x,y) - T_{\mathrm{air}}(x,y)\big) \;, \tag{3.173b}$$

where $N(j), N_{\mathrm{r}}$ and N are the number of fibres in the j^{th} row, the number of rows, and the total number of filaments within the bundle, respectively. The product $B\,W$ is the cross-sectional area of the rectangular bundle. Instead of the real temperature profile of the air around each fibre, an effective average temperature field T_{air} is now calculated.

In the case of radial symmetry the corresponding relation to Eq. 3.172 for the heat energy is given as

$$\lambda_{\mathrm{air}}\big(T_{\mathrm{air,xx}} + T_{\mathrm{air,rr}} + \frac{1}{r}\,T_{\mathrm{air,r}}\big) = c_{\mathrm{air}}\,\varrho_{\mathrm{air}}\,(v_{\mathrm{x}}\,T_{\mathrm{air,x}} + v_{\mathrm{r}}\,T_{\mathrm{air,r}}) - q_{\mathrm{fib}} \;, \tag{3.174}$$

where the heat source density in the radial symmetric case is given as

$$q_{\mathrm{fib}}(x,y) = \frac{N}{R_2^2 - R_1^2}\, \lambda_{\mathrm{air}}\, Nu(x,r) \cdot \big(T(x,r) - T_{\mathrm{air}}(x,r)\big) \;. \tag{3.175}$$

Discussion. There is no analytical solution to the energy equations (3.172) or (3.174) within the filament bundle. The solutions can only be found numerically by transferring the partial differential equations into any adequate difference equations and using for example a five or more-points formula.

The amount of heat transportation by means of thermal heat conduction is insignificant in comparison to heat convection by air:

$$\lambda_{\mathrm{air}}(T_{\mathrm{air,xx}} + T_{\mathrm{air,yy}}) \ll c_{\mathrm{air}}\,\varrho_{\mathrm{air}}(v_{\mathrm{x}}\,T_{\mathrm{air,x}} + v_{\mathrm{y}}\,T_{\mathrm{air,y}}) \;. \tag{3.176}$$

For modelling, this suggests the possibility to simplify the energy equations through neglecting the heat conduction, which means the complete suppression of the left-hand side of Eq. 3.172 or 3.174. However, in such cases where no active quenching occurs or in the range between spinneret and onset of air blowing, the bundle sucks the air by itself (because of the pumping effect – the momentum balance has to be satisfied) and the air flow becomes symmetrical from both sides of the bundle to the center line. The result of these model assumptions is that no filament cooling takes place along the center line if the heat conductivity is not taken into account. Therefore, heat conductivity becomes essential especially for the symmetric flow cases and for the regions without active quenching. Additionally, there are always oscillations of fibres and air, turbulences, and free heat convection in real fibre spinning

processes. These effects increase of course the heat transfer described by the heat conduction term λ_{air} alone. For a more realistic simulation the influence of heat conduction should be taken into consideration by replacing the heat conductivity λ_{air} with an *effectively increased* term λ_{eff}.

On the other hand, the temperature slope for the air in spinning direction x is small in comparison to the slope in quenching direction y. While assuming $T_{\mathrm{air,xx}} \ll T_{\mathrm{air,yy}}$ the term $T_{\mathrm{air,xx}}$ can be neglected in Eqs. 3.172 and 3.174. Together with $a = \lambda_{\mathrm{air}}/(\varrho_{\mathrm{air}}\, c_{\mathrm{air}})$ and with Eq. 3.173b resp. 3.175 then follows

$$T_{\mathrm{air,yy}} = \frac{v_{\mathrm{x}}\, T_{\mathrm{air,x}} + v_{\mathrm{y}}\, T_{\mathrm{air,y}}}{a} - \frac{N \cdot \pi Nu\, (T - T_{\mathrm{air}})}{B\, W} \tag{3.177}$$

for the rectangular case, resp.

$$T_{\mathrm{air,rr}} + \frac{1}{r}\, T_{\mathrm{air,r}} = \frac{v_{\mathrm{x}}\, T_{\mathrm{air,x}} + v_{\mathrm{r}}\, T_{\mathrm{air,r}}}{a} - \frac{N \cdot Nu\, (T - T_{\mathrm{air}})}{R_2^2 - R_1^2} \tag{3.178}$$

for the radial symmetric case.

After the onset of quenching air the influence of heat conductivity within the fibre bundle can be neglected in comparison to the effects of the forced convection. The terms at the left-hand side in Eqs. 3.177 and 3.178 vanish and the equations to calculate the air temperature inside the fibre bundle are simplified to

$$v_{\mathrm{x}}\, T_{\mathrm{air,x}} + v_{\mathrm{y}}\, T_{\mathrm{air,y}} = \frac{N \cdot \pi Nu\, a\, (T - T_{\mathrm{air}})}{B\, W} \tag{3.179}$$

for the rectangular case, and

$$v_{\mathrm{x}}\, T_{\mathrm{air,x}} + v_{\mathrm{r}}\, T_{\mathrm{air,r}} = \frac{N \cdot Nu\, a\, (T - T_{\mathrm{air}})}{R_2^2 - R_1^2} \tag{3.180}$$

for the radial symmetric case, respectively.

Some Remarks to Boundary Conditions, Geometry, and Numerical Realisation

For the calculation of the air temperature fields $T_{\mathrm{air}}(x, y)$, resp. $T_{\mathrm{air}}(x, r)$, it is necessary to possess knowledge about

- the velocity fields of air $\boldsymbol{v}_{\mathrm{air}}(x, y)$, resp. $\boldsymbol{v}_{\mathrm{air}}(x, r)$ within the bundle
- the fibre temperature profiles $T(x, y_j)$, resp. $T(x, r_j)$ of each row j and the corresponding NUSSELT numbers $Nu(x, y_j)$ resp. $Nu(x, r_j)$ within the bundle, and
- the conditions at the borders of the bundle, the boundary conditions.

Air temperature. Knowledge of the air temperature profile at the boundaries of the rectangular region (see Fig. 3.40) is required in order to solve the partial differential equation (3.177) for the temperature field inside the bundle (the radial symmetric case can be treated in an analogous manner):

$$\begin{aligned}
&\text{region A}: && T_{\text{air}}(x=0,y) = T_{\text{air,spinneret}}(y)\ ,\\
&\text{region B, C}: && T_{\text{air}}(x,y=0) = T_{\text{air},0}(x)\ ,\\
&\text{region D, E}: && T_{\text{air}}(x,y=B) = T_{\text{air,B}}(x)\ .
\end{aligned}$$

The air temperature at the spinneret (region A in Fig. 3.40) is assumed to be equal to the spinneret temperature itself, this means that it is also equal to the initial fibre temperature T_0:

$$T_{\text{air}}(x=0,y) = T(0) = T_0\ .$$

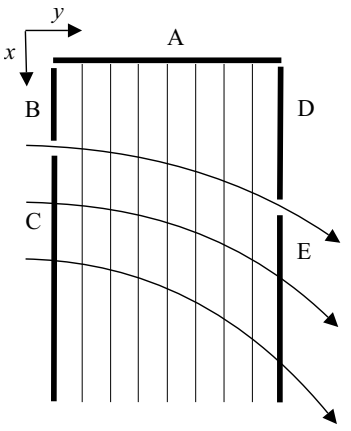

Fig. 3.40. Boundary conditions for rectangular fibre bundle: A – initial fibre temperature, B and D – unknown temperature, C – temperature profile of blowing air, E – temperature profile results from calculation

Near the spinneret and before the onset of quenching, that is the region where the filament bundle sucks air by itself, the temperature profile of the sucked air is normally unknown (region B and D in Fig. 3.40). The air temperature there is influenced by many factors, such as the geometry of the current spinneret design, the realised spinning conditions, the free heat convection, etc. It seems *impossible* to determine the air temperature in this region *a priori*. The only possibility to derive necessary boundary conditions for the calculation is to make an assumption regarding the air temperature based on *temperature measurement* in a real spinning process. The purely theoretical solution of the multifilament melt spinning problem in this region is impossible. This is due to the fact that the temperature profiles at the borders, required as input parameter, depend in a very complex way on the specialities of each respective spinning equipment. The boundary parameter may thus vary from case to case.

After the onset of quenching air (region C in Fig. 3.40) the boundary conditions for the windward side are given through the temperature profile and velocity profile of blowing air which are well-defined parameters in the melt spinning process. The velocity of the blowing air is much higher than the velocity of the self-primed air. Furthermore, the heat transfer becomes much more effective and can be described by means of the forced heat convection *alone*. Neglecting the slope $T_{\mathrm{air,yy}}$ dramatically simplifies the energy equation (3.179). No more information about the temperature profile at the leeward side is now needed (region E in Fig. 3.40).

There is a second difficulty besides the unknown boundary conditions in the region near the spinneret. The heat conductivity of air λ_{air} is too small to show any effect for realistic cooling behaviour along the centre line of the fibre bundle for the case where no active quenching is done by blowing air. The calculated temperature becomes nearly independent from the distance x in the centre. As discussed earlier, this unrealistic result can be improved by using an *effective* value of heat conductivity λ_{eff} (instead of λ_{air}) that takes into account oscillations, turbulences, and free convection effects. The comparison of calculated temperatures with values measured in real fibre spinning trials can be used to fit the effective heat conductivity to the measurements. The results from several experiments suggest a factor between $\lambda_{\mathrm{eff}} \approx (100 \ldots 200)\lambda_{\mathrm{air}}$.

Summarizing the discussion above, it can be said that near the spinneret and for regions without active quenching the air temperature needs to be calculated using the heat energy equation (3.177) (for the rectangular bundle), whereas the heat conductivity of air is taken into consideration and should be replaced with a more realistic effective value λ_{eff}. For the regions with active quenching and much higher air flow velocity the consideration of heat conductivity of air is no longer important and can be neglected. For this case the calculation can be carried out using Eq. 3.179.

Numerical realisation. For the simplest but most interesting case of constant force density across the fibre bundle, the velocity field of air is given by Eqs. 3.148 and 3.149 for the rectangular geometry (and the respective equations for the radial geometry). The improvement made by iterative calculation of the global mean value of force density k_{m} with respect to distance x follows from the global momentum balance equations (3.150) (resp. the radial correspondence). For iteration the use of the *dampened* NEWTON procedure is helpful:

$$k_{\mathrm{m}}^{(i+1)}(x) = k_{\mathrm{m}}^{(i)}(x) - \delta \frac{\widetilde{F}\big(k_{\mathrm{m}}^{(i)}(x)\big)}{\widetilde{F}'\big(k_{\mathrm{m}}^{(i)}(x)\big)} \,, \tag{3.181}$$

where $\widetilde{F}$ is given by the air friction momentum balance

$$\widetilde{F} = \sum F_{\mathrm{air},i} - W \int_0^x \varrho_{\mathrm{air}}\, v_{\mathrm{x}}\, v_{\mathrm{y}}\, dx' - W \int_0^B \varrho_{\mathrm{air}}\, v_{\mathrm{x}}^2\, dy \tag{3.182}$$

for rectangular bundle geometry, and

$$\widetilde{F} = \sum F_{\mathrm{air},i} - 2\,\pi\,R_2 \int_0^x \varrho_{\mathrm{air}}\,v_{\mathrm{x}}\,v_{\mathrm{r}}\,dx' - 2\pi \int_{R_1}^{R_2} \varrho_{\mathrm{air}}\,v_{\mathrm{x}}^2\,r\,dr \tag{3.183}$$

for the radial geometry, respectively. The dampening factor $\delta < 1$ avoids too rapid changes within the iteration process and supresses oscillations. The results of the linearised assumptions can be used as the initial value $k_{\mathrm{m}}^{(0)}$ to start the iteration procedure with

$$k_{\mathrm{m}}^{(0)}(x) = \frac{2}{\varrho_{\mathrm{air}}\,B\,W\,x^2} \sum F_{\mathrm{air},i}(x) \tag{3.184}$$

for the rectangular bundle geometry, and

$$k_{\mathrm{m}}^{(0)}(x) = \frac{2}{\varrho_{\mathrm{air}}\,\pi\,(R_2^2 - R_1^2)\,x^2} \sum F_{\mathrm{air},i}(x) \tag{3.185}$$

for the radial geometry, respectively. For the cases of non-constant force density across the bundle ($\alpha \neq 0$, Eqs. 3.125, 3.159) the convergence region for the iteration procedure is to be carefully observed. The starting values $k_{\mathrm{m}}^{(0)}$ above can only be successfully used if $|2\,\alpha\,B| \ll 1$, or $\left|\gamma\,(R_2^2 - R_1^2)\right| \ll 1$.

The partial derivatives of the energy equations (3.177) and (3.178) can be replaced with difference quotients expressed by any adapted point-formula. If the second derivative $T_{\mathrm{air,yy}}$ (resp. $T_{\mathrm{air,rr}}$) is taken into account for the symmetric case, the result is a (three-)diagonal system of algebraic equations which can be effectively solved with LD-dissection. On the other hand, if the conduction effects can be neglected, a simple step procedure may be carried out. In the latter case the numerical procedure is quite similar to the solution procedures for the earlier described cell-method (see page 94). To accelerate the convergence for the alternating calculations of the multifilament system (fibres – air – fibres – air ...) it is convenient to use only the Nusselt number and then simultaneously calculate the fibre temperatures again, according to Eq. 3.10.

In principle, the only reason to start the calculation procedure with the model of fibre formation first is its simplicity. At first, the calculation of the fibre formation is done based on any assumption concerning the environmental air. Then the air velocity and air temperature are determined on the basis of the air friction force and the heat exchange from fibres to bundle. After that, fibre formation calculation is carried out again, and so forth until no further significant changes can be observed. Depending upon the starting values and the current spinning parameters (and also on the step width and number of rows) sufficient convergence can be reached after approximately three to five calculation runs. A modern personal computer (1 GHz processor clock rate for example) only needs seconds to complete the calculations.

Geometrical limits. The described method for modelling the multifilament melt spinning process is easy to manage and leads to quick calculations which allow to assess technological parameters with respect to optimised spinning conditions for high quality fibre products. But the model is restricted to the assumption of *free boundary conditions at the leeward side*. The pressure gradient $p_{,\mathrm{x}}$ vanishes only for the free leeward side and it is possible to use the harmonic functions for computing the air velocity components within the bundle. This means that the deflection of air is *only* caused by means of air friction from the filaments alone. There is no influence of any walls of the quenching chamber affecting the leeward side. The quenching air flow originates on the windward side (or from inner side to outer side in radial geometry), and air flow deflection is only caused by the fibres. If there are no fibres then no air flow deflection occurs. On the other hand, if any wall is located at the leeward side then the boundary conditions are not free anymore as in the before mentioned manner, the deflection of air will then be caused by both the filaments *and* the wall. The same effect occurs if quenching air flow is reached from both sides to the centre (or from outer to inner side in case of radial geometry). The effect of the wall can then be replaced with a symmetry line. Furthermore, the pressure gradient $p_{,\mathrm{x}}$ cannot be neglected anymore since the streamlines result from both, air friction from fibres and from the geometrical conditions of the quenching chamber. The further use of the developed model is only possible if some modifications are implemented. Firstly, the streamlines of air have to be determined depending upon the geometry of the quenching chamber. Secondly, the influence of air friction of the fibres needs to be considered. The latter can be achieved, for example, with the described concept of the *varying force density* $k_{\mathrm{m}}(x)$. Figure 3.41 illustrates the basic idea.

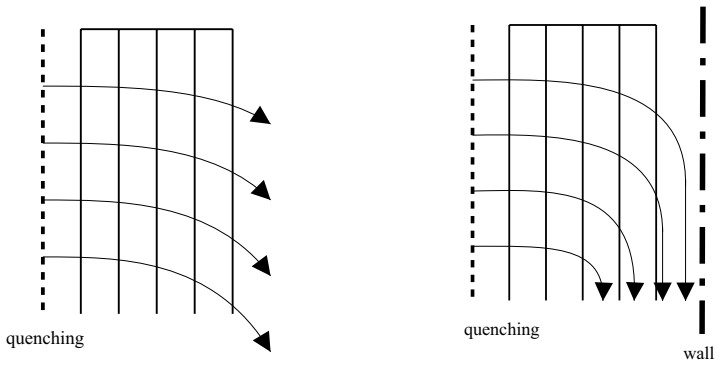

Fig. 3.41. Boundary conditions on leeward side. *Left:* free boundary, air deflection is caused only by fibres; *right:* no free boundary, air deflection is caused by wall *and* fibres, the influence of the wall can be treated by replacing it with a symmetry line

3.2.4 Example 1: Numerical Simulation of Fibre Formation in the Staple Fibre Melt Spinning Process

The PET staple fibre melt spinning with rectangular geometry of the filament bundle, as the introductory discussed on page 92 shall now be treated by means of the outlined model for different quenching conditions. The spinning parameters are as follows

polymer:	poly(ethylene terephthalate) (PET),
spinneret:	1300 holes, 13 rows with 100 holes on each row,
	dimension W x B: 26 cm x 6.5 cm, rectangular,
	diameter of capillary holes: 0.30 mm,
melt temperature:	$T_0 = 290\,^{\circ}\mathrm{C}$,
throughput:	$Q_{\mathrm{PET}} = 1300 \times 0.6$ g/min = 780 g/min,
take-up velocity:	$v_{\mathrm{L}} = 1200$ m/min,
quenching:	cross quenching from one side,
	beginning 5 cm below spinneret,
	temperature $T_{\mathrm{air}} = 25\,^{\circ}\mathrm{C}$,
	velocity (1) $v_{\mathrm{air}} = 1.5$ m/s,
	length of quenching zone $L_{\mathrm{air}} = 1.0$ m .

The results of the calculation are shown in the following figures. Figure 3.42 depicts the streamlines of air flow within the filament bundle. The deflection of air in fibre direction can be clearly seen on the left hand side of the figure. The air sucking effect from both sides below the spinneret, in the 5 cm region free of quenching air flow, is also shown on the right-hand side of the figure. Next, Fig. 3.43 shows the temperature of air within the bundle (the isotherms); there is a transition from symmetric temperature distribution below the spinneret to asymmetric distribution after the start of quenching at distance $x = 5$ cm.

Figure 3.44 illustrates the experimental verification of the calculated air temperature. The diagram depicts the dependency of air temperature T_{air} on distance x from spinneret at three positions: at windward side, in the center, and at leeward side. The temperature at windward side is a given boundary condition (and thus cannot be used for verification). The temperature inside the bundle seems impossible to be measured, but the temperature at the leeward side, when the air has passed the bundle, can be determined easily.

Unevenness of the Filament Properties

The air flow and air temperature distribution within the filament bundle lead to different environmental conditions for each filament row which influence their cooling and air friction behaviour. It is obvious that any retarded cooling caused by higher air temperature increases the length of the fibre formation zone and affects the resulting filament properties. The longer the fibre formation zone (the distance from the spinneret exit to the solidification

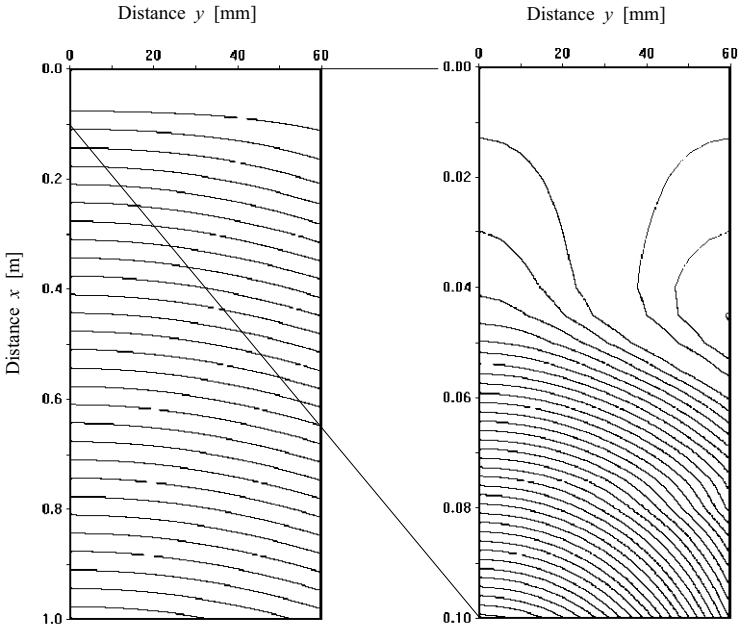

Fig. 3.42. Air flow (streamlines) inside the filament bundle. The magnified region below spinneret ($x = 0 \ldots 0.1$ cm) is presented again at the right part of the figure; spinning parameter: PET staple fibre spinning process, see before

point) the greater the exposition to air friction, and the higher the part of the friction force. On the other hand, the deflection of air into fibre direction (especially at leeward side) reduces the air friction coefficient and therefore can also reduce the friction force. Both effects interact and it depends on the current spinning and geometric conditions if and how the resulting stress at the solidification point changes and thus the connected fibre properties. The following figures show the courses of temperature (Fig. 3.45) and tensile stress (Fig. 3.46) for fibres within the bundle in three selected rows, one at the windward side (row #1), one in the centre of the bundle (row #7), and one at the leeward side (row #13).

Under the prevailing conditions near the spinneret the filaments at windward side and leeward side (the outer sides of the filament bundle) are subjected to higher cooling rates compared to the filaments in the center of the bundle. The symmetric conditions of geometry and air flow in the region near the spinneret also result in symmetric courses of fibre formation. But after the onset of (asymmetric) quenching air the cooling rates change to the (expected) sequence of windward-centre-leeward and the courses of fibre formation also become asymmetric, as expected. The solidification points for the individual filaments are reached at different positions. As discussed in the section about the modelling of fibre formation, the stress at the solidification

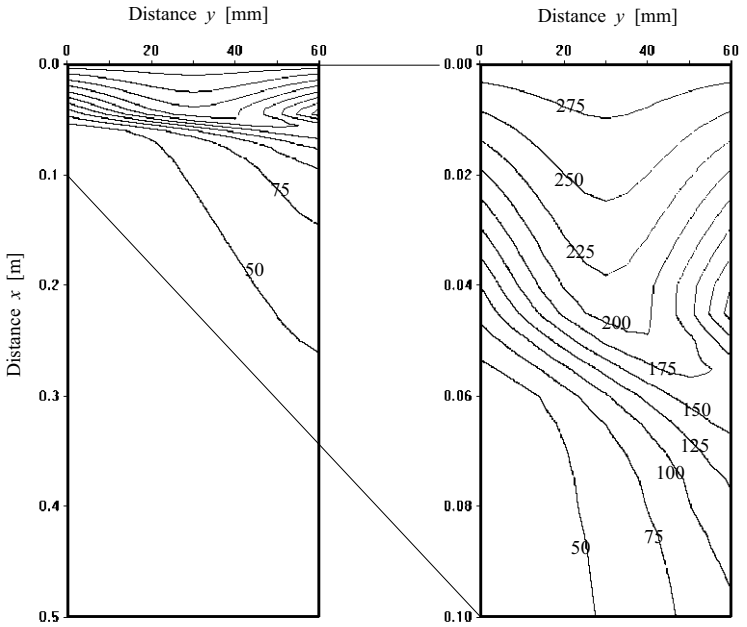

Fig. 3.43. Air temperature (isotherms) inside the filament bundle with quenching air blowing from the left hand side. The magnified region below spinneret ($x = 0 \ldots 0.1$ cm) is presented again at the right part of the figure; temperatures are indicated (℃); spinning parameter: PET staple fibre spinning process, see before

point essentially determines the fibre orientation and its resulting properties. Figure 3.47 shows the stress at the solidification points and the corresponding elongations to break across the fibre bundle. The lowest stress at the solidification point, the lowest orientation and consequently the highest elongation to break (the highest draw ratio) is not attained to the fibres at leeward side of the bundle but inside the bundle at row #9. This (for the moment unexpected) result is a direct consequence of the conditions near the spinneret. The course of graphs in the diagram Fig. 3.47 does not appear very smooth, but the scattering results from the numerical effect of rounding the numbers to limited digits. In principle the numerical accuracy and smoothness of the graphs can be improved.

In order to indicate the tranversal uneveness of the filaments (the variation of the orientation over the bundle cross section) the maximum and minimum elongation to break can be used to define the variation coefficient $CV_{\varepsilon_\mathrm{b}}$:

$$CV_{\varepsilon_\mathrm{b}} = \frac{\varepsilon_{\mathrm{b,max}} - \varepsilon_{\mathrm{b,min}}}{\varepsilon_{\mathrm{b,min}}} \cdot 100\,\% \,. \tag{3.186}$$

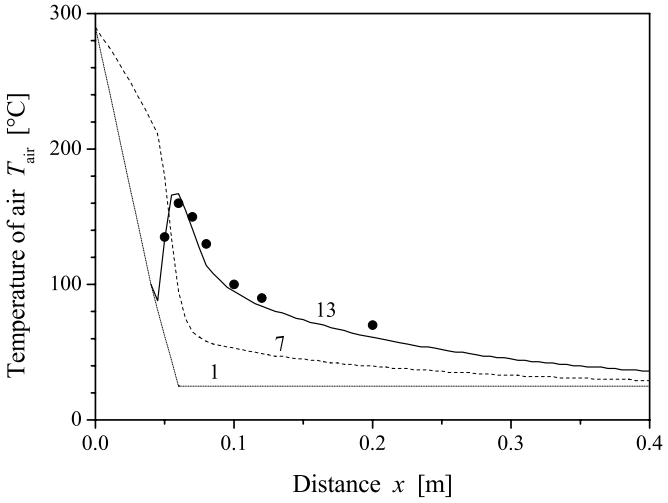

Fig. 3.44. Air temperature inside the filament bundle at three different positions: 1 – windward side (row #1), 7 – center of the bundle (row #7), 13 – leeward side (row #13), symbols: measured temperature at leeward side; data source: Institute of Polymer Research Dresden

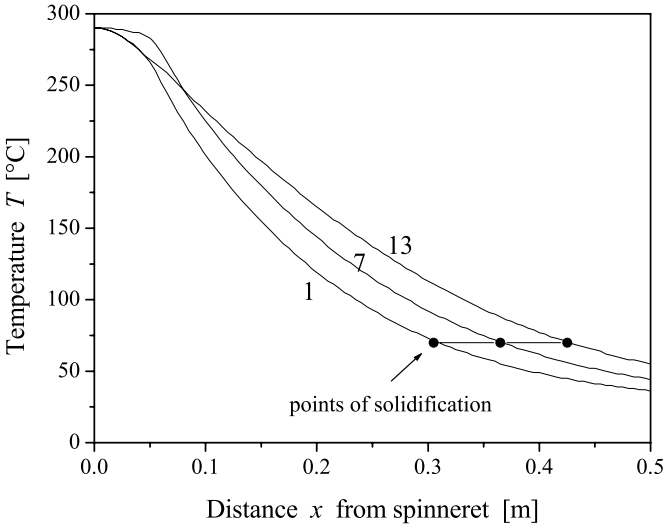

Fig. 3.45. Filament temperature $T(x)$ (calculated) for three different locations: 1 – windward side (row #1), 7 – centre of the bundle (row #7), 13 – leeward side (row #13), the position of solidification points at T_s =70 ℃ is indicated; spinning parameter: PET staple fibre spinning process, see before

With the results shown in Fig. 3.47 the variation coefficient of orientation (resp. elongation to break) is $CV_{\varepsilon_b} = 3.6\,\%$.

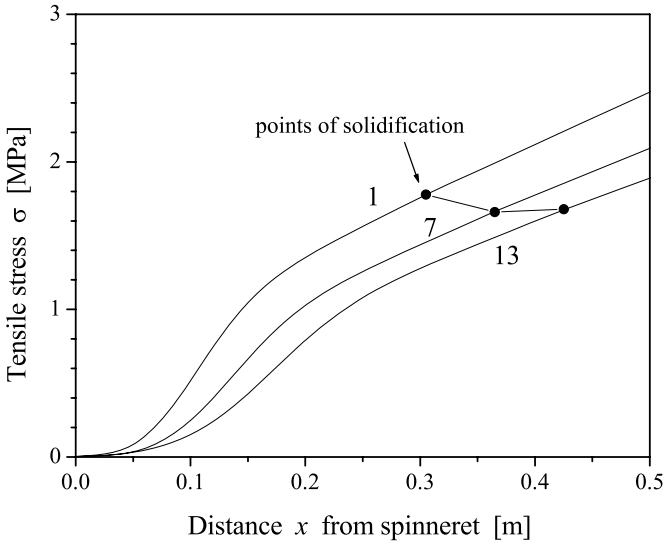

Fig. 3.46. Filament tensile stress $\sigma(x)$ (calculated) for three different locations: 1 – windward side (row #1), 7 – center of the bundle (row #7), 13 – leeward side (row #13), the position of solidification points is indicated; spinning parameter: PET staple fibre spinning process, see before

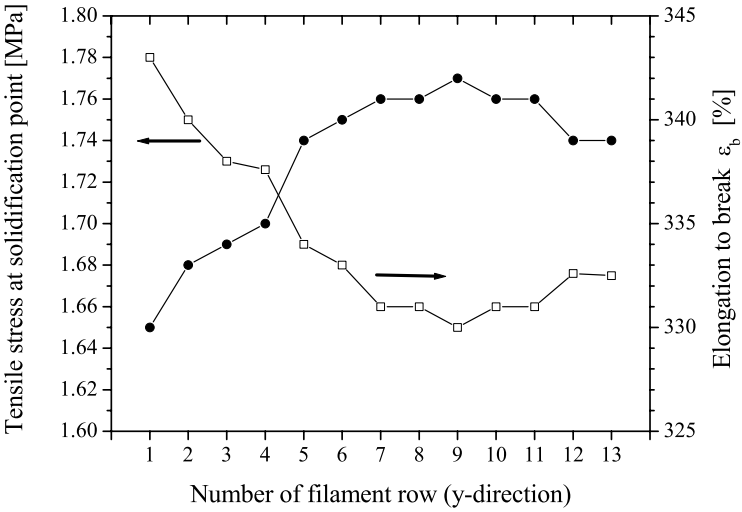

Fig. 3.47. Filament stress $\sigma(x_s)$ at solidification point and corresponding elongation to break (calculated) across the fibre bundle: rows #1 to #13; spinning parameter: PET staple fibre spinning process, see before

The variation coefficient changes by modifying the process parameters, but only small improvements are possible. Neither changes in throughput,

extrusion temperature nor take-up velocity can entirely prevent this geometrically associated variance. An example is shown in Fig. 3.48 which depicts the trace of the maximum and minimum elongation to break and the variation coefficient CV_{ε_b} versus the take-up velocity. The throughput in this example was related to the take-up velocity in order to achieve a constant filament fineness.

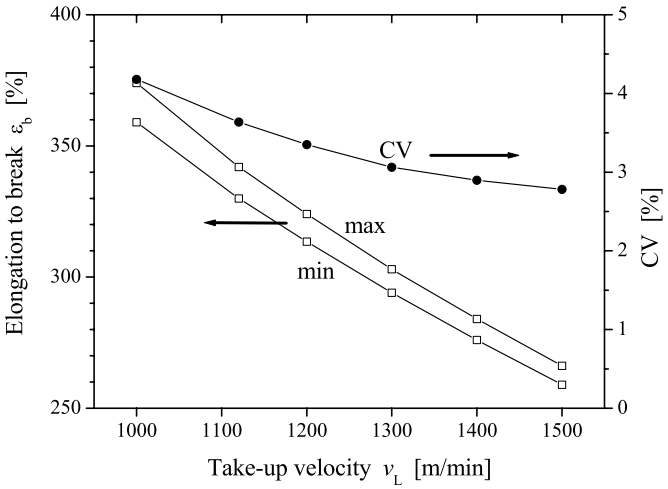

Fig. 3.48. Maximum and minimum elongation to break and corresponding coefficient of variation CV_{ε_b} in dependence on take-up velocity, constant filament fineness

Effect of Quenching Air Profile

The influence of changing the quenching air velocity on both the filament cooling and to the uneveness of filament orientation across the bundle will be briefly discussed in this section. Five different cases are considered, such as no active quenching, and quenching air velocities of 0.5, 1.5, 2.0 and 3.0 m/s. The case of 1.5 m/s air velocity was already mentioned, the figures of the previous section can be directly compared to the following ones. The air blowing starts again at distance $x = 5$ cm below the spinneret, the different profiles of blowing air velocity and temperature are shown in Fig. 3.49.

The resulting streamlines and the air temperatures within the filament bundle for the three cases (#A, #B, #D) are shown in Fig. 3.50.

It is obvious that the different velocity profiles affect the fibre properties. Table 3.11 summarises the maximum and minimum elongations to break together with the corresponding CV-value for each case. Additionally, results of the calculations with $v_{air} = 1.5$ m/s (#C) and $v_{air} = 3.0$ m/s (#E) are

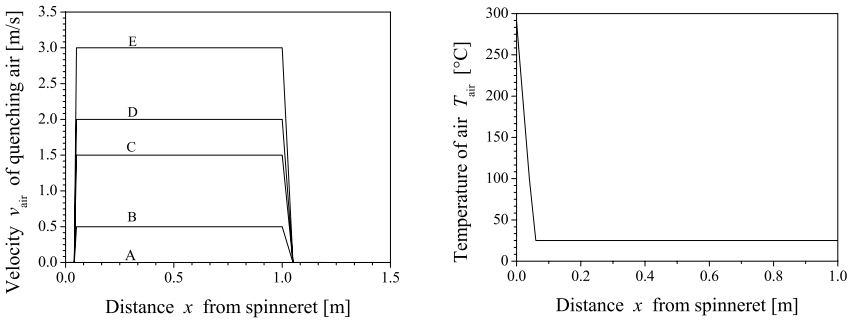

Fig. 3.49. Velocity profiles (*left*) and temperature profile (*right*) of quenching air, as used for calculation example

shown. It becomes clear that increasing the quenching air velocity increases the eveness but also makes the process unstable if a critical value of air velocity is reached. On the contrary, extremly high air velocities do not result in a further decrease of uneveness. One reason for that is that the initial rheological force F_0 plays a more important role for fibre formation at low take-up velocities than inertial or air friction force. The initial force F_0 is essentially determined from the conditions near the spinneret. Therefore it should be possible to maximise the eveness by means of an adapted mass throughput or by adapted temperature regime, respectively.

Table 3.11. Maximum and minimum elongation to break for different quenching air velocity profiles

	Air velocity	ε_{max} in %	ε_{min} in %	CV_{ε_b} in %
A:	no active quenching	397	363	9.4
B:	$v_{air} = 0.5$ m/s	361	334	8.1
C:	$v_{air} = 1.5$ m/s	342	330	3.6
D:	$v_{air} = 2.0$ m/s	338	325	4.0
E:	$v_{air} = 3.0$ m/s	332	320	3.8

In general, stress at the solidification point becomes less dependent upon spinning conditions at high take-up velocities. This is because the inertia force then dominates the tensile stress. But at lower take-up velocities (which are commonly used in the staple fibre spinning process and in the example above) the stress at the solidification point can be influenced by spinning conditions near the spinneret.

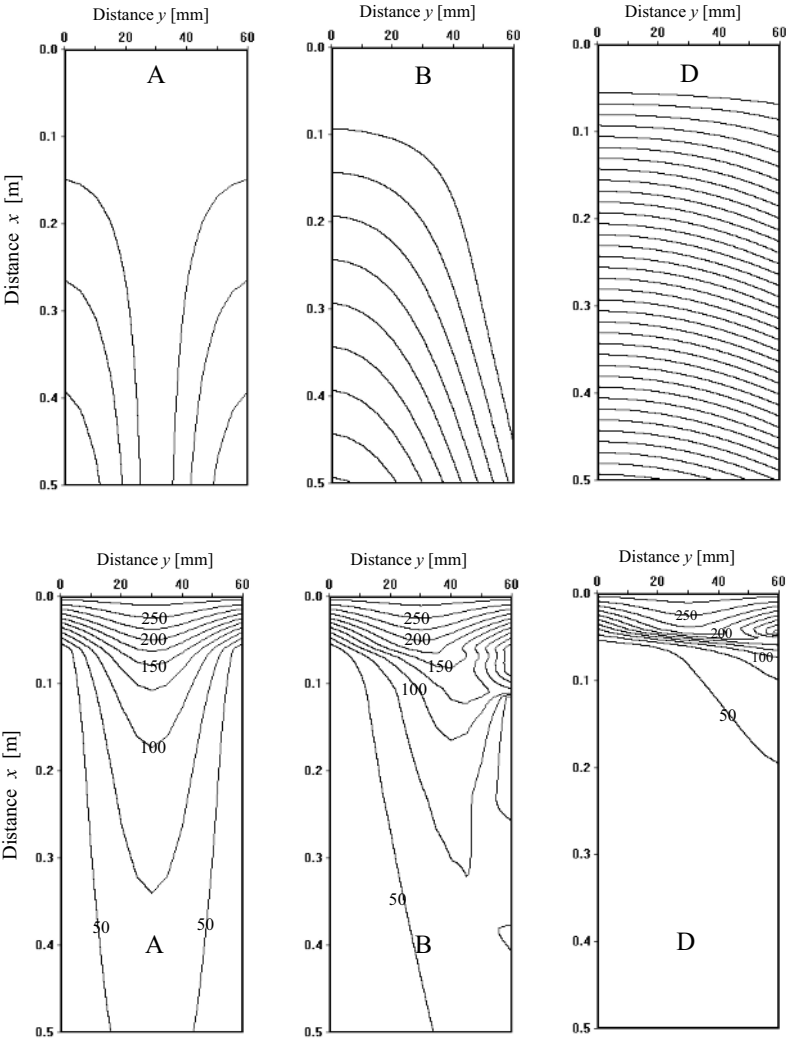

Fig. 3.50. Streamlines (*upper row*) and temperature (*lower row*) of air inside the filament bundle, *A:* no active quenching, *B:* $v_{\mathrm{air}} = 0.5$ m/s, *D:* $v_{\mathrm{air}} = 2.0$ m/s, the temperature of the isotherms is indicated

Effects of Adapted Temperature Distribution and Mass Throughput

The nearly parabolic characteristic of the elongation to break behaviour which is shown in Fig. 3.47 can be corrected by a gradual adjustment of the mass throughput and/or melt temperature distribution for the filaments on each individual row of the spinneret. One possibility is to create a spe-

cific temperature distribution across the spinneret plate (Fig. 3.51). The melt temperature distribution has to affect the distribution of elongation to break in opposite direction. The higher melt temperature at the windward side for example first leads to a lower viscosity of the polymer melt and, under the assumption of constant melt pressure, a higher mass throughput can be expected. Secondly, the higher temperature also affects the cooling length of the fibres. Both effects act in the same direction and result (theoretically) in a totally uniform orientation distribution across the bundle. The disadvantage is that a filament bundle of such configuration indeed shows uniform orientation but non-uniform fineness distribution. The filaments possess different diameters resulting from the different throughputs. Besides that, it seems to be difficult to implement the technical means for such temperature gradient controlled spinneret plate under industrial conditions.

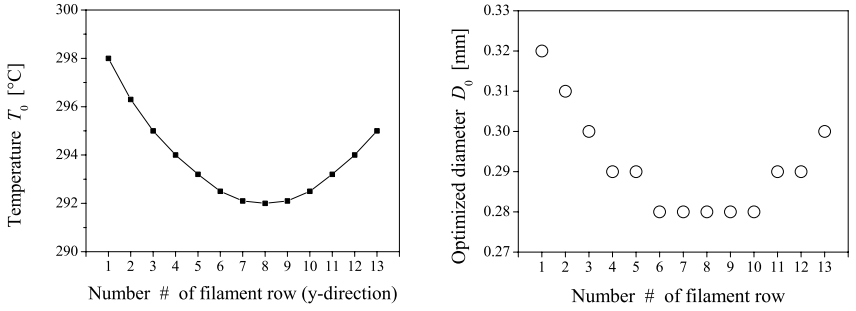

Fig. 3.51. Optimised melt temperature profile (*left*) and optimised capillary diameters (*right*)

Another possibility to influence the mass throughput in the described manner is to adjust the diameters of capillary holes in the spinneret. A similar idea was already proposed earlier, with diameters gradually reducing from windward to leeward side. The model calculation now allows to predict the exact stepwise adaption of the hole diameters of each row. It indicates the adaption of larger diameters at the windward side followed by the leeward side and holes of smaller diameters in the centre. Figure 3.51 provides a proposal for five stages of spinneret hole diameters. The corresponding Table 3.12 shows that, by adapting these five grades, the initial variation coefficient of the elongation to break of nearly 4% drops to a quarter, and, adapting only three grades still results in a drop of variation to half of the initial value. The disadvantage of uneven fineness of course remains.

In principle it should be possible to combine the adapted melt temperature profile and the adapted capillary hole diameter distribution to minimise *both* effects, that of uneven orientation *and* uneven fineness. But in practice the realisation seems difficult and may only be achieved under very special conditions.

Table 3.12. Optimised spinneret hole diameters

Number of stages	Diameter in [mm]	Fineness in [dtex]	CV_{ε_b} in [%]
1	0.30	18	4
3	$0.29 \cdots 0.31$	$16 \cdots 19$	2
5	$0.28 \cdots 0.32$	$14 \cdots 21$	1

Effect of Retarded Cooling

A more effective and also easy to realise approach which does not change the individual filament mass throughputs is the carefully designed asymmetrical cooling program for the filament bundle. Since the cooling rate for the filament rows in the centre of the tow near the spinneret cannot be increased and is always lower than that at the outer sides, the conclusion is to delay the cooling rate of the filament rows at the windward and leeward side by means of adapted booster heating. The lateral quenching exemplary adopted here results in non-uniform cooling down of the windward side, the centre, and the leeward side, respectively. A compensation of the non-uniform cooling can be attained via asymmetrically designed booster heating near the spinneret. The model calculation now allows to find the optimum temperature profile at windward and leeward sides that provides (theoretically) for reduction to zero of the CV value of the orientation. In practice the aim is to minimise the variation of the orientation and the resulting uneveness of elongation to break in order to achieve high quality yarns and to realise stable process conditions and high productivity.

Figure 3.52 shows an optimised velocity and temperature profile of quenching air, and Fig. 3.53 depicts the effect of the optimised profile to the air temperature within the bundle. The air quenching starts 10 cm below the spinneret. The region between spinneret at $x = 0$ and beginning of air blowing is heated to different temperatures for the windward and the leeward side, respectively.

Figure 3.53 can be directly compared with Fig. 3.43. The next diagram (Fig. 3.54) shows the courses of fibre temperatures for three different positions inside the bundle. A comparison with Fig. 3.45 illustrates the retarded cooling. The higher temperature near the spinneret mainly influences the initial rheological forces F_0 of the fibres and therefore also the total forces at each solidification distance. The result of booster heating is the nearly uniform distribution of stress at solidification points versus the filament rows and at last nearly uniform filament orientations. Figure 3.55 shows the calculated elongations to break across the fibre bundle in comparison with the original (unoptimised) variant. The coefficient of variation for the elongation to break CV_{ε_b} changes from initially 3.6% to 0.8%.

As the mean orientation of the bundle is simultaneously reduced, a higher draw ratio in the following drawing stages becomes possible and opens up the

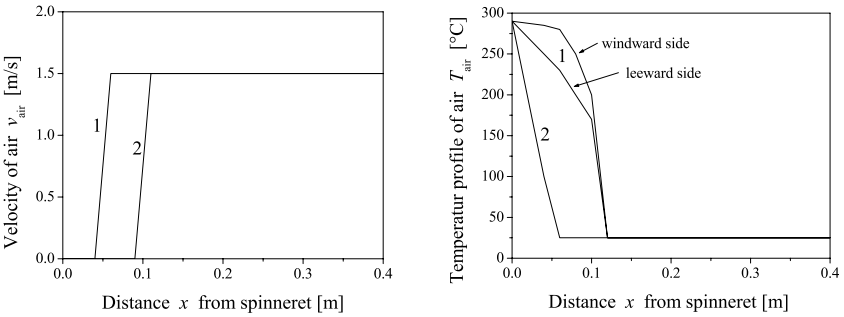

Fig. 3.52. Optimised profiles (#1) of air. *Left:* Velocity profile at windward side; *right:* Air temperature profiles at windward and leeward sides, the profiles of the example before (#2, see Fig. 3.49-C) is shown for comparison

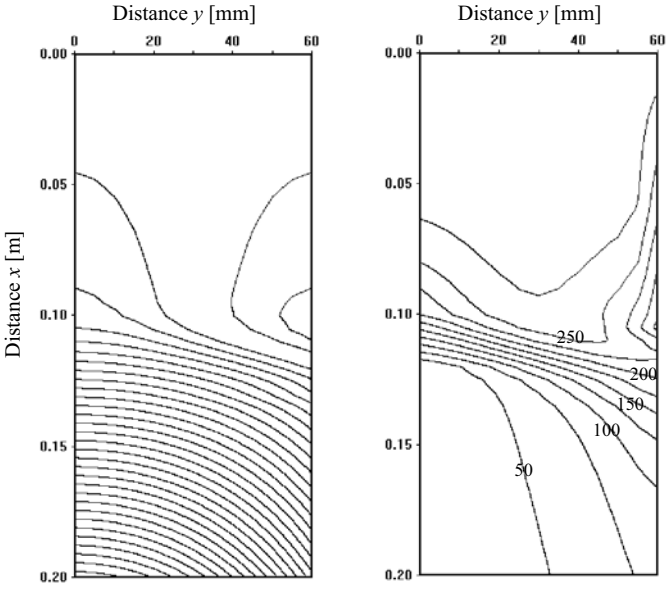

Fig. 3.53. Streamlines (*left*) and temperatures (*right*) of air inside the filament bundle for optimised air profiles, the temperature of the isotherms is indicated. Only the region 20 cm below spinneret is shown, please compare to Figs. 3.43 and 3.42

additional opportunity of increasing the mass throughput (increased productivity) with equal target fibre fineness. For the discussed example this would lead to an increased productivity of about 4...5%. A further advantage of the method of retarded cooling is its adabtability and flexibility. The method allows for easy and quick adaptions to changes in production technology [262].

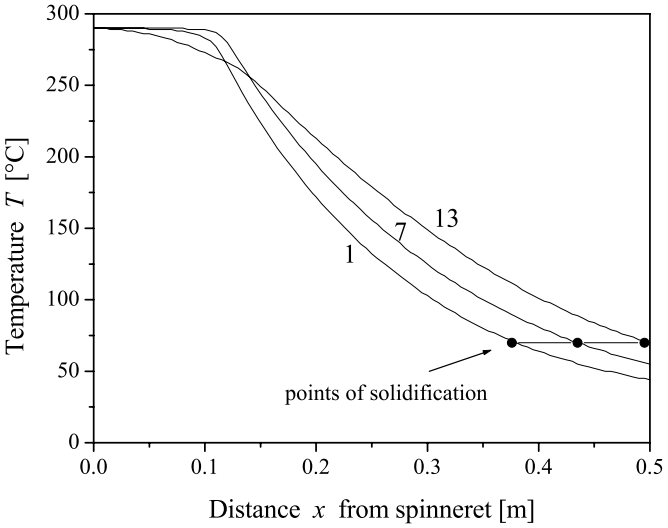

Fig. 3.54. Filament temperature $T(x)$ (calculated) for three different locations: 1 – windward side (row #1), 7 – center of the bundle (row #7), 13 – leeward side (row #13), the positions of solidification distances are indicated; optimised air profile

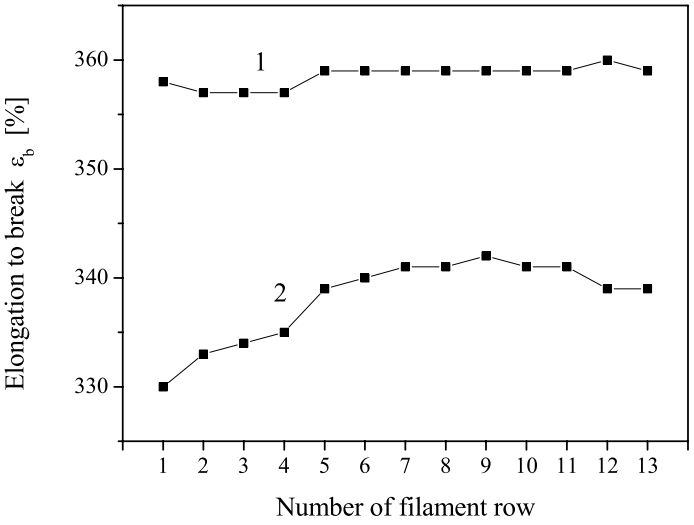

Fig. 3.55. Elongation to break (calculated) across the fibre bundle (row #1 to #13) for the optimised air profile, $CV_{\varepsilon_b} = 0.8\%$ (1), results of the origin variant (Fig. 3.47) as comparison, $CV_{\varepsilon_b} = 3.6\%$ (2)

3.2.5 Example 2: Modelling of Fibre Formation in the Spunbonded Nonwoven Process

The spunbonded nonwoven process represents a typical multifilament spinning process because of its high number of filaments which can be up to a multiple of thousands. Take-up of the filaments is usually achieved by means of air friction, either in an excess-pressure or in an underpressure process, or sometimes a combination of both. Hajji, Misra, Spruiell et al. [263, 264] discussed the application of a modified single filament model to the *Reicofil* spunbonding nonwoven process and found good agreement between experimental and predicted data for their investigation. The following section deals with the application of both single filament and multifilament fibre formation models to the underpressure spunbonding nonwoven process in order to attain high filament velocities and low filament finenesses. The discussion is based on investigations which were carried out by the authors together with the *Saxon Textile Research Institute Chemnitz* [265]. The questions for the investigations were the following: Which dependencies exist for the underpressure process between the filament velocity and the filament fineness on the one hand and the spinning and take-up condition on the other? What are the best energetic conditions for the air suction device? How is the take-up to be designed to enable high filament velocities? Some answers can be given with the help of the applied fibre formation model.

Friction Forced Filament Take-up

The specialty of the process is that the filament take-up is not realised by means of godets or a winder like in the conventional yarn spinning processes but via drag of an air stream in spinning direction (Fig. 3.56). Contrary to the fibre spinning process where the final fibre velocity is fixed, the take-up velocity resulting from air drag force is not known from the beginning and thus cannot be treated as an initial spinning parameter. The higher the velocity of the axial air stream the higher the friction and drag force transferred to the fibre – thus the higher the fibre velocity. Furthermore, the higher the fibre velocity the lower its diameter (at constant mass throughput) and the lower the resulting friction and driving of the fibre. Consequently, the intentional effect will be reduced as the resulting air drag itself depends upon the difference between the velocities of fibre and air and also on the fibre fineness. The final fibre velocity, its fineness and all corresponding properties result from the balance between the air drag transferred to the fibre and the inherent fibre force contributions like the rheological, inertial, and gravitational forces, respectively.

When trying to solve the differential equations of the fibre formation model it becomes obvious that the initial value F_0 for the force at the spinneret is unknown. This causes no difficulties in the case of conventional take-up by means of godets or a winder because the initial rheological force in the

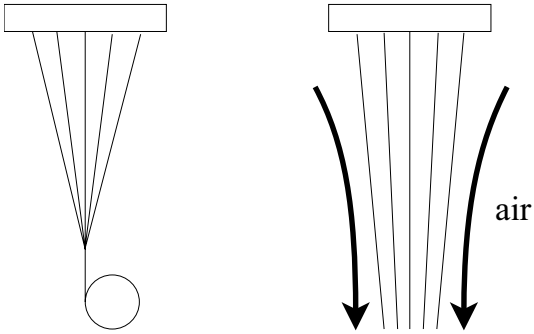

Fig. 3.56. Comparison between conventional yarn melt spinning process (*left*) and nonwoven process with air drag take-up (*right*)

model can be determined via an iteration procedure, that is, until the final take-up velocity is reached within an adequate numerical tolerance. However, the situation regarding the take-up by means of air drag is quite different because the final take-up velocity results from an equilibrium of forces and therefore is unknown from the beginning.

The simplest idea to solve this problem is to assume the initial rheological force is equal to zero $F_0 = F(0) = 0$ [263, 264]. But the problem can be more accurately solved in general by means of an additional iteration if the rheological force is known (or can be estimated) at *any* distance x of the fibre path. Especially the usage of a take-up channel (see below) opens up the possibility to get a much better assumption for the missing boundary value.

Figure 3.57 illustrates the basic idea of modelling the effect of a take-up channel. The possible technical realisation of an underpressure nonwoven equipment is also depicted. The positions of entrance and exit of the take-up channel (measured from the spinneret at $x = 0$) are x_1 and x_2, respectively.

The tensile force F for a single filament at entrance x_1 of the take-up channel is given by (see Eq. 3.11a on page 50 – the force balance)

$$F(x_1) = F_0 + Q \cdot (v(x_1) - v_0) + \int_0^{x_1} \frac{\varrho_{\mathrm{air}}}{2} c_{\mathrm{f}}\, \tilde{v}^2\, \pi\, D\, dx - \int_0^{x_1} \varrho_{\mathrm{p}}\, g\, \frac{\pi}{4}\, D^2\, dx\ , \tag{3.187}$$

where $\tilde{v}$ is the difference between the velocities of fibre and surrounding air, respectively, $\tilde{v} = |v - v_{\mathrm{air}}|$. The tensile force must be equal to the force applied inside the take-up channel:

$$F(x_1) = F_{\mathrm{e}} + \int_{x_1}^{x_2} \frac{\varrho_{\mathrm{air}}}{2}\, c_{\mathrm{f}}\, \tilde{v}^2\, \pi\, D\, dx - \int_{x_1}^{x_2} \varrho_{\mathrm{p}}\, g\, \frac{\pi}{4}\, D^2\, dx\ . \tag{3.188}$$

If the fibre is already solidified at the entrance $x = x_1$ of the channel, which means the fibre velocity and diameter are fixed and the air velocity inside

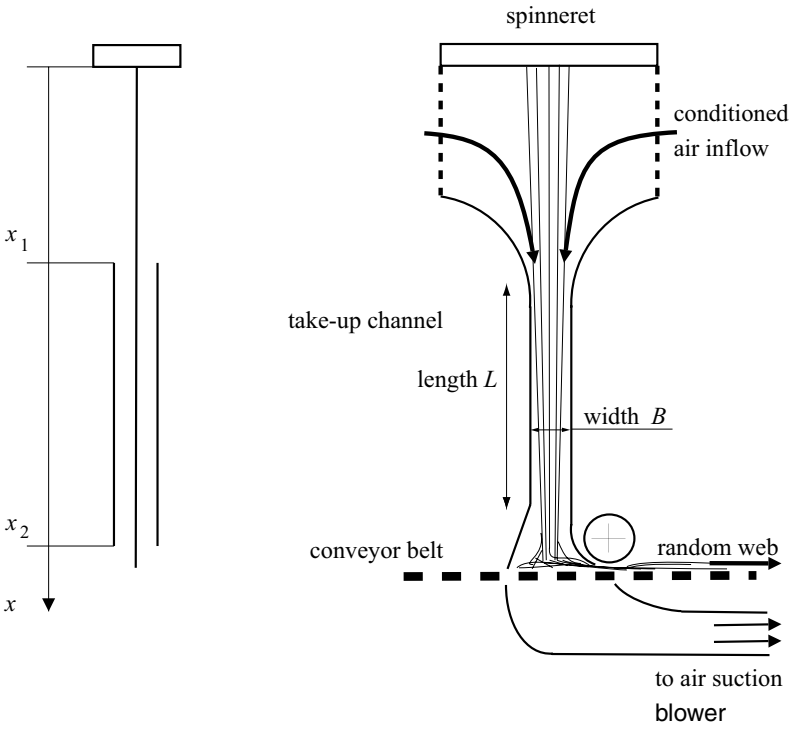

Fig. 3.57. Principle of the take-up channel (*left*) and possible realisation of an underpressure spunbonding nonwoven process (*right*)

the channel can also assumed to be constant, then (3.188) is simplified to

$$F(x_1) = F_\mathrm{e} + L\,\frac{\varrho_\mathrm{air}}{2}\,c_\mathrm{f}\,\tilde{v}^2\,\pi\,D - L\,\varrho_\mathrm{p}\,g\,\frac{\pi}{4}\,D^2\ . \tag{3.189}$$

The term $F_\mathrm{e} = F(x_2)$ is the tensile force at the exit of the channel and $L = x_2 - x_1$ is the channel length. Both equations can be combined together for all distances x. If careful attention is payed to the signs of air friction force contribution inside and outside of the take-up channel follows

$$F(x) = F_0 + Q\cdot(v(x) - v_0) + \Theta\int_0^x \frac{\varrho_\mathrm{air}}{2}\,c_\mathrm{f}\,\tilde{v}^2\,\pi\,D\,dx - \int_0^x \varrho_\mathrm{p}\,g\,\frac{\pi}{4}\,D^2\,dx\ , \tag{3.190}$$

with

$$\Theta = \begin{cases} 1 & \text{for} \quad v(x) > v_\mathrm{air} \\ -1 & \text{for} \quad v(x) < v_\mathrm{air} \end{cases}\ . \tag{3.191}$$

The initial tensile force F_0 correlates with the initial fibre velocity gradient dv/dx at $x = 0$ and therefore determines the final velocity after integration.

The only reasonable assumption for the equilibrium of forces at any distance is that the tensile force vanishes at the exit of the take-up channel

$$F(x_2) = 0 \,. \tag{3.192}$$

This condition replaces the boundary condition of a fixed take-up velocity. With the air profile $v_{\mathrm{air}}(x)$ given and the equations of fibre modelling, it is now possible to calculate the final fibre velocity and all connected characteristics of fibre formation.

High Filament Velocities – Realised by Means of an Underpressure Spunbonding Nonwoven Process

Subject of the investigations described below is the design of an underpressure spunbonding nonwoven equipment that realises high filament velocities up to 3000 m/min and filament finenesses of 1...2 dtex [265]. Boundary conditions are: the maximum total height of the equipment of less than 3 m and the limited power of the air suction blower. With help from the fibre formation model it was possible to accompany the design process and to give useful hints for the construction.

Inside the upper part of the underpressure spunbonding nonwoven equipment, the air entrance chamber, the air flow behavior should be a symmetrical (Fig. 3.57). Assuming a channel width of $B = 20$ mm, height of entrance chamber of $H = 1$ m, and mean value of the air velocity inside the channel of $v_{\mathrm{channel}} = 3000...6000$ m/min, then follows for the air entrance velocity v_{entr}:

$$v_{\mathrm{entr}} = \frac{B}{H} \cdot v_{\mathrm{channel}} = 1...2 \text{ m/s} \,.$$

The amount of entrance air velocity is comparable to the quenching air velocity for the staple fibre multifilament spinning example treated in the section before. Therefore the model of symmetrical flow behaviour can be used to calculate the multifilament effects on individual fibre formation, for example to estimate the differences in cooling behaviour of filaments located at the inner and outer side of the bundle, respectively. Figure 3.58 elucidates the application of the model for melt spinning of polypropylene.

For this process it must be assured that the filament temperatures inside the take-up channel are lower than any given critical temperature in that manner, and that no sticking occurs while the filaments touch each other or the walls of the channel. The solidification which represents the end of the fibre formation zone is not fixed because it depends on the spinning conditions, especially on the mass throughput, the melt temperature, and the kind of polymer material (with its property of heat capacity). Additionally, the cooling rate is retarded in the centre of the filament bundle. Therefore each set of spinning conditions determines a minimum distance x_{min} where the temperatures of all filaments is lower than the critical temperature:

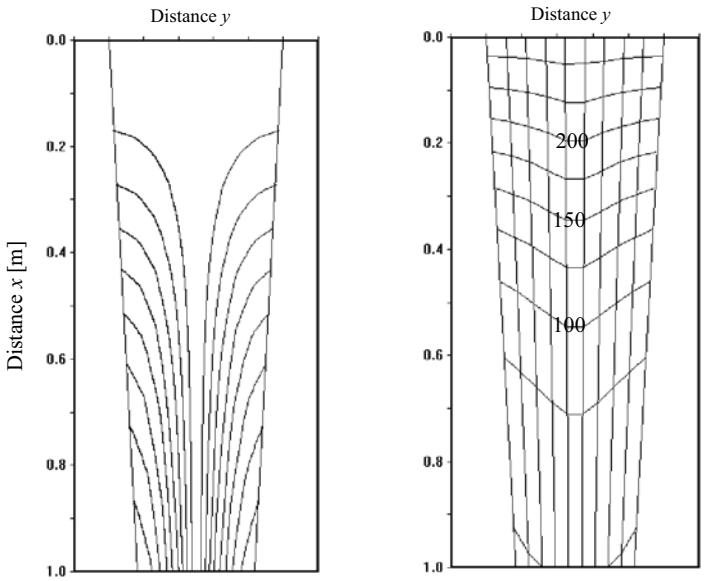

Fig. 3.58. Example of multifilament model application to the underpressure spunbonded nonwoven process. *Left:* streamlines of air, *right:* filament temperatures (isotherms), temperatures in ℃ indicated

$$T(x_{\min}) < T_{\text{crit}} \ . \tag{3.193}$$

The next figure (Fig. 3.59) shows the distances where the polypropylene filaments reach the temperature of $T_{\text{crit}} = 100\,℃$ as example.

It can be seen that for the indicated spinning conditions these distances are always lower than 1 m; therefore the minimum distance of $x_{\min} \approx 1$ m according to the mass throughput of $Q = 1$ g/min is a sufficient distance between the spinneret and the entrance of the take-up channel. The calculation also confirms the assumption that the final filament velocity depends nearly linearly on the length L of the take-up channel. The calculation also provides relationships to describe the dependence of final velocity on air velocity inside the channel (see Figs. 3.60, 3.61).

At last the theoretical investigations allow to estimate the pairs of air velocity v_{channel} within the channel and corresponding length L of the channel to reach a destined filament velocity (Fig. 3.62). From the figures it can be seen that the conditions to reach 3000 m/min filament velocity are approximately the following: channel length ≈ 1 m, driving air velocity ≈ 100 m/s.

The task of reaching a defined air velocity inside the take-up channel of a given length and width is due to the power and energetic conditions of the air suction blower and depends upon pressure losses of the channel together with other parts of the spinning device. The longer the channel, the

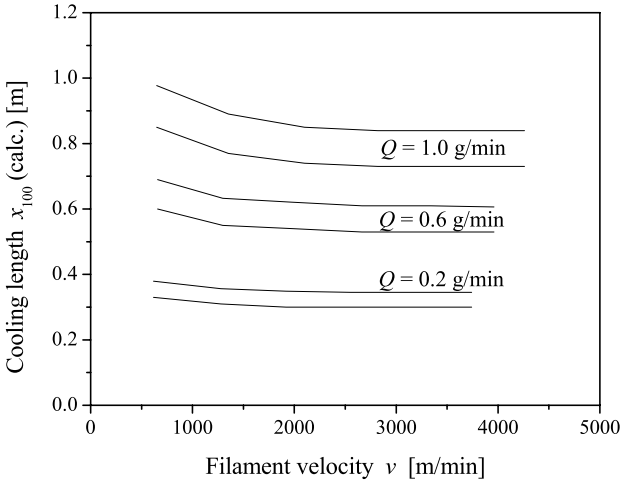

Fig. 3.59. Cooling length x_{100} (calc.) vs. final filament velocity v (upper and lower limit for filaments at center and boundaries of the bundle); polymer: polypropylene (PP), melt temperature: 260 ℃, air temperature: 25 ℃, three different mass throughputs (per hole) are indicated

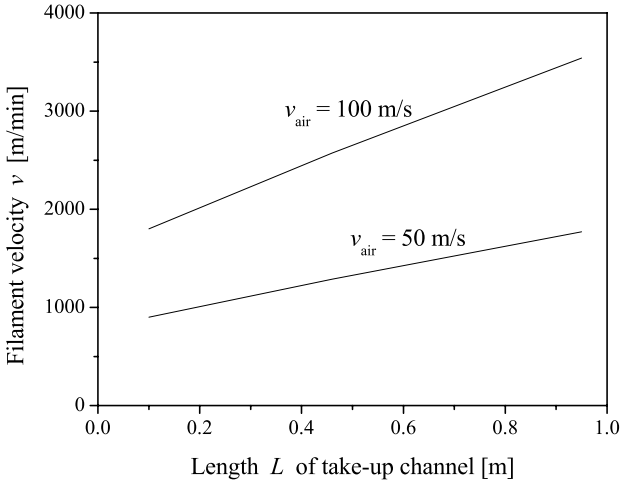

Fig. 3.60. Final filament velocity v (calc.) vs. length L of the take-up channel, two different velocities of air inside channel (indicated), other spinning conditions: see Fig. 3.59

higher the pressure losses and the lower the resulting air velocity inside, but the higher the exposed length of the filaments to air friction force. On the other hand, there is an optimum channel width B for a given length L to achieve maximum possible air velocity. The smaller the channel width from this optimum value the higher the pressure losses, and the higher the channel

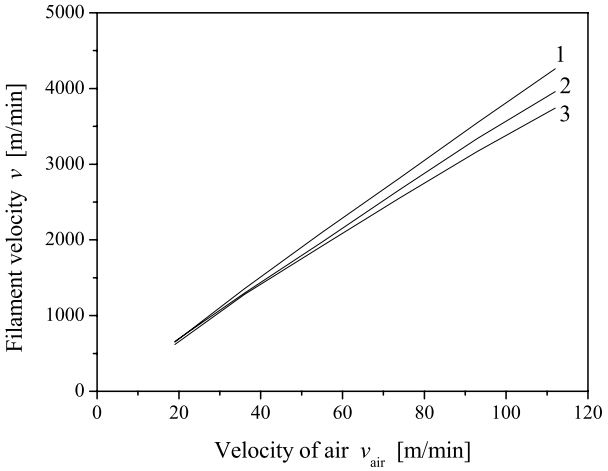

Fig. 3.61. Final filament velocity v (calc.) vs. air velocity v_{channel} inside take-up channel, three different mass throughputs (per hole) indicated: 1 – 1 g/min, 2 – 0.6 g/min, 2 – 0.2 g/min, other spinning conditions: see Fig. 3.59

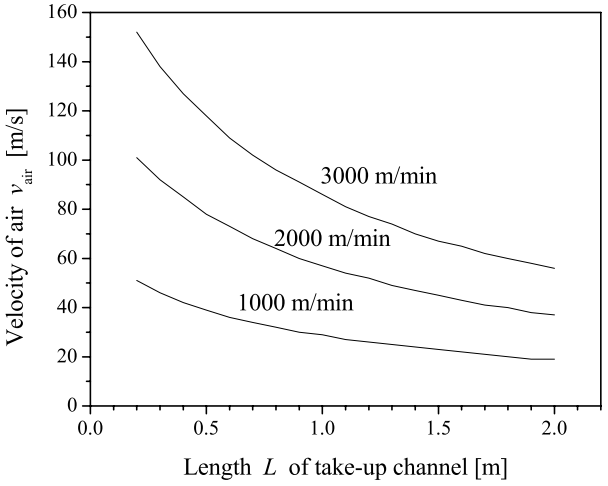

Fig. 3.62. Combinations for length L of take-up channel and air velocity v_{channel} to destined final filament velocity v (indicated), mass throughput (per hole) 0.6 g/min, other spinning conditions: see Fig. 3.59

width from the optimum, the higher the cross section area and the lower the resulting air velocity. For the investigated equipment [265] the optimum channel width was $B = 20$ mm. At last Fig. 3.63 shows the finally reached filament velocities and finenesses depending upon the air velocity inside the channel for the investigated equipment.

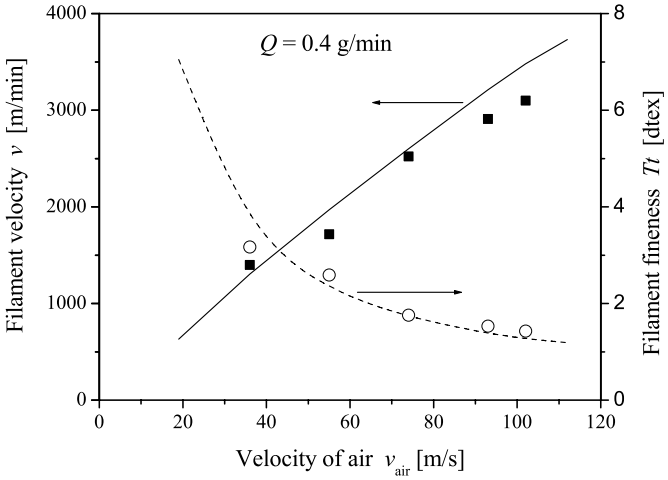

Fig. 3.63. Final filament fineness Tt and final filament velocity v in dependence on the velocity of air inside take-up channel v_{channel}, mass throughput (per hole): 0.4 g/min, *lines*: calculated, *symbols*: measured values

3.2.6 Summary

Process modelling and simulation seems to be an effective way in order to solve engineering problems. Computer simulations can indeed be a helpful tool for understanding the principle behaviour of the considered process. But one has to keep in mind that information generated by the computer program is always based on any physical and/or mathematical model of the real process, and this describes the essential aspects of the treated process only in a relatively qualified manner. The simulations can never replace the experimental work and the empirically collected experiences, but they can powerfully support the laboratory and industrial research in order to avoid time-consuming and/or expensive investigations regarding process modification, extension, or optimisation, respectively. Especially the last mentioned task of optimisation is typical for engineering procedures in melt spinning: the prediction of resulting fibre properties after changing the process parameters, geometrical conditions, the used material, or to optimise the process with respect to productivity and quality. The example treated above shows how the computer simulation was used to support the design of a special melt spinning device for underpressure spunbonded nonwoven equipment. Here, the theory of fibre formation together with the *engineering* modelling of the entire process allowed for the determination of major dependencies and relations regarding material properties, process conditions and characteristics of fibre formation. This knowledge, combined with additional empirical results enabled the successful design of the device which provided for the desired

filament velocity of 3000 m/min, and filament finenesses of 1...2 dtex, respectively.

The results of any simulation are always to verify on the basis of experimental data. It is possible to measure on-line the filament velocity, the filament diameter, the temperature, and orientation (birefringence) depending upon distance from the spinneret and to correlate the process conditions with the resulting fibre properties. A serious model should be based on such experimental background. Secondly, such a model should also be tractable and for engineering purposes easy to handle. The models of fibre formation, available after more than 40 years of development, do not satisfy all these requirements. Some important effects cannot be described well so far but only in an approximative manner (e. g. the theory of crystallisation in fibre formation). Some relations must be fitted to experimental data due to the lack of a satisfactory theory. On the other hand, there are also reliable empirical data missing for some polymer types, especially for the non-isothermal behaviour under high stresses and high deformation rates. Therefore, the model of fibre formation consists of both well investigated and exact relations but also of approximations valid only for special conditions or within certain ranges. For any successful engineering the need for the combination of *both* model simulation *and* empirical experience is obvious.

3.3 Limits of Fibre Formation in Melt Spinning and Spinnability

3.3.1 Maximum and Minimum Fineness

The limits of the melt spinning process can be estimated by some simple physically based considerations [266, 267]. At first, we want to look at the maximum possible fineness $Tt_{\max}$. The fineness of the as-spun filament is given by the quotient $Tt = Q/v$. Additionally, for the final drawn and full oriented fibre the necessary draw ratio DR to reach final fineness Tt_{f} has to be considered: $Tt_{\mathrm{f}} = Q/(v \cdot DR)$. This means that in order to reach the maximum possible fineness, the highest possible mass throughput Q and the minimum possible take-up velocity v has to be used. The draw ratio itself depends upon the spinning conditions, mainly on the take-up velocity. One has to regard that cooling down of the polymer stream strongly relates to the mass throughput (see Sect. 3.1, Fig. 3.23 on page 85) to realise the maximum fineness. The higher the mass throughput per hole the longer the distance to the solidification point. A simple demand for stable melt spinning and avoidance of fibre breaks means that the fibres need to be cooled down below the solidification temperature before their first contact with the preparation applicator or any other fibre guidance element, respectively. The minimum length $L_{\min}$ of the spinning tube has to exceed the solidification distance: $L_{\min} > L_{\mathrm{s}}$. After solidification in general no further deformation of the fibres

occurs. But sometimes it is required that a certain minimum fibre temperature has to be reached in order to avoid sticking effects between the filaments and the guidance elements or between the filaments themselves. In Fig. 3.64 on the left-hand side the distance L_{50} is required to reach the temperature $T = 50$°C and the solidification distance L_s for spinning of PA 6 at three different mass throughputs depending upon the take-up velocity is shown. For higher take-up velocities ($v \geq 3500$ m/min) where stress induced spinline crystallisation takes place the solidification occurs above the glass transition temperature of $T_g \approx 50$°C. But for maximum fibre fineness the lower take-up velocities ($v \leq 3000$ m/min) should be preferred so that the fibre temperature at the solidification point equals the glass transition temperature of $T_g = 50$°C for PA 6. The figure on the right-hand side depicts the calculated cooling distance $L_{50} \approx L_s$ vs. mass throughput Q for different take-up velocities of up to 3000 m/min. The upper curve in the picture represents the relationship $L_{50}(Q)$ for the minimal possible take-up velocity v_{min} which itself is determined by the minimal possible take-up distance (this is the solidification distance) and the resulting gravitational force. The calculation based on the minimal possible take-up velocity v_{min} was carried out in such way that the resulting spinline stress shows a nearly constant or an only very small increasing behaviour vs. the spinning distance x, that means that the minimum take-up velocity has to be greater at least than the velocity of freely falling fibre. At the solidification point the spinline stress for all variants reaches an extremly low value: $\sigma_s = 10 \ldots 15$ kPa. The processing for PA 6 then results in fibres with no (or very low) orientation and possible draw ratios of about $DR \approx 6$.

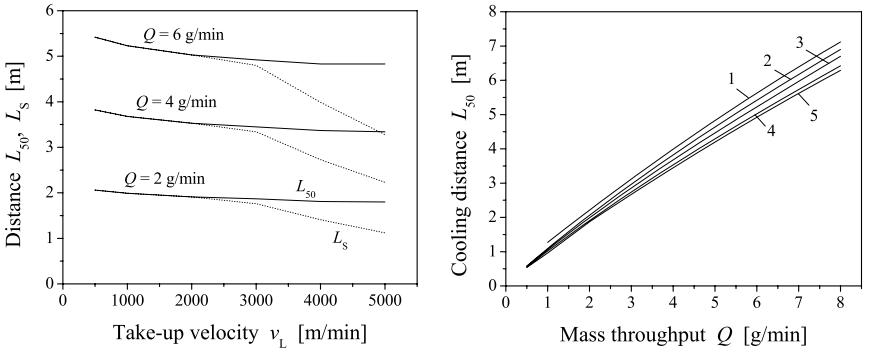

Fig. 3.64. *Left:* (calculated) distance L_{50} required to reach fibre temperature $T = 50$°C (*solid lines*) and solidification distance L_s (*dotted lines*) vs. take-up velocity v, mass throughput (per hole) indicated; *right:* cooling distance L_{50} vs. mass throughput Q, different take-up velocities: 1 – minimum possible (150 ... 300 m/min), 2 – 500 m/min, 3 – 1000 m/min, 4 – 2000 m/min, 5 – 3000 m/min, *Spinning parameter:* PA 6, molecular weight: 17 000, melt temperature: 265°C, no additional air quenching

Figure 3.65 shows on the left-hand side the thermal limitations for regarding the maximum possible fineness (*after drawing* to final elongation to break of 25%) determined in terms of necessary cooling length vs. take-up velocity. The figure on the right-hand side shows the maximum possible fineness $Tt_{\max}$ depending upon the throughput Q after drawing with draw ratio $DR = 6$, applying the minimal possible take-up velocity $v_{\min}$ and under the condition of an adapted optimum cooling distance.

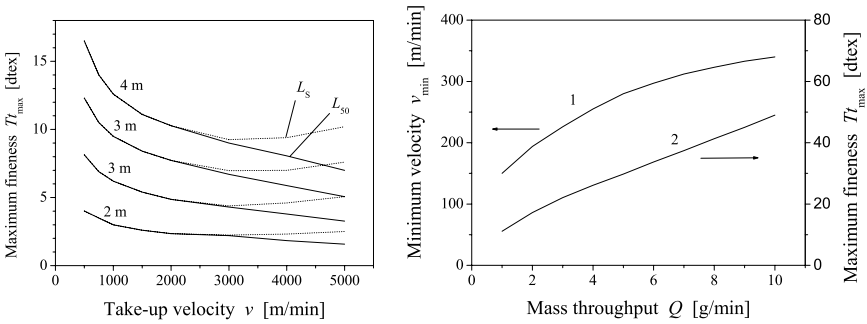

Fig. 3.65. *Left:* limitation curves for maximum fineness $Tt_{\max}$ (after drawing) vs. take-up velocity v, cooling length L_{50} is indicated; *right:* (calculated) maximum possible fineness $Tt_{\max}$ (1) (after drawing) and minimum possible take-up velocity $v_{\min}$ (2) vs. mass throughput Q (per hole), adapted spinning length; *Spinning parameter:* PA 6, molecular weight: 17 000, melt temperature: 265°C, no additional air quenching

The maximum possible finenesses presented here are theoretical values, of course, and estimated without any additional air quenching. Inclusion of quenching should further stabilise the (low tension) spinning process. Resultingly, it can be stated that regarding the filament fineness the upper limit for conventional spinning equipment with cooling lengths of $L = 4 \ldots 6$ m for PA is in the range of $30 \ldots 40$ dtex after drawing. For PET the required cooling lengths are somewhat smaller, and the maximum possible fineness slightly increases. In order to achieve any further increase of filament fineness the conventional cooling by means of air is to be replaced by more effective cooling methods, e. g. cooling and solidification in a water quench.

Remark. It must be mentioned that if the melt is extruded at very high throughputs (high flow rates) the melt stream becomes distorted. These distortions are known as *melt fracture* [268] where the extrudate shows instabilities in form of spiral or gross flow behaviour or surface roughness and the so-called sharkskin effect. These phenomena have been studied by many investigators and are still up to now not fully understood.

The minimum possible fineness after drawing should be reached with minimum throughput Q, maximum possible take-up velocity v and (if possible) high draw ratio DR:

$$Tt_{\mathrm{DR}} = \frac{Q}{v \cdot DR} \,. \tag{3.194}$$

The fibre orientation and therefore the resulting possible draw ratio are determined by the stress at the solidification point and depend upon the take-up velocity (see Sect. 3.1, Fig. 3.22 on page 84). The higher the take-up velocity the higher the tensile stress and also the degree of orientation and the lower the residual draw ratio. Figure 3.66 (*left-hand side*) shows the resulting fineness before and after the drawing (to final elongation of 25%) of PA 6 fibres in a spinning process with increasing take-up velocity and constant mass throughput. The advantage of getting minimum fineness after drawing is not very effective due to the fact that, with increasing take-up velocity the orientation increases and thus the draw ratio decreases. On the other hand, the reduction of throughput directly decreases the fineness and only slightly increases the fibre orientation resp. reduces the residual draw ratio. However, the effect of increasing orientation in the case of decreasing throughput is smaller than in the case of increasing velocity. To get minimal fineness, the reduction of throughput is much more effective than increasing the spinning speed (Fig. 3.66, *right-hand side*).

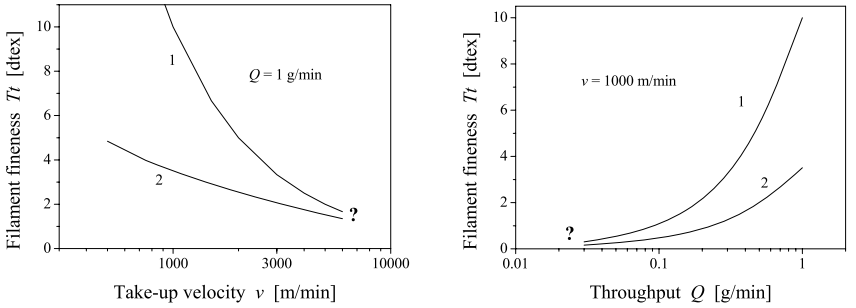

Fig. 3.66. (Calculated) filament fineness before drawing (1) and after drawing (2) of PA 6 vs. take-up velocity v (*left*) resp. vs. mass troughput Q (*right*), constant throughput and take-up velocity, respectively; the limits (marked with symbol **'?'**) are unknown and depend strongly on the material and the processing parameter

Increasing the take-up velocity and decreasing the mass throughput rapidly border on the physical limits of the process. The higher the take-up speed the higher the resulting spinline stress and the extensional deformation rate of the material. This may cause filament breakages due to brittle cohesive fracture or visco-elastic ductile failure. In the next section some aspects of the failure behaviour will be discussed.

An estimation of the limiting conditions with respect to fibre stress in the spinning line can be made as follows: After solidification the tensile stress must not exceed the critical stress level that may cause secondary deformation. Figure 3.67 shows on the left-hand side the fibre stress σ_{L} at certain distances L depending upon take-up velocity v_{L}. The example is calculated for single PA 6 filaments with mass throughput $Q = 1$ g/min. The distance to solidification for low take-up velocities when temperatures reach 50°C is about $L_{\mathrm{s}} \approx L_{50} \approx 1$ m. For higher take-up velocities the distance L_{s} becomes smaller, however, the cooling distance L_{50} remains nearly constant. The filament stress strongly increases with take-up velocity, at longer distances L it is mainly caused by air friction. To avoid unwanted secondary deformation, the critical stress for PA 6 is assumed to be $\sigma_{\mathrm{crit}} \approx 50$ MPa. The condition $\sigma_{\mathrm{L}} < \sigma_{\mathrm{crit}}$ leads to the picture at the right-hand side of Fig. 3.67, which depicts the maximum possible take-up velocity and the resulting minimum fineness for the given mass throughput depending upon the take-up distance L before and after drawing to 25% of final elongation. The shorter the take-up distance L the higher the stress limited maximum possible take-up velocity and the lower the resulting minimum fineness.

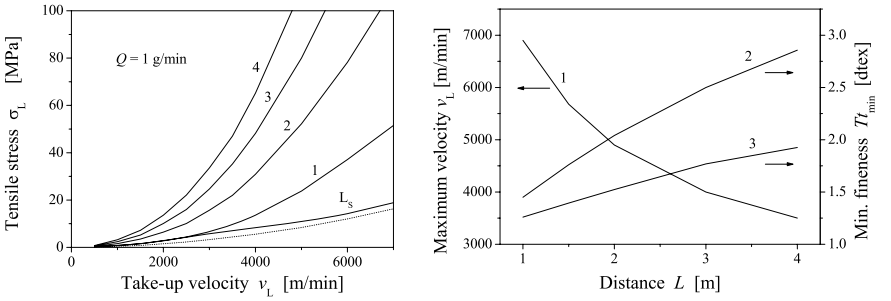

Fig. 3.67. *Left:* (calculated) filament stress σ_{L} vs. take-up velocity for different distances L, distances are indicated: $L = 1$ m (1), 2 m (2), 3 m (3), 4 m (4), and solidification distance L_{s}, *dotted line*: calculation without air friction; *right:* maximum possible take-up velocity (1) for the condition $\sigma_{\mathrm{L}} \leq 50$ MPa and minimum fineness Tt_{min} before (2) and after drawing (3) to 25% final elongation; PA 6, mass throughput $Q = 1$ g/min

For the example above, with constant throughput of 1 g/min, it is not possible to reach a final fineness of 1 dtex by only increasing the spinning speed. For the production of fine filaments the reduction of throughput appears at the same time necessary. To get an impression of this second variant in the next diagram (Fig. 3.68) the resulting tensile stress at distance $L = 1$ m with respect to the accessible fineness is compared if (1) the throughput is kept constant and the take-up velocity increases (this is the example above) and if (2) the take-up velocity is kept constant and the throughput decreases, respectively. It can be clearly observed that reducing the throughput leads to

much lower stress at any certain distance and opens up the way to spinning fine and ultra fine fibres.

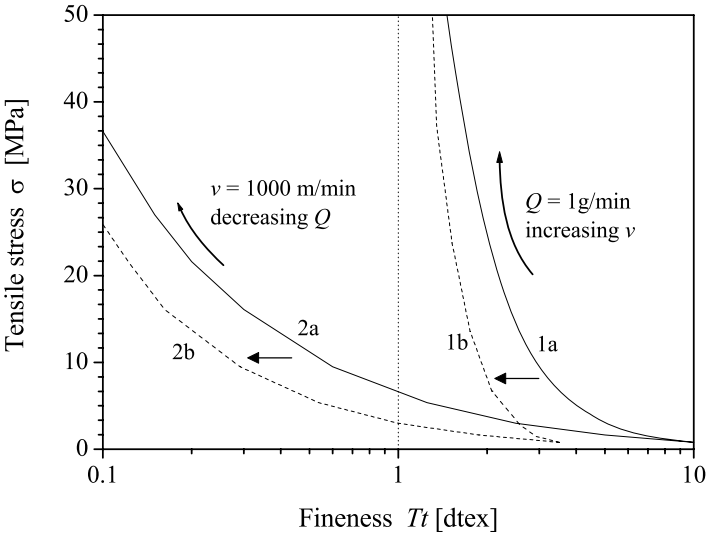

Fig. 3.68. (Calculated) filament tensile stress σ_{L} at distance $L = 1$ m vs. filament fineness Tt, (1) – constant throughput $Q = 1$ g/min, increasing take-up velocity, (2) – constant velocity $v = 1000$ m/min, decreasing throughput, (a) – fineness before drawing (as spun filaments, *solid lines*), (b) – fineness after drawing to 25% elongation (*dotted lines*)

Remark. Of course minimum air friction (and minimum stress level) results at solidification distance L_{s}. In practice, the take-up distance should be as long as necessary and as short as possible. To reduce air friction, it is effective to place the guide, where the single filaments are bundled together, as close to the spinneret as possible. Additionally, a further reduction of fibre stress seems possible via complete avoidance of air friction. The friction component disappears if air and fibres have an equal speed, realised by means of finely adjusted air stream *in the fibre direction* through using a special shaped (e. g. conical) spinning tube. In this case the tensile stress is mainly determined by inertia: $\sigma \approx \varrho \cdot v_{\mathrm{L}}^2$ (see dotted line in Fig. 3.67) and nearly independent of throughput and the current take-up distance. For very low mass throughput the cooling distance becomes very low and also the resulting stress contribution from inertia. Now, the surface tension and the contribution from initial rheological force F_0 at the spinneret becomes more and more important. F_0 is determined from the mean fluidity of the material in the deformation region and can be influenced within certain limits by means of a post heating zone below the spinneret in order to control the cooling and also the deformation behaviour. Finally, the limit for possible minimum fineness of continously spun and drawn filaments could be $Tt_{\min} \approx 0.1$ dtex .

On the other hand, the unlimited reduction of throughput leads sooner or later to capillary break, the filaments divide into single drops. Under limitation of very thin filaments the surface tension is contributed substantially at the spinneret exit. The following consideration supports this assumption. Melt spinning of filaments is also a generation of filament surface: The surface generation rate $\dot{A}_\mathrm{F}$ for a filament is given by

$$\dot{A}_\mathrm{F} = \pi \cdot D_\mathrm{F} \cdot v_\mathrm{F} = 2\sqrt{\pi \cdot v_\mathrm{F} \cdot \dot{Q}_\mathrm{V}}\,, \tag{3.195}$$

where D_F is the final filament diameter, v_F is the final velocity, and $\dot{Q}_\mathrm{V}$ is the volumetric rate of throughput. Assuming N single drops with radius R_d, the production rate of the drops surface $\dot{A}_\mathrm{d}$ is given by

$$N \cdot \dot{A}_\mathrm{d} = \frac{\dot{Q}_\mathrm{V} \cdot 4\,\pi\,R_\mathrm{d}^2}{4/3\,\pi\,R_\mathrm{d}^3} = \frac{3}{R_\mathrm{d}} \cdot \dot{Q}_\mathrm{V}\,, \tag{3.196}$$

and the ratio of surface generation between drops and filaments is given by the relationship

$$\frac{N\dot{A}_\mathrm{d}}{\dot{A}_\mathrm{F}} = \frac{3}{2\,R_\mathrm{d}}\sqrt{\frac{\dot{Q}_\mathrm{V}}{\pi\,v_\mathrm{F}}}\,. \tag{3.197}$$

At decreasing throughput (volume rate $\dot{Q}_\mathrm{V}$) the relation (3.197) becomes at a certain level < 1 and the division into single drops is the energetically favorable case. Of course the relationships above only provide for a qualitative discussion and are not applicable to any quantitative calculation. For the more detailed analysis Ziabicki showed that for capillary break the ratio between surface tension and viscosity of the melt plays an important role [274].

3.3.2 Visco-elastic Failure and Nonlinear Effects

Increasing spinning speed and/or decreasing throughput leads to filament breakage. Failure behaviour in spinning polymer melts includes:

- capillary break,
- cohesive, brittle fracture,
- ductile failure.

For low take-up velocities and low deformation rates the Newtonian viscous constitutive equation may sufficiently describe the rheological flow and deformation behaviour of the molten polymer. But even at higher deformation rates the visco-elastic polymers show transient effects which characterise the time dependency between polymer relaxation and deformation, described by any relaxation time spectrum. To discuss the effect of visco-elastic failure the simple Maxwell model (3.47) should be used. It is clear that the Maxwell

model, and only one single relaxation time λ, cannot completely characterise the rheological behaviour of the fiber forming polymers in melt spinning but the effect can be made quantitatively visible.

Equation (3.47) on page 63 can be written as

$$\eta \cdot \frac{\mathrm{d}v}{\mathrm{d}x} = \sigma + \lambda\, v\, \frac{\mathrm{d}\sigma}{\mathrm{d}x}, \qquad \lambda = \frac{\eta}{E}\,, \tag{3.198}$$

and together with $\sigma = F/A = \varrho_\mathrm{p}\, v\, F/Q$ then follows

$$\frac{\mathrm{d}v}{\mathrm{d}x} = \frac{1}{\eta} \cdot \frac{\sigma\left(1 + \lambda\, v \dfrac{1}{F}\, \dfrac{\mathrm{d}F}{\mathrm{d}x}\right)}{1 - \sigma/E}\,. \tag{3.199}$$

It can be seen from Eq. 3.199 that the deformation rate $\mathrm{d}v/\mathrm{d}x$ becomes infinitely large if the spinning stress σ or/and the compliance $1/E$ reach some critical value. Assuming constant tensile force $F(x) = F_\mathrm{c} = C \cdot Q/\varrho_\mathrm{p}$ as in the example on page 61 the deformation rate is simplified to

$$\frac{\mathrm{d}v}{\mathrm{d}x} = \frac{1}{\eta} \cdot \frac{\sigma}{1 - \sigma/E} = \frac{1}{\eta} \cdot \frac{C \cdot v}{1 - C \cdot v/E}\,. \tag{3.200}$$

The ratio between stress and deformation rate defines the *apparent elongational viscosity*

$$\eta_\mathrm{app} = \frac{\sigma}{\mathrm{d}v/\mathrm{d}x}\,, \tag{3.201}$$

which for the simplified case of constant force becomes

$$\eta_\mathrm{app} = \frac{\eta}{1 + \lambda \dfrac{\mathrm{d}v}{\mathrm{d}x}} = \frac{\eta}{1 + De}\,, \tag{3.202}$$

where De denotes the *Deborah*-number, which describes the ratio between relaxation time $\lambda = \eta/E$ and deformation time $(\mathrm{d}v/\mathrm{d}x)^{-1}$. Visco-elasticity appears as an artificial reduction of viscosity if the deformation is described in the manner above.

Ziabicki [184] discussed the solution of Eq. 3.200 for the special case of $E = \text{const.}$ and pointed out that after reaching the critical region some visco-elastic spinning instability occurs. Its intensity increases the more the ratio between the elastic and viscous properties of the material increases. Similar results were found by means of dynamic rheological measurements. For well spinnable polymers the ratio between storage modulus G' and loss modulus G'' must not exceed any critical value [269]. To illustrate the complexity of visco-elastic behaviour Fig. 3.69 (*left side*) shows the spinline velocity v vs. distance x from spinneret for three different ranges of elastic modulus: 1) the pure viscous case ($E \to \infty$), 2) the visco-elastic case describing the

spinning behaviour of PA 6 more realistically by means of a deformation dependent modulus $E = E_0\, f(\varepsilon_e)$ (Eq. 3.83), and 3) a visco-elastic case like 2) but with drastically reduced modulus (factor 0.01). The condition used for the calculation in all three cases was that both viscosity and modulus reach infinity at solidification distance and deformation finishes afterwards. The corresponding apparent viscosities Eq. 3.201 are shown at the right-hand side of Fig. 3.69. The DEBORAH number for the visco-elastic case 2)

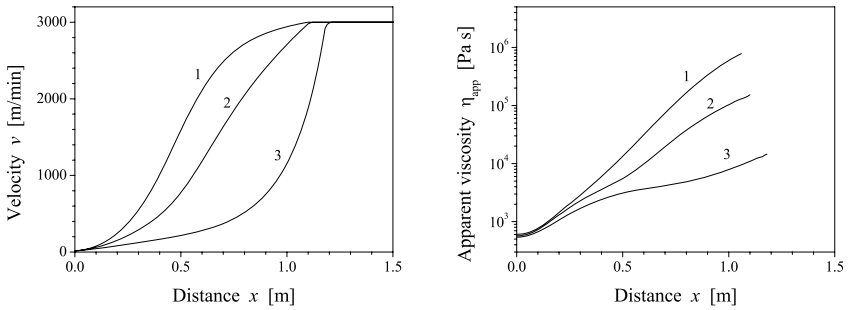

Fig. 3.69. The influence of visco-elasticity on spinning behaviour (calc.). *Left:* velocity v vs. distance x from spinneret exit, *right:* apparent elongational viscosity vs. distance, 1 – pure viscous behaviour ($E_1 \to \infty$), 2 – visco-elastic behaviour ($E_2 = E_0\, f(\varepsilon_e)$) realistically describing melt spinning of PA 6, 3 – highly elastic behaviour ($E_3 = 0.01 E_2$); material PA 6, mass throughput $Q = 1$ g/min, take-up velocity $v_L = 3000$ m/min

in Fig. 3.69 varies from $De \approx 0.05$ near the spinneret to $De \approx 5$ near the solidification point. This means that the spinning behaviour changes from viscous at the beginning over visco-elastic to mostly elastic deformation at the end.

A high deformation rate may lead to another effect well known in rheology: the decrease of viscosity with increasing the deformation rate. This kind of nonlinear rheological behaviour is often described in shear melt rheology by a power-law equation or by the CROSS-CARREAU model which can be generalised for extensional deformation to any equation of the form

$$\eta(T, \dot{\varepsilon}) = \frac{\eta_0(T)}{1 + a\, \dot{\varepsilon}^{\,b}} \,, \tag{3.203}$$

or, respectively

$$\eta(T, \dot{\varepsilon}) = \frac{\eta_0(T)}{1 + a\, \left(\eta_0(T) \cdot \dot{\varepsilon}\right)^b} \,, \tag{3.204}$$

with parameters a, b.

The nonlinear effect of decreasing viscosity is demonstrated in Fig. 3.70 where the fibre formation was calculated again for the visco-elastic MAXWELL model (Eq. 3.47) but now with deformation rate depending upon viscosity Eq. 3.203. Because it is only a qualitative comparison the simplified relation with power exponent $b = 1$ was used. Other used parameters are the same as in the example for the purely viscous (case 1) and the visco-elastic (case 2) behaviours.

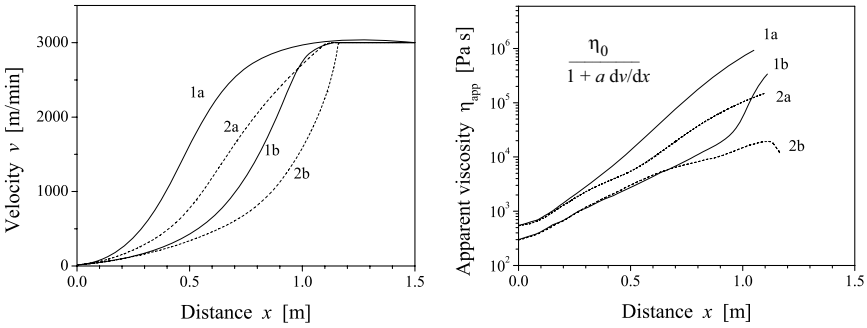

Fig. 3.70. The influence of nonlinear viscous and visco-elastic spinning behaviour (calc.), *left:* velocity v vs. distance x from spinneret exit, *right:* apparent elongational viscosity vs. distance, 1 – purely viscous behaviour ($E \to \infty$), 2 – visco-elastic behaviour ($E = E_0\, f(\varepsilon_e)$) realistically describing spinning of PA 6, (a) linear viscous behaviour, parameter $a = 0$, (b) nonlinear viscous behaviour, parameter $a = 0.1$; material PA 6, mass throughput $Q = 1$ g/min, take-up velocity $v_L = 3000$ m/min

Nonlinearity and visco-elasticity amplify each other because both show similar behaviour of decreasing the apparent viscosity while increasing the deformation rate. In Fig. 3.70 the beginning of failure at the end of graph (2b) can be seen, only prevented here by the abrupt end of the deformation because the viscosity and modulus are set to infinity at the solidification point. There is no solution for the calculation (within the frame of the used model equations) for any larger value of the nonlinearity parameter $a > 0.1$. The nonlinear and highly elastic behaviour can lead to fibre breakage if no rapid stabilisation effect follows. In melt spinning the stress induced crystallisation may overtake this role and acts as an additional hardener. Often the *neck*-like deformation observed is followed by stress induced crystallisation.

The different kinds of failure behaviour are shown in Fig. 3.71 (according to [270, 273]). Brittle fracture occurs if the stress exceeds the critical amount of the breaking stress. No special deformation appears at the point of rupture. Otherwise the ductile failure shows a typical thinning behaviour which may also lead to break, perhaps in a similar manner to the brittle fracture because the stress significantly increases. The thinning behaviour may be locally limited; this deformation is called *neck*-deformation. If the

elongation or the elongation rate exceeds some critical value, the transition to 'catastrophic' failure may occur and can be explained with the special nonlinear visco-elastic rheological material behaviour. On the other hand, if there is any stabilizing effect like stress/elongation induced crystallisation the required breaking stress may rapidly increase and thus fibre breakage may be avoided.

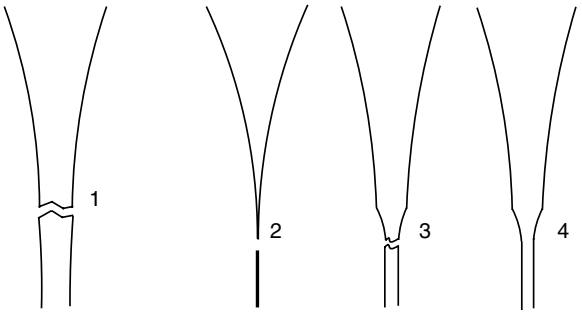

Fig. 3.71. Failure behaviour, 1 – brittle fracture, 2 – ductile failure, 3 – neck-like deformation, 4 – neck-like deformation followed by any stabilizing effect

Figure 3.72 shows some experimental results together with results from calculation, exemplary for high speed spinning of PA 6. The range from 3000 m/min to 7200 m/min and from 1.0 g/min to 3.0 g/min was investigated experimentally (the bold marked region in the diagram). Each point within the 'spinnability map' (according to [271–273]) represents a combination of take-up velocity v_L and draw down ratio $ddr = v_\mathrm{L}/v_0 \propto v_\mathrm{L}/Q$. Horizontal lines in this map represent constant draw down ratios and therefore constant finenesses. The straight lines passing the origin mark the states of constant mass throughput. For the experiments the take-up velocity was increased stepwise at constant mass throughput until fibre breakage occurred and no stable spinning process was further possible. The points (or more exactly: the small region) where the stable spinning behaviour turned into unstable behaviour mark the right border of the investigated region.

Additionally, the calculated lines of constant maximum deformation rate $\dot{\varepsilon} = \mathrm{d}v/\mathrm{d}x$ and the lines of constant stress σ_s at the solidification point are shown in the diagram.

The maximum possible draw down ratio decreases with increasing throughput and increasing take-up velocity. This means that in order to get fine filaments lower throughput and lower take-up speed is to be recommended with respect to spinning stability. It seems that for small throughputs the maximum deformation rate and the ductile failure behaviour are the limiting factors of spinnability. For sufficiently high mass throughputs and higher spinning speeds the melt spinning behaviour of PA 6 shows the typical neck-effect. Much higher deformation rates and also higher stresses are now possi-

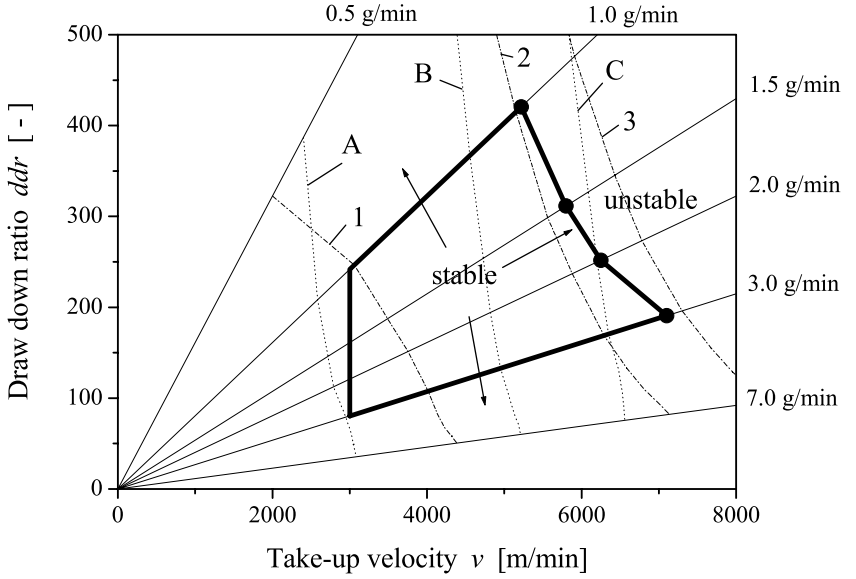

Fig. 3.72. Spinnability map for PA 6 melt spinning, lines of constant mass throughput (indicated); bold marked region: experimentally investigated, stable spinning conditions; points (•): limitation of spinnability, right from the border line no further spinning is possible; lines of constant maximum deformation rate (calculated): 1 – $\dot{\varepsilon} = 100\,s^{-1}$, 2 – $800\,s^{-1}$, 3 – $1200\,s^{-1}$, lines of constant stress at solidification point (calculated): A – $\sigma_s = 5$ MPa, B – 10 MPa, C – 15 MPa, data source: Institute of Polymer Research Dresden

ble. It seems that the stress induced crystallisation that occurs after necking acts as a stabiliser and the failure then results from brittle fracture. Similar conclusions were drawn also by other authors [273]. The failure behaviour of melt spun polymers is an interesting field of fibre research with many unsolved problems. The question of spinnability includes problems of material behaviour (flow behaviour, rheology, crystallisation, phase transition, structure development, and so on) as well as measuring and analytical techniques and also engineering practice.